HYDROGEN-ENRICHED METHANE-AIR COMBUSTION AT INTENSE TURBULENCE

by

Sajjad Mohammadnejad Daryani

A thesis submitted in partial fulfillment of
the requirements for the degree of

DOCTOR OF PHILOSOPHY

in

The College of Graduate Studies

(Mechanical Engineering)

THE UNIVERSITY OF BRITISH COLUMBIA

(Okanagan)

March 2022

The following individuals certify that they have read, and recommend to the College of Graduate Studies for acceptance, a dissertation entitled:

HYDROGEN-ENRICHED METHANE-AIR COMBUSTION AT INTENSE TURBULENCE

submitted by Sajjad Mohammadnejad Daryani in partial fulfillment of the requirements of the degree of Doctor of Philosophy

Dr. Sina Kheirkhah, School of Engineering

Supervisor

Dr. Sunny Li, School of Engineering

Supervisory Committee Member

Dr. Kendal Bushe, Department of Mechanical Engineering

Supervisory Committee Member

Dr. Liwei Wang, School of Engineering

University Examiner

Dr. Simone Hochgreb, University of Cambridge

External Examiner

Abstract

Internal structure and burning velocity of hydrogen-enriched methane-air turbulent premixed flames are investigated experimentally using planar laser-induced fluorescence of formaldehyde molecule and hydroxyl radical as well as stereoscopic particle image velocimetry techniques. A Bunsen burner is utilized to complete experiments at intense turbulence intensities (Karlovitz numbers up to 76.0). It is shown that, by increasing the turbulence intensity, the preheat and reaction zone thicknesses can increase to values that are, respectively, 6.3 and 4.9 of the corresponding laminar flames. Turbulent flow characteristics of the flames suggest that the potential penetration of eddies into the preheat and reaction zones is the underlying reason for the broadening of these zones. Broadening of the reaction zone, which is studied in this thesis, suggests that the flamelet assumption used in formulating the local consumption speed in past studies may not hold. Thus, a new formulation, which does not utilize the flamelet assumption, is developed and used for estimating the burning velocity of premixed flames. It is shown that, at small turbulence intensities, the values of the estimated burning velocity follow those of the local consumption speed. However, at large turbulence intensities and consistent with the results in the literature, the local consumption speed underpredicts the values of the burning velocity. It is shown that the amount of this underprediction is correlated with the broadening of the reaction zone, suggesting that the non-flamelet behavior contributes to this underprediction. It is shown, although the flame thickening increases the burning velocity, extinctions decrease this parameter, which may cause a characterized behavior, referred to as bending. The amount of this bending is

shown to be related to the inverse of the Damköhler number. Using this, a mathematical formulation that allows for the estimation of the burning velocity is developed. It is shown all of the above are influenced by the air entrainment, referred to as lack of back support. Specifically, this influences the flames structure and the burning velocity by diluting the reactants, changing the effective fuel-air equivalence ratio, and altering both the effective turbulence intensity and the effective normalized integral length scale.

Lay Summary

The flame structure and the rate at which reactants convert to products (burning velocity) are investigated experimentally for conditions with turbulent flow characteristics relevant to those of engineering applications. It is traditionally believed that the premixed flames feature a thin structure even at extremely turbulent conditions. Past studies have used this assumption to develop formulations for estimating the burning velocity. They have shown that as the turbulence is intensified, the burning velocity increases. However, this increase becomes less pronounced at large turbulence conditions, which is referred to as the bending behavior. This dissertation shows that the thin flame structure assumption does not always hold and proposes a new model for estimating the burning velocity. This thesis provides plausible answers to a few of ongoing questions in the area of turbulent combustion science. The proposed physics-based and experimentally obtained models can be used for improved design of future gas turbine engines.

Preface

All work presented in this dissertation was conducted under the supervision of Professor Sina Kheirkhah from the School of Engineering of the University of British Columbia. The experiments were performed at the Gas Turbine Laboratory of the Aerospace Research Centre at the National Research Council Canada. The results in this thesis have led to journal articles and conference presentations, which are listed in the following.

Journal publications

1. Mohammadnejad, S., An, Q., Vena, P., Yun, S., and Kheirkhah, S., (2021) "Contributions of flame thickening and extinctions to a heat release rate marker of intensely turbulent premixed hydrogen-enriched methane-air flames", Combustion and Flame, 231, 111481 [1].

2. Mohammadnejad, S., An, Q., Vena, P., Yun, S., and Kheirkhah, S., (2020) "Thick reaction zones in non-flamelet turbulent premixed combustion", Combustion and Flame, 222, 285-304 [2].

3. Mohammadnejad, S., Vena, P., Yun, S., and Kheirkhah, S., (2019) "Internal structure of hydrogen-enriched methane–air turbulent premixed flames: Flamelet and non-flamelet behavior", Combustion and Flame, Vol. 208, pp. 139-157 [3].

4. Mohammadnejad, S., An, Q., Vena, P., Yun, S., and Kheirkhah, S., (2022) "Lack of back-support effects on flame extinction, flame structure, and burning velocity",

submitted.

Conference publications and presentations

1. Mohammadnejad, S., An, Q., Vena, P., Yun, S., and Kheirkhah, S., (2020) "Broadening of reaction zones in turbulent lean methane-air premixed flames", Bulletin of the American Physical Society [4].

2. Mohammadnejad, S., Vena, P., Yun, S., and Kheirkhah, S., (2019) "Non-flamelet behavior of hydrogen-enriched methane-air turbulent premixed flames", Canadian Section of the Combustion Institute: 2019 Spring Technical Meeting.

3. Mohammadnejad, S., Vena, P., Yun, S., and Kheirkhah, S., (2019) "Towards quantifying the propensities of stable hydrogen-enriched methane-air turbulent premixed flames to blow-out and flash-back", Canadian Section of the Combustion Institute: 2019 Spring Technical Meeting.

Table of Contents

List of Tables

List of Figures

Acknowledgments

I would like to take the chance and express my sincerest gratitude to my supervisor Professor Sina Kheirkhah. His support, guidance, and effort played a pivotal role in the completion of this work. I am deeply thankful for his great help in preparing the thesis, journal articles, and conference presentations. He is one of the smartest people I have ever met and has always surprised me with his great research ideas. He was always passionate about presenting different materials and knew how exactly I can improve the quality of my presentations. For example, it was not possible to show a figure to him and do not get several suggestions for its improvement. He has good psychological abilities as well and knows how to get the best out of his students. He not only helped me with the scientific aspects but also provided me with financial support from different sources so that I have my full attention to the research. I never forget that once he said: "Money is the last thing I want you to be worried about". I am also thankful to him for giving me the permission to serve as a teaching assistant in several courses and providing me with the chance to help organize the Canadian Section of the Combustion Institute in the spring of 2019. He had great patience when things were going wrong. This reduced the amount of pressure on me, which was a great help in having my full concentration on the research. I learned so many things from him and had extremely enjoyable moments performing my research under his supervision.

I also want to thank Dr. Sean Yun, Dr. Patrizio Vena, and Dr. Qiang An from the Aerospace Research Centre of the National Research Council (NRC) Canada. They

facilitated performing sophisticated experiments at NRC to study the hydrogen-enriched methane-air premixed flames. I want to deeply thank Dr. Patrizio Vena for his great help especially in the first measurement campaign we performed in the summer of 2018 when I was new to Canada. He is super nice and a wonderful person. I will never forget that he picked me up from the airport, took me to a restaurant for a dinner, drove me to my accommodation, and when he saw that I have rented a room in an improper location of Ottawa (because of not being familiar with the city), he called my supervisor and said: "He cannot stay here". Then he searched himself and found another accommodation in an exceptionally peaceful location with a very nice landlord. I am also grateful to Dr. Wajid Ali Chishty and the Staff at NRC's gas turbine laboratory, especially Michel and Jonathan that helped me in collecting data. I am especially thankful to them for coming earlier than regular working hours and leaving very late at night so that I can finish collecting all of my data.

I would like to thank Dr. Gilles Bourque and Dr. Philippe Versailles for their great help and support as well as the chance they provided me with to conduct experiments on the newly designed nozzles of Siemens Energy Canada Limited. I would also like to acknowledge the financial support from the MITACS Accelerate program, Siemens Energy Canada Limited, and Fortis BC.

Finally, I would like to thank my family, lab mates, friends, and relatives that helped and supported me during my Ph.D. Especially, the unconditional love and support of my father, Mahmoud Mohammadnejad Daryani, and my mother, Roghayyeh Dehghan Dizaji, helped me to stand up and face all of the challenges and hardships during these years. I am grateful to Leslie Saca and Ramin Heydarlaki for their collaborations with me in the lab and my other lab mates, Zahra Mollahoseini, Deepanshi Sisodiya, Sepehr Mosadegh, Ali Rostami, Jesse Morales, and Zejia Xu. I am also thankful to my brother, Hossein Mohammadnejad Daryani, and my friends in UBC, Amin Naeini, Sadaf Shabanian, Hassan Navazi, Kam-

ran Alasvand, Shiva Khoei, Hamed Mirzaei, Majed Amini, Faezeh Ketabchi, Parisa Alaei, Hossein Boojari, Bahare Rahimi, Zhila Bahrami, Iman Jalilvand, Elnaz Ghahremani Rad, Kianoush Alasvand, Aydin Badrian, Reza Suraki, and so many other friends that helped me have enjoyable moments in here.

Dedication

For my parents,

who dedicated their purest love and support to me.

Nomenclature

Symbols

A	Area
$\mathcal{A}$	Area of eddy
$\overline{A}_{\mathrm{f}}$	Flame surface area
A_{Le}	A variable for calculation of effective Lewis number
A_{OH}	Area of region in the FOV with large OH PLIF signal
A_{R}	A constant in the study of Ronney and Yakhot (CST, 1992)
A_{W}	Area of window "W"
B_{L}	Laminar flame burning rate
$B_{\mathrm{L},0}$	Freely propagating laminar flame burning rate
$B_{\mathrm{L},0,\mathrm{eff}}$	Effective freely propagating laminar flame burning rate
B_{T}	Turbulent flame burning rate
$B_{\mathrm{T},\xi}$	Local turbulent flame burning rate
$\mathcal{C}$	Circumference of eddy
C_1	ICCD camera for collecting OH PLIF signal
C_2	ICCD camera for collecting CH_2O PLIF signal
C_3	PIV sCMOS camera
C_4	PIV sCMOS camera
CH	Methylidyne radical radical
$\mathrm{C}_2\mathrm{H}$	Ethynyl radical

CH_4	Methane
CH_2O	Formaldehyde molecule
$[CH_2O]$	Formaldehyde molecule concentration
CH_2O_{max}	Maximum CH_2O PLIF signal
CH_2O_{PLIF}	Formaldehyde molecule PLIF signal
CO	Carbon monoxide
c_1	A constant in the study of Wabel et al. (PCI, 2017)
c_2	A constant in the study of Wabel et al. (PCI, 2017)
c_3	A constant in the study of Wabel et al. (PCI, 2017)
$\overline{c}_{OH}$	Mean progress variable obtained by binazring the OH images
c_p	Specific heat
$c_{p,0}$	Specific heat of reactants at 1500 K
$c_{p,k}$	Specific heat of the the k^{th} component
D	Bending behavior
Da	Damköhlder number
Da_{eff}	Effective Damköhlder number
E	Error function for the calculation of α and β
E'	Error function for the calculation of α' and β'
E_a	Activation energy
$FWHM_F$	Full width at half maximum of reaction zone thickness
$FWHM_P$	Full width at half maximum of preheat zone thickness
f_B	Boltzmann population function
H	Hydrogen atom
H_2	Hydrogen
$H_2\%$	Hydrogen-enrichment percentage
HCO	Formyl radical

[HCO]	Formyl radical concentration
H_2O	Water
HRR	Heat release rate
$\overline{HRR}$	Mean heat release rate
$\overline{HRR}_{\mathrm{L}}$	Mean heat release rate of laminar flame
HRR_{n}	Heat release rate normalized by the corresponding maximum
$\overline{HRR}_{\mathrm{T}}$	Mean heat release rate of turbulent flame
h	Vertical distance along y-axis for calculation of Λ
h^*	Smallest vertical distance along y-axis that R_{uu} becomes zero
I	Incident laser intensity
I_0	Flame stretch factor
I_{HRR}	Heat release rate marker
$\overline{I}_{\mathrm{HRR}}$	Mean I_{HRR}
i	Summation variable
J	Discrepancy between normalized heat release rate marker and normalized local consumption speed
Ka	Karlovitz number
KE	Specific total kinetic energy of eddy
KE_ω	Specific rotational kinetic energy of eddy
k	Summation variable
k_{f}	Forward reaction rate constant
$\mathcal{L}$	Markstein length
L_1	-25 mm cylindrical lens
L_2	400 mm cylindrical lens
L_3	1000 mm cylindrical lens

$L_{P_1P_2}$	Length of a portion of the line "L", which is inside the interrogation window
L_ξ	Length of the mean progress variable contour
Le_{eff}	Effective Lewis number
$Le_{\text{eff,st}}$	Effective Lewis number for stoichiometric mixture
Le_i	Lewis number of i^{th} component
Le_{O_2}	Lewis number of Oxygen
l'	Side length of a square-shaped eddy
l_T	Taylor length scale
${l_T}^*$	Taylor length scale at 1500 K
M_1	532 nm mirror
M_2	355 nm mirror
M_3	283 nm lens
$\mathcal{M}_L$	Laminar heat release rate marker
$\mathcal{M}_{L,\text{eff}}$	Effective heat release rate marker for laminar flame
$\mathcal{M}_T$	Turbulent heat release rate marker
$\dot{m}_r$	Reactants mass flow rate
N	Total number of the species in a fuel-air mixture used for calculating its specific heat and thermal conductivity
$\mathcal{N}\%$	Non-flamelet behavior percentage
N_{FL}	Number of data points featuring flamelet behavior in OH versus CH_2O diagram
N_{NF}	Number of data points featuring non-flamelet behavior in OH versus CH_2O diagram
N_{OH}	Number of pixels featuring large OH PLIF signal
$N_{\overline{OH}}$	Number of pixels expected to feature large time-averaged OH PLIF signal

N_t	Total number of data points in the Cantera simulations for calculation of α and β
n	Number of the POD modes removed from the velocity data
n_e	Number of eddies
n_i	Number density of excited species
$\mathbf{n}_\mathrm{LE}$	Unit vector normal to flame leading edge
n_R	A constant in the study of Ronney and Yakhot (CST, 1992)
O	Oxygen atom
O_2	Oxygen
OH	Hydroxyl radical
OH^*	Electrically excited OH
[OH]	Hydroxyl radical concentration
OH_max	Maximum OH PLIF signal
OH_PLIF	Hydroxyl radical PLIF signal
P	Pressure
P_0	Atmospheric pressure
p	Perimeter
Q	swirling strength
Q_{21}	Quenching rate
$\dot{Q}_\mathrm{Co-flow}$	Flow rate of co-flow
Q_P	Swirling strength in preheat zone
Q_R	Swirling strength in reactants
$Q_\mathrm{R,L}$	Swirling strength in reactants for laminar flame
q	Threshold for calculation of non-flamelet behavior
R	Universal gas constant
$\mathcal{R}$	Equivalent radius of eddy

R_{uu}	Auto-correlation of the streamwise velocity
Re_{l_T}	Turbulent Reynolds number
Re_R	Secondary Reynolds number in the study of Ronney and Yakhot (CST, 1992)
Re_λ	Reynolds number estimated based on Taylor length scale
r	Radius of circle
r_c	Local radius of flame front curvature
S	Fluorescence signal intensity
S_L	Laminar flame speed
$S_\mathrm{L,0}$	Freely propagating laminar flame speed
$S_\mathrm{L,0,eff}$	Effective freely propagating laminar flame speed
$S_\mathrm{T,GC}$	Global consumption speed
$S_\mathrm{T,LC}$	Local consumption speed
$S_\mathrm{T,LD}$	Displacement speed
Sc	Schmidt number
s_1	Power of [OH] for estimation of I_HRR in study of Chi et al. (PCI, 2018)
s_2	Power of [CH_2O] for estimation of I_HRR in study of Chi et al. (PCI, 2018)
T	Temperature
T_b	Products temperature
T_n	Temperature normalized by the corresponding maximum
T_u	Reactants temperature
t	Time
U	Mean bulk flow velocity
u'	Root-mean-square of velocity fluctuations in upstream direction
$\mathbf{V}_\mathrm{FLAME}$	Flame velocity vector
$\mathbf{V}_\mathrm{GAS}$	Gas velocity vector

v'	Root-mean-square of velocity fluctuations in y direction
w'	Root-mean-square of velocity fluctuations in z direction
X_{CH_2O}	CH_2O mole fraction
$X_{CH_2O,n}$	CH_2O mole fraction normalized by the corresponding maximum
X_k	Mole fraction of k^{th} component
X_{OH}	OH mole fraction
$X_{OH,n}$	OH mole fraction normalized by the corresponding maximum
X_R	A variable in the study of Ronney and Yakhot (CST, 1992)
x	Streamwise axis
x_i	Fuel volumetric fraction of i^{th} component
Y_k	Mass fraction of k^{th} component
y	Axis in the imaging field and normal to the streamwise direction
Z	Position across a freely propagating laminar flame
z	Axis normal to the imaging field

Greek symbols

α	Power of CH_2O for estimation of I_{HRR}
α'	Power of $[CH_2O]$ for estimation of I_{HRR}
α_0	Thermal diffusivity at 1500 K
α_{th}	Reactants thermal diffusivity
β	Power of OH for estimation of I_{HRR}
β'	Power of [OH] for estimation of I_{HRR}
β_{Le}	Zeldovich number
γ_i	i^{th} POD mode
δ_F	Reaction zone thickness
δ'_F	Most probable value of reaction zone thickness

$\delta_{\mathrm{F,L}}$	Reaction zone thickness of laminar flame
$\delta'_{\mathrm{F,L}}$	Most probable value of reaction zone thickness for laminar flame
$\delta_{\mathrm{F,L,0}}$	Reaction zone thickness of freely propagating laminar flame
δ_{L}	Laminar flame thickness
δ'_{L}	laminar flame thickness estimated at 300 K
$\delta_{\mathrm{L,eff}}$	Effective laminar flame thickness
δ_{laser}	Laser sheet thickness
δ_{P}	Preheat zone thickness
δ'_{P}	Most probable value of preheat zone thickness
$\delta_{\mathrm{P,L}}$	Preheat zone thickness of laminar flame
$\delta'_{\mathrm{P,L}}$	Most probable value of preheat zone thickness for laminar flame
$\delta_{\mathrm{P,L,0}}$	Preheat zone thickness of freely propagating laminar flame
ϵ	Turbulent dissipation
ϵ^*	Strain rate
ζ_i	rotational speed
η	Curvilinear axis normal to $\overline{c}_{\mathrm{OH}}$
η^*	Kolmogorov length scale at 1500 K
η_{K}	Kolmogorov length scale
η_{max}	maximum of η
η_{min}	Minimum of η
Λ	Integral length scale
Λ'	Transverse length scale
λ	thermal conductivity of reactants
λ_0	thermal conductivity of reactants at 1500 K
λ_k	Thermal conductivity of k^{th} component
ν	Reactants kinematic viscosity

ν^*	Reactants kinematic viscosity at 1500 K
ξ	Curvilinear axis tangent to $\overline{c}_{\mathrm{OH}}$
ξ_{max}	maximum of ξ
ξ_{min}	Minimum of ξ
ρ_{r}	Reactants density
Σ	Flame surface density
σ_{blur}	Blurring parameter
τ_{f}	Flame time scale
$\tau_{\eta_{\mathrm{K}}}$	Kolmogorov time scale
ϕ	Fuel-air equivalence ratio
ϕ_{eff}	Effective fuel-air equivalence ratio
ω	Vorticity

Abbreviations

CF	Co-flow
DNS	Direct numerical simulation
FCR	Flow characterization region
FOV	Field of view
FWHM	Full width at half maximum
HG	Harmonic generator
ICCD	Intensified charge couple device
JPDF	Joint probability density functions
LE	Leading edge
LES	Large eddy simulation
LFL	Lower flamability limit
Nd:YAG	Neodymium, Yttrium, Aluminum, and Garnet

P	Photodiode
PDF	Probability density function
PIV	Particle image velocimetry
PLIF	Planar Laser-Induced Fluorescence
POD	Proper Orthogonal Decomposition
RHS	Right-hand-side
RMS	Root-mean-square
SLPM	Standard litre per minute
SPIV	Stereoscopic particle image velocimetry
sCMOS	scientific Complementary metal–oxide–semiconductor
TG	Turbulence generator
UV	Ultra violet

Chapter 1

Introduction

This chapter is divided into 4 sections. In the first section, the motivation of this thesis is discussed. The relevant background is reviewed in the second section to discuss the existing knowledge gaps in the literature and provide the knowledge required for addressing the objectives of the dissertation. The objectives of this thesis are presented in the third section. Finally, the outline of the thesis is summarized in the last section of this chapter.

1.1 Motivation

Hydrogen-enrichment of natural gas (which mainly contains methane) will be used as a means to decarbonize several industries that use combustion equipment, such as land-based power generation gas turbine engines in the near future [24]. Several investigations suggest that hydrogen-enrichment of natural gas reduces the emission of carbon oxides [25–30], partly addresses the sustainability issue of natural gas (since hydrogen can be produced by water electrolysis using sustainable sources such as wind and solar energies [31, 32]), and decreases the possibility of flame blow-out [25, 27]. In spite of the aforementioned advantages of mixing hydrogen with methane, our understanding related to the internal structure (preheat and reaction zones) and also the speed at which the fuel and air mixture is converted to combustion products (referred to as the turbulent burning velocity) is limited for both pure and hydrogen-enriched methane-air flames, especially at engine flow-relevant conditions (extremely turbulent conditions with, for example, root-mean-square of the reactants streamwise velocity divided by mean the bulk flow velocity, u'/U, of about 50% [33]).

Understanding the internal structure of extremely turbulent flames is of significant importance since the developed knowledge can be potentially utilized for the generation of models that can be reliably used for the design and development of the relevant combustion equipment. Despite the large number of investigations performed to study the moderately turbulent premixed flames ($u' \lesssim 2$ m/s), see for example the review papers by [6, 34, 35], experimental data as well as knowledge related to the internal structure of turbulent premixed flames that are more relevant to gas turbine engines are mainly limited to few research groups, see for example the studies of [8, 36, 37]. Results presented in these studies point to contradictory conclusions and are only limited to methane-air flames. Also, due to the small number of conducted experiments, there exist several unanswered research questions related to both pure and hydrogen-enriched methane-air flames. For instance, the influences of lack of back-support, room air-entrainment of the reactants, and flame extinction on the internal structure of these flames are not well understood. Thus, further investigations are required to study the internal structure of highly turbulent pure and hydrogen-enriched methane-air premixed flames.

Related to the flame internal structure is the turbulent burning velocity. This is an important parameter since it facilitates quantifying how fast turbulent premixed flames burn, is linked to the thermal power a combustor can generate, and is also commonly used to compare and validate both direct numerical simulations (DNS) and large eddy simulation (LES) using the experimental investigations [34]. The burning velocity has been estimated using the flamelet assumption for methane-air flames, see for example the review papers by Driscoll [6, 34]. The flamelet assumption is considered to hold provided either of the following two criteria are satisfied. First, for test conditions that the turbulent premixed flame reaction zone thickness does not exceed the corresponding laminar flame counterpart significantly [6, 34, 38–41], the flamelet assumption holds. The second criterion suggests that for the test conditions that the relations between the combustion species

and temperature follow those of the corresponding laminar flame, the flamelet assumption holds [6, 42]. Although several studies show that the flamelet assumption holds for a wide range of turbulence conditions [8, 42], results of several other investigations [12, 36, 37, 43–49] disagree and suggest that the flamelet assumption may not hold. For these studies [12, 36, 37, 43–49], the turbulent burning velocity cannot be estimated using the formulations developed based on the flamelet assumption. Also, there exist several ongoing research questions pertaining to the turbulent burning velocity of the premixed flames, especially those with large turbulence intensities. For example, the reason for the existing inconsistency between the reported values of the turbulent burning velocities obtained using different formulations is not well understood. Effect of room air entrainment and reactants dilution (here, referred to as lack of back support) on the turbulent burning velocity is remained to be investigated as well.

The present thesis is motivated by three research questions. The first question pertains to the internal structure of pure and hydrogen-enriched methane-air flames at intensely turbulent conditions. What are the underlying reasons for the contradictory results in the literature regarding the premixed flames internal structure? The second question is related to the burning rate of the premixed flames. How the burning velocity of the premixed flames can be estimated for the conditions that the flamelet assumption does not hold and why there exists a disparity between the values of the burning velocity reported in the literature? Third, what are the effects of lack of back-support on the internal structure and burning velocity of the premixed flames?

1.2 Background

This section is divided into five subsections. In the first subsection, the structure of a laminar flame is presented and the preheat and reaction zone thicknesses are defined. The planar laser-induced fluorescence (PLIF) methods for tracking the spatial variation of the

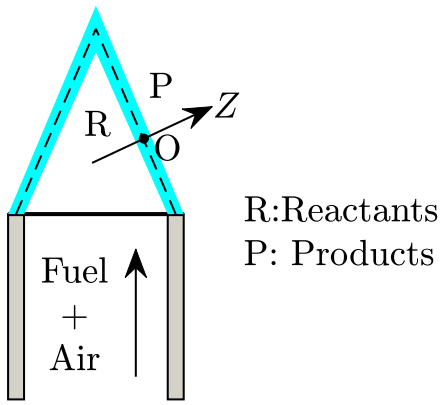

Fig. 1.1. Schematic of a premixed laminar Bunsen flame.

premixed flames heat release rate are discussed in the second subsection. The background related to turbulent premixed flames structure and burning velocity is reviewed in the third and fourth subsections, respectively. Finally, the background related to the effect of the hydrogen-enrichment on the internal structure and burning velocity of turbulent premixed flames is discussed in the last subsection.

1.2.1 Laminar flames structure

It is of significant importance to understand the characteristics of laminar flames for many reasons. Two that are relevant to this thesis are discussed here. First, for nearly laminar and moderately turbulent flames, the local structure of the flames is believed to be similar to that of a laminar flame [6, 34, 38]. Second, the laminar flames are used as a benchmark for comparing characteristics of the turbulent flames and as a result development of a regime diagram. Figure 1.1 shows a laminar Bunsen flame schematic. Moving from the reactants to the products along a line normal to the flame, a very short distance exists along which most of the chemical reactions occur. For a two-dimensional domain, this distance becomes a thin region, which is referred to as the flame and is highlighted by the blue color in Fig. 1.1. Figure 1.2 shows the flame structure in this region for two representative conditions with a fuel-air equivalence ratio of 0.7 and hydrogen-enrichment percentages (the

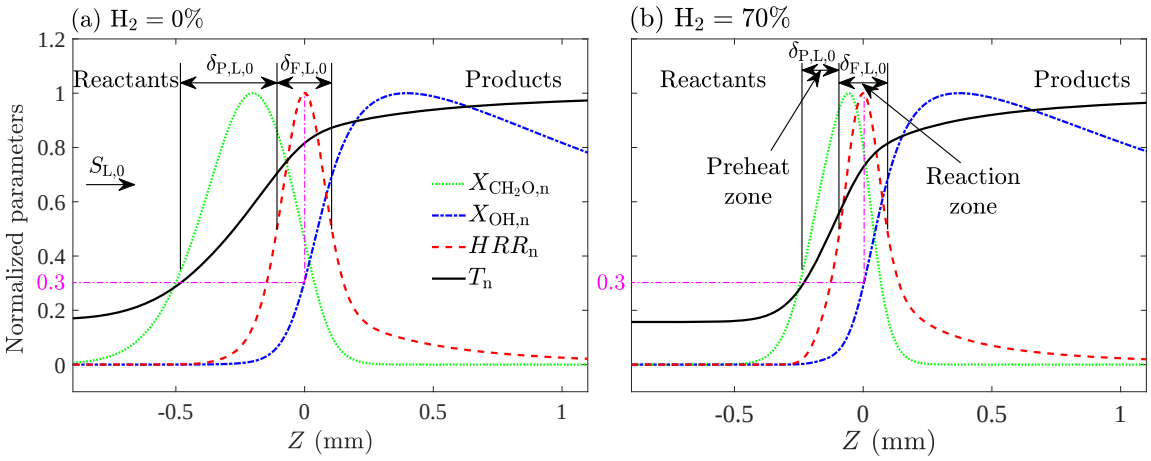

Fig. 1.2. (a) and (b) present the chemical structure of freely propagating laminar premixed flames of methane and air enriched by 0% and 70% of hydrogen, respectively. The fuel-air equivalence ratio is 0.7. $\delta_{P,L,0}$ and $\delta_{F,L,0}$ highlight the preheat and reaction zone thicknesses for the freely propagating flames and $S_{L,0}$ is the unstretched laminar flame speed. Also, $X_{CH_2O,n}$, $X_{OH,n}$, HRR_n, and T_n are the normalized (by corresponding maximum values) mole fraction of CH_2O, mole fraction of OH, heat release rate, and temperature respectively.

percentage of the ratio of the hydrogen volume flow rate to the summation of the hydrogen and methane volume flow rates) of $H_2 = 0$ and 70%. The results in the figure are generated using Cantera [50] simulations for atmospheric freely propagating flames with the GRI-Mech 3.0 mechanism. In this figure, $X_{CH_2O,n}$, $X_{OH,n}$, HRR_n, and T_n are the normalized (by the corresponding maximum values) mole fraction of CH_2O, mole fraction of OH, heat release rate, and temperature, respectively.

The flame itself is composed of several regions [5]. Two regions that are of significant importance are the preheat and reaction regions (also called zones). The reaction zone is where most of the heat release rate is generated [51, 52]. More specifically, the reaction zone is the loci of points at which the amount of heat release rate is larger than 50% of the maximum heat release rate [8, 53, 54]. The thickness of this region is highlighted by $\delta_{F,L,0}$ in Figs. 1.2(a) and (b). Compared to the reaction zone, the preheat zone is the locus of points at which the flame temperature increases, but there does not exist a large heat release rate. As can be seen in Fig. 1.2, there exists a considerable amount of CH_2O in the preheat zone. Specifically, the preheat zone is defined as where the mole fraction of CH_2O is more than

35% of the corresponding maximum value but the amount of the heat release rate is not significant (smaller than 50% of its maximum) [53, 55]. The thickness of the preheat zone is highlighted by $\delta_{\mathrm{P,L},0}$ in Fig. 1.2. Also, shown by an arrow in Fig. 1.2(a) is a vector that presents the fresh reactants relative flow velocity compared to the flame, whose magnitude is $S_{\mathrm{L},0}$ [51, 52]. The values of the laminar preheat and reaction zone thicknesses as well as the laminar flame speed are presented and used later in Chapters 4 and 5.

Compared to the preheat and reaction zone thicknesses, the (total) laminar flame thickness, δ_{L}, is defined as the sum of the preheat and reaction zone thicknesses [51, 52, 56]

$$\delta_{\mathrm{L}} = \delta_{\mathrm{P,L},0} + \delta_{\mathrm{F,L},0}. \tag{1.1}$$

Alternatively, δ_{L} can also be defined [5, 56–58] as a reactive-diffusive length associated with the relative diffusion of heat from the flame to the reactants and the flame speed, which is given by

$$\delta_{\mathrm{L}} \sim \frac{\alpha_0}{S_{\mathrm{L},0}}, \tag{1.2}$$

where α_0 is the flame thermal diffusivity calculated using

$$\alpha_0 = \frac{\lambda_0 / c_{\mathrm{p},0}}{\rho_{\mathrm{r}}}, \tag{1.3}$$

with λ_0 and $c_{\mathrm{p},0}$ being the gas thermal conductivity and the constant pressure specific heat (both estimated at reaction temperature of about 1500 K), and ρ_{r} is the fuel and air mixture (reactants) density (estimated at 300 K). Combining Eqs. (1.2) and (1.3), the laminar flame thickness can be estimated from [5, 6, 8, 58]

$$\delta_{\mathrm{L}} = \frac{\lambda_0 / c_{\mathrm{p},0}}{\rho_{\mathrm{r}} S_{\mathrm{L},0}}. \tag{1.4}$$

Please note that δ_{L} estimated from Eqs. (1.1) and (1.4) can yield different values. Values

obtained from Eq. (1.4) are used in the present dissertation, similar to [5, 6, 8, 58].

1.2.2 PLIF for prediction of the heat release rate

Of significant importance in studying lean premixed methane-air turbulent flames structure is the formyl radical concentration, [HCO], since it is directly linked to the heat release rate [59, 60]. Please note that "[ ]" indicates the species concentration. Planar Laser-Induced Fluorescence technique can be utilized to investigate the formyl radical concentration; however, measuring [HCO] is challenging due to two reasons. First, excitation of the formyl radical at experimentally-accessible wavelengths leads to spectral fluorescence interference with other species. Second, [HCO] is relatively small, which leads to small values of the signal-to-noise ratio. These two issues adversely influence the quality of the HCO PLIF measurements. To partly address the former issue, Zhou et al. [61] utilized a pulsed alexandrite laser. They [61] concluded that the excitation at 259.004 nm leads to minimum spectral fluorescence interference with other species for lean methane-air flames. However, for rich conditions, spectral emissions from large hydrocarbons formed in the flames pollute the HCO PLIF signal. An alternative approach for heat release rate-related measurements is PLIF of species that lead to the formation of the formyl radical. For example, Kiefer et al. [62] considered

$$\mathrm{CH_2O + OH \xrightarrow{k_f} HCO + H_2O} \tag{1.5}$$

as a reaction that leads to significant HCO formation in lean methane-air premixed flames. Specifically, from Eq. (1.5), the time-rate of change of [HCO] is given by [63]

$$\frac{\mathrm{d[HCO]}}{\mathrm{dt}} = k_\mathrm{f}(T)[\mathrm{CH_2O}][\mathrm{OH}] \tag{1.6}$$

where $[\mathrm{CH_2O}]$ and [OH] are the concentrations of the $\mathrm{CH_2O}$ molecule and OH radical, respectively, with $k_\mathrm{f}(T) = 5.7 \times 10^{-17} T^{1.18} \exp(225/T)$ being the forward reaction rate

constant [64]. Equation (1.6) suggests that the heat release rate, which is related to the time rate of change of [HCO], equals multiplication of [CH_2O], [OH], and $k_f(T)$. It is important to note that the measured PLIF signals of CH_2O and OH are not necessarily linearly related to the corresponding species concentrations. The fluorescence signal intensity (S), is given by [65]

$$S = I n_i \underbrace{\frac{f_B(T)}{Q_{21}(T)}}_{f(T)}, \tag{1.7}$$

where I is the incident laser intensity, n_i is the number density of the excited species and is proportional to the species of interest concentration, f_B is the Boltzmann population function, and Q_{21} is the quenching rate. For a constant incident laser intensity, it is straight forward to show that the fluorescence intensity is proportional to the multiplication of $f(T) = f_B(T)/Q_{21}(T)$ and the concentrations of the species of interest [66]. Thus, the multiplication of the CH_2O and OH PLIF signals can be estimated from

$$CH_2O_{PLIF}OH_{PLIF} = g(T)[CH_2O][OH], \tag{1.8}$$

where CH_2O_{PLIF} and OH_{PLIF} are PLIF signals of CH_2O and OH, respectively and $g(T) \propto f_{CH_2O}(T) f_{OH}(T)$. Several past investigations, e.g. [8, 36, 53, 54, 67], assumed that $g(T) \propto k_f(T)$. This assumption along with combination of Eqs. (1.6) and (1.8) can be used to show that

$$\frac{d[HCO]}{dt} \propto CH_2O_{PLIF}OH_{PLIF}. \tag{1.9}$$

However, validity of this assumption ($g(T) \propto k_f(T)$) remains to be investigated and is later discussed in Chapter 3. In order to accurately estimate the HRR of methane-air premixed flames, Wabel et al. [66] and Kyritsis et al. [68] suggested that the PLIF intensities of

hydroxyl radical (OH_{PLIF}) and formaldehyde (CH_2O_{PLIF}) can be obtained from

$$OH_{PLIF} \propto X_{OH}, \tag{1.10a}$$

$$CH_2O_{PLIF} \propto X_{CH_2O} \times \underbrace{[1 - \exp(-1680.5/T)] \times \left[\frac{40.1969 \exp(-740/T)}{(1 + 0.134/T + 0.37/T^2)T^{3/2}}\right] T^{3/4}}_{h(T)}, \tag{1.10b}$$

where X_{OH} and X_{CH_2O} are the mole fractions of OH and CH_2O (as introduced in the previous subsection), respectively. Please note that Eq. (1.10) is developed for methane-air flames and its validity for hydrogen-enriched methane-air flames remains to be investigated. Using this equation for hydrogen-enriched methane-air flames is one of the limitations of this study. As demonstrated in Eq. (1.10), the intensity of the OH PLIF signal is proportional to its mole fraction. However, for CH_2O, increasing the temperature from 300 K to 700 K and 2000 K, first increases $h(T) = CH_2O_{PLIF}/X_{CH_2O}$ from 0.05 to 0.09, and then decreases this parameter to 0.05. Utilizing Eq. (1.10), the OH_{PLIF} and CH_2O_{PLIF} signals as well as the temperature data, the mole fractions (and/or concentrations) of these species can be estimated. Then, these concentrations, the temperature data, and Eq. (1.6) can be used to estimate the heat release rate. Although, this strategy (compared to that obtained from Eq. (1.9)) allows for more accurate estimation of the heat release rate, simultaneous measurements of CH_2O_{PLIF}, OH_{PLIF}, and temperature is experimentally expensive.

As alternatives, there exist other PLIF/concentration/mole fraction methods to track the heat release rate of methane-air premixed flames as well. For example, the study of Najm et al. [59] suggests that the location of OH mole fraction (or PLIF signal) peak is relatively close to the location of the heat release rate peak for the regions with small curvature. However, for highly curved flame regions, this correlation weakens [60]. CH PLIF also is commonly used to track the heat release rate [8, 36, 44, 69, 70]. Multiplications of CO and OH as well as OH and CH_4 concentrations are also other methods to track the location

of heat release rate [60]. Chi et al. [7] used multiplication of CH_2O and H for assessing methane-air flames heat release rate. Marshall and Pitz [71] used a similar method to track the heat release rate of lean hydrogen-air flames. For example, they [71] used [H] as well as $[O_2] \times [H]$, $[OH] \times [H_2]$, and $[O] \times [H_2]$ to estimate the heat release rate of the lean hydrogen-air flames, where [H], $[O_2]$, $[H_2]$, and [O] are concentrations of H, O_2, H_2, and O respectively. They [71] concluded that [H] is an accurate indicator of the heat release rate in lean hydrogen-air flames.

1.2.3 Turbulent flames structure

In this section, the literature related to the preheat and reaction zones of premixed flames are reviewed. Similar to the laminar flame, the reaction zone of a turbulent flame is the region where a significant heat release rate (more than 50% of the maximum heat release [8, 53, 54]) is generated [51, 52]. The preheat zone of a turbulent premixed flame is visualized using CH_2O PLIF. Specifically, the preheat zone is defined as the region where CH_2O PLIF signal is more than 35% of the corresponding maximum value and the heat release rate is smaller than 50% of its maximum [53, 55]. The preheat and reaction zone thicknesses are denoted by δ_{P} and δ_{F} in this dissertation, respectively.

The internal structure of premixed flames can be highly influenced by the turbulent flow characteristics. The turbulent Reynolds number (Re_{T}) allows to quantify the turbulent flow characteristics and is given by

$$Re_{\mathrm{T}} = \frac{u'\Lambda}{\nu}. \tag{1.11}$$

In Eq. (1.11), Λ is the integral length scale and is estimated using the auto correlation of the velocity data (R_{uu}). These are given by [72]

$$\Lambda(x, y) = \int_0^{h^*} R_{uu}(x, y, h)\mathrm{d}h, \tag{1.12a}$$

$$R_{uu}(x,y,h) = \frac{\overline{\left[u(x,y) - \overline{u(x,y)}\right]\left[u(x,y+h) - \overline{u(x,y+h)}\right]}}{\overline{\left[u(x,y) - \overline{u(x,y)}\right]^2}}, \tag{1.12b}$$

where u is the streamwise velocity and h^* is the smallest vertical distance along the y-axis that R_{uu} attains a zero value. In Eq. (1.12b), the over-bar symbol represents averaging over time. In Eq. (1.11), ν is the fuel and air mixture (reactants) kinematic viscosity (estimated at 300 K). In addition to the integral length scale, the Taylor (l_{T}) and Kolmogorov (η_{K}) length scales can also be used to quantify the turbulent flow characteristics and are given by

$$l_{\mathrm{T}} = \Lambda \left(\frac{u'\Lambda}{\nu}\right)^{-\frac{1}{2}} = \Lambda Re_{\mathrm{T}}^{-\frac{1}{2}}, \tag{1.13}$$

$$\eta_{\mathrm{K}} = \left(\frac{\nu^3}{\epsilon}\right)^{\frac{1}{4}} = \Lambda \left(\frac{u'\Lambda}{\nu}\right)^{-\frac{3}{4}} = \Lambda Re_{\mathrm{T}}^{-\frac{3}{4}}, \tag{1.14}$$

where $\epsilon = u'^3/\Lambda$ [6, 72]. Please note that other than the formulation introduced for Taylor length scale (Eq. (1.13)), there is another formulation ($l_{\mathrm{T}} = \sqrt{15}\Lambda Re_{\mathrm{T}}^{-1/2}$) for this length scale as well, which can be found in [5, 73]. The definition provided in Eq. (1.13) is used in this thesis for estimation of the Taylor length scale. Taylor and Kolmogorov length scales can also be estimated based on the reaction zone temperature (at about 1500 K). Specifically, Taylor (${l_{\mathrm{T}}}^*$) and Kolmogorov (η^*) length scales estimated based on the reaction zone temperature can be calculated using

$${l_{\mathrm{T}}}^* = \Lambda \left(\frac{u'\Lambda}{\nu^*}\right)^{-\frac{1}{2}}, \tag{1.15}$$

$${\eta_{\mathrm{K}}}^* = \Lambda \left(\frac{u'\Lambda}{\nu^*}\right)^{-\frac{3}{4}}, \tag{1.16}$$

where ν^* is the kinematic viscosity of the reactants estimated at 1500 K.

In addition to the above length scales, the relative characteristic velocity of the turbulent flow to the laminar flame speed also dictates the quality of turbulence and flame interaction. Several studies (see for example [5, 6, 8, 74]) used $u'/S_{\mathrm{L},0}$ and $\Lambda/\delta_{\mathrm{L}}$ to predict the general

flame characteristics. Specifically, Borghi [74] and Peters [5] developed a regime diagram, referred to as the Borghi-Peters diagram, to categorize the premixed flames. A modified version of this diagram is shown in Fig. 1.3. As can be seen, premixed flames with $\frac{u'\Lambda}{S_{\mathrm{L},0}\delta_{\mathrm{L}}} \lesssim 1$ are laminar and those with $\frac{u'\Lambda}{S_{\mathrm{L},0}\delta_{\mathrm{L}}} \gtrsim 1$ are turbulent. The turbulent premixed flames with $u' \lesssim S_{\mathrm{L},0}$ are referred to as the wrinkled flames [5, 52]. For these flames, eddies rotational velocity is relatively small compared to the laminar flames speed and they can only slightly wrinkle the flame front [5, 52]. $u'/S_{\mathrm{L},0}$ and $\Lambda/\delta_{\mathrm{L}}$ are utilized to define a parameter referred to as the Karlovitz number (Ka), which is given by [5, 6, 52]

$$Ka = \frac{\tau_{\mathrm{f}}}{\tau_{\eta_{\mathrm{K}}}} = \left(\frac{u'}{S_{\mathrm{L},0}}\right)^{\frac{3}{2}} \left(\frac{\Lambda}{\delta_{\mathrm{L}}}\right)^{-\frac{1}{2}}, \tag{1.17}$$

where τ_{f} and $\tau_{\eta_{\mathrm{K}}}$ are the flame and Kolmogorov time scales, respectively [5, 75]. $u'/S_{\mathrm{L},0}$ and $\Lambda/\delta_{\mathrm{L}}$ are also used to define another non-dimensional parameter for characterizing the turbulent flames, which is referred to as the Damköhlder number (Da) [52, 75]

$$Da = \left(\frac{u'}{S_{\mathrm{L},0}}\right)^{-1} \left(\frac{\Lambda}{\delta_{\mathrm{L}}}\right). \tag{1.18}$$

The turbulent premixed flames with $u' \gtrsim S_{\mathrm{L},0}$ and $Ka \lesssim 1$ are categorized as the corrugated flames and feature both wrinkled flame surfaces and pockets [5, 51, 52]. However, both preheat and reaction zones are thin for the flames categorized in this regime [5, 76–78].

It is hypothesized [5, 52] that flames with $1 \lesssim Ka \lesssim 100$ should feature broadened preheat zones as turbulent eddies are small enough to penetrate into the preheat zone while the reaction zone remains thin. However, for $1 \lesssim Ka \lesssim 100$, the results reported in the literature for the preheat zone thickness are contradictory. On one hand, experimental [8, 36, 70, 79–82] and DNS studies [83, 84] show that the preheat zone may broaden for $Ka \gtrsim 1$; however, on the other hand, several other studies [8, 77, 85–87] suggest that the preheat zone may not broaden for $Ka \gtrsim 1$. The reason for this discrepancy is elaborated in [6, 8].

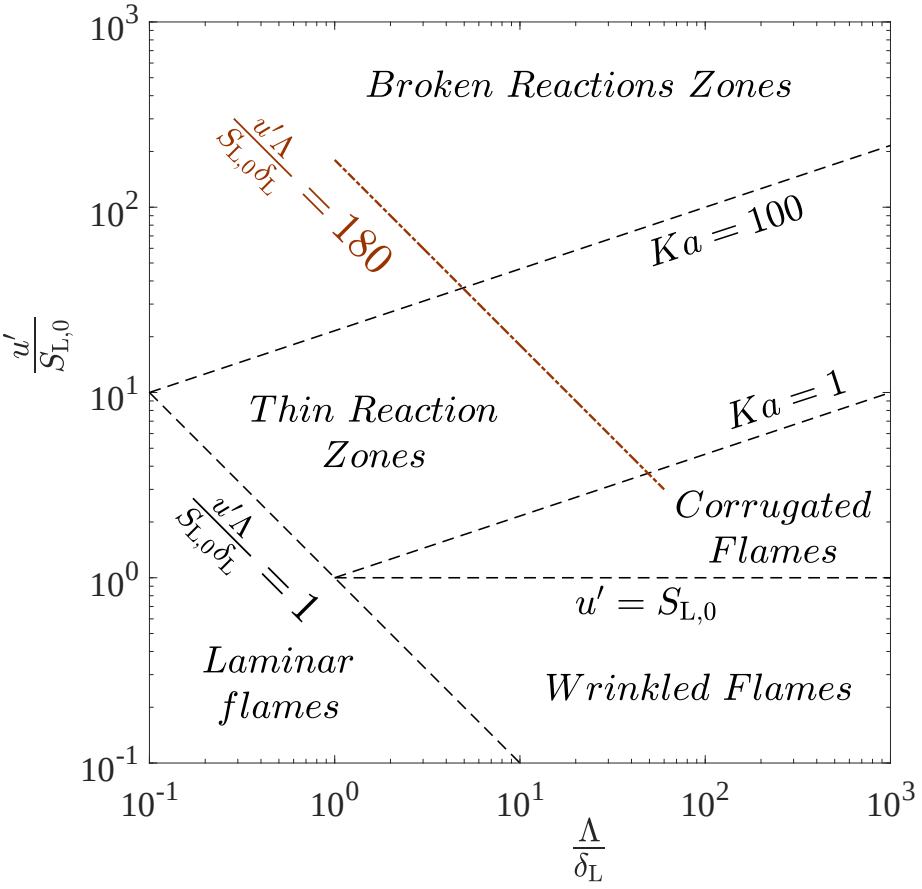

Fig. 1.3. Borghi–Peters diagram [5, 6].

Driscoll et al. [6] and Skiba et al. [8] argue that turbulent eddies pertaining to the flames with $Ka \gtrsim 1$ should feature sufficient turbulent kinetic energy allowing them to penetrate and broaden the preheat zone. Skiba et al. [8] and Driscoll et al. [6] experimentally showed that, in addition to $Ka \gtrsim 1$, flames should feature $u'\Lambda/(S_{L,0}\delta_L) \gtrsim 180$ for their preheat zone to be broaden. The suggested border of $u'\Lambda/(S_{L,0}\delta_L)$ is shown by the dotted-dashed brown line in Fig. 1.3.

For flames with $Ka \gtrsim 100$, the reaction zone is also expected to feature broadening as eddies are small enough to be able to penetrate into this zone [5, 52]. Similar to the preheat zone, the results reported in the literature regarding the turbulent flames reaction zone thickness are also contradictory. Experimental investigation [8] and DNS of [88–90] show that the reaction zone remains thin upto $Ka \approx 550$ and 1000, respectively. In contrast to the studies of [8, 88–90], those of [12, 36, 37, 43–49] suggest that the reaction zone is, in

fact, broadened compared to the laminar flame counterpart. The underlying reason for the contradiction between the results of [8] and [36, 37, 43–46] are discussed in [6, 8]. Driscoll and co-workers [6, 8] argue that the burners utilized in the studies of [36, 37, 43–46] feature very small diameters (1.5–4 mm) and very large mean bulk flow velocities (200–418 m/s). For such flows, the background turbulence is primarily driven by the jet shear layers, as such, their [36, 37, 43–46] results cannot be compared with those of [8]. To the best of the author knowledge, no experimental investigation has demonstrated existence and/or characterized the broadened reaction zones of extremely turbulent premixed flames generated by relatively large exit diameter Bunsen burners.

1.2.4 Turbulent burning velocity

Driscoll et al. [34] reviewed three definitions of the burning velocity, which are discussed here. First, the burning velocity can be defined based on the speed of the reactants consumption. Using this, the burning velocity is defined as the rate at which the reactants convert to combustion products [34]. This consumption speed can be estimated globally and locally, which are referred to as the global ($S_{\mathrm{T,GC}}$) and local ($S_{\mathrm{T,LC}}$) consumption speeds, respectively [6, 34]. These speeds are estimated using [6, 11, 34]

$$S_{\mathrm{T,GC}} = \frac{\dot{m}_{\mathrm{r}}}{\rho_{\mathrm{r}} \overline{A}_{\mathrm{f}}}, \tag{1.19a}$$

$$S_{\mathrm{T,LC}} = \frac{S_{\mathrm{L},0} I_0}{L_\xi} \int_{-\infty}^{\infty} \int_{-\infty}^{\infty} \Sigma(\eta, \xi) \mathrm{d}\eta \mathrm{d}\xi, \tag{1.19b}$$

where $\dot{m}_{\mathrm{r}}$ and ρ_{r} are the reactants mass flow rate and density. $\overline{A}_{\mathrm{f}}$ is the flame surface area estimated based on the mean progress variable ($\overline{c}_{\mathrm{OH}}$). To estimate the mean progress variable, mean of the binarized (zero for reactants and one for products) OH PLIF images (mole fraction fields) is usually used [11, 12, 91, 92]. In order to help illustrate this, 500 images of a sinusoidally curved two-dimensional flame were generated artificially using the data

corresponding to a freely propagating laminar methane-air flame with $\phi = 0.7$. Then, the curved flame was positioned randomly in the two-dimensional space. The two-dimensional OH and CH_2O synthetic PLIF data were estimated using the mole fractions of OH and CH_2O and temperature pertaining to the the freely propagating laminar flame as well as Eq. (1.10). OH and CH_2O synthetic PLIF signals for a representative frame of the synthetically generated two-dimensional flame are presented in Figs. 1.4(a) and (b), respectively. A threshold was utilized to binarize the OH contours. This threshold was selected using the laminar freely propagating flame data. As can be seen in Fig. 1.2, the location of the flame front (maximum of the heat release rate) corresponds to about 30% of the normalized OH PLIF signal (mole fraction). Thus, 30% of the normalized OH PLIF signal was selected as the threshold for binarizing the OH contours. The binarized OH contour for the representative frame of the synthetically generated two-dimensional flame is shown in Fig. 1.4(c). These contours were averaged over the 500 frames to obtain $\overline{c}_{\mathrm{OH}}$. Fig. 1.4(d) show the corresponding $\overline{c}_{\mathrm{OH}}$ for the synthetically generated flame.

In Eq. (1.19b), η and ξ are the curvilinear axes, which are respectively normal and tangent to a given $\overline{c}_{\mathrm{OH}}$ contour (usually $\overline{c}_{\mathrm{OH}} = 0.5$) and L_ξ is the length of the mean progress variable contour. For example, for the synthetically generated flame, $\overline{c}_{\mathrm{OH}} = 0.5$ contour is highlighted with a green solid curve in Fig. 1.4(d). Also, at a given point such as "P" on $\overline{c}_{\mathrm{OH}} = 0.5$ curve, η and ξ axes are presented for demonstration. In Eq. (1.19b), Σ is the flame surface density obtained using the procedure discussed in the following. Figure 1.4(e) shows the flame front (see curve "L") for the representative frame of the synthetically generated flame. In order to calculate the flame surface density, for a given point in the domain of investigation (such as "O"), an interrogation window (window "W") with a size of 1.5×1.5 mm^2 is considered. Please note that conclusions of this study are not sensitive to the selected interrogation size. The flame surface density is estimated by dividing the length of the flame front within the interrogation window shown in Fig 1.4(e)

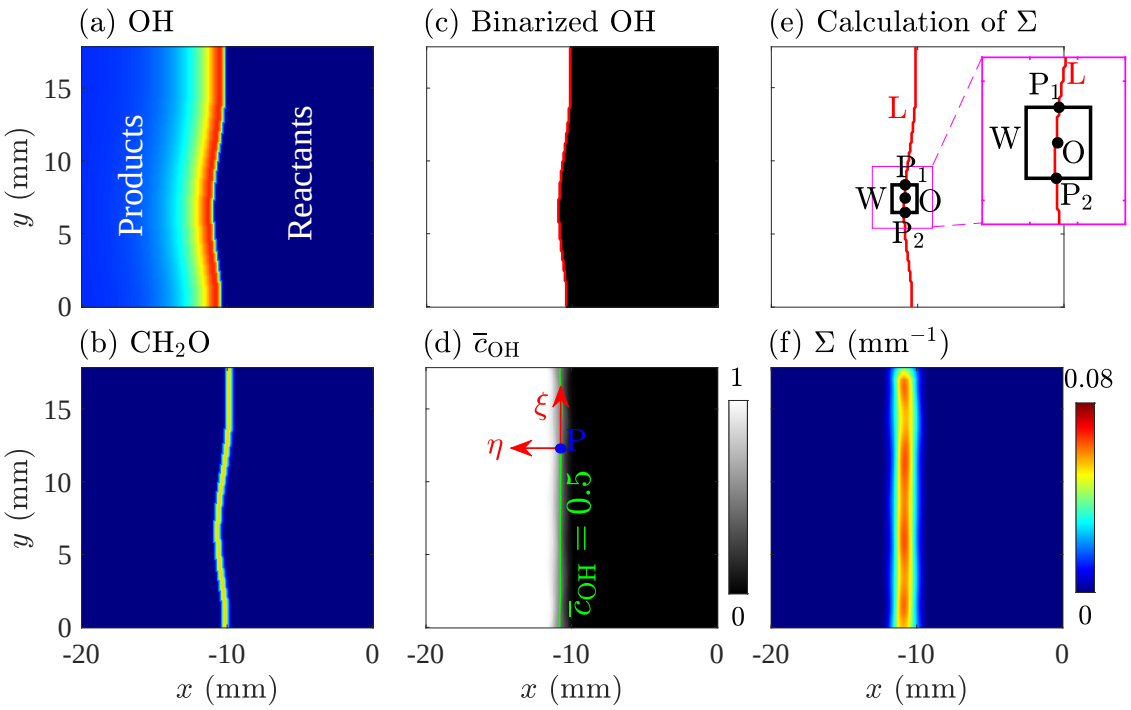

Fig. 1.4. (a) OH and (b) CH_2O synthetic PLIF signals for a representative frame of synthetic two-dimensional flame. (c) and (d) are the binarized OH and $\overline{c}_{OH}$ contours. (e) represents the procedure for estimation of flame surface density. (f) Flame surface density for the synthetic two-dimensional flame.

by the area of the window. Specifically, the flame surface density at point "O" in Fig. 1.4(e) is calculated using

$$\Sigma = \frac{L_{P_1P_2}}{A_W}, \tag{1.20}$$

where $L_{P_1P_2}$ is the length of a portion of the line "L", which is inside the interrogation window ($\widehat{P_1P_2}$), and A_W is the area of window "W". Figure 1.4(f) shows the averaged flame surface density obtained based on 500 frames for the synthetically generated flame with the window size of 1.5×1.5 mm^2.

In Eq. (1.19b), I_0 is the Bray-Cant [93] stretch factor, and is defined as the ratio of the laminar flame speed (S_L) to the unstretched laminar flame speed ($S_{L,0}$) obtained for the corresponding freely propagating laminar flame. The stretch factor can be estimated using the following equation [34, 94]

$$I_0 = \frac{S_L}{S_{L,0}} = 1 - \frac{\mathcal{L}}{r_c}, \tag{1.21}$$

where $\mathcal{L}$ is the Markstein length and r_c is the local radius of the flame front curvature. The Markstein length depends on the reactants chemistry [95, 96]. For lean methane-air [95] and hydrogen-air flames [96], which are relevant to those investigated in this dissertation, the Markstein length is relatively small compared to r_c (this is obtained based on the probability density functions of the curvature in Fig. 8 of [97], which is obtained for the flames with large Karlovitz numbers). As a result, it is acceptable to assume I_0 is close to unity for lean hydrogen-enriched methane-air mixtures that feature near unity Lewis numbers, see for example [6, 11].

Compared to the above definition, the burning velocity can also be defined as the speed at which a flame leading edge moves towards the gas flow. This burning velocity is referred to as the displacement speed ($S_{T,LD}$) and equals to the relative speed of the flame edge compared to the gas flow velocity in the direction normal to the leading edge. That is $S_{T,LD} = (\mathbf{V}_{FLAME} - \mathbf{V}_{GAS})_{LE}.\mathbf{n}_{LE}$, where $\mathbf{V}_{FLAME}$ and $\mathbf{V}_{GAS}$ are the velocity vectors of the flame and gas, respectively, and "LE" indicates that measurements are at the location of the flame leading edge. $\mathbf{n}_{LE}$ is the unit vector in the direction of the normal to the flame leading edge [34]. In this thesis, the former definition of the burning velocity (i.e. the consumption speed based burning velocity) is utilized.

As reviewed in Driscoll et al. [6, 34], there are two ongoing questions regarding the global and local consumption speeds of the methane-air turbulent premixed flames in the literature. First, the DNS studies of [97–99] suggest that increasing the turbulence intensity increases the flame surface area such that the local consumption speed nearly equals the global consumption speed. However, several other studies, see for example [6, 9–12, 14, 100, 101], suggest that as the turbulence intensity increases, the global consumption speed increases, but the flame surface area and the local consumption speed plateau. For instance, Wabel et al. [11] show that, at $u'/S_{L,0} \approx 150$, the global consumption speed is about 5 times the local consumption speed. They. [11] speculated that, as the preheat zone broadens with

increasing the turbulence intensity, the turbulent diffusivity of the gas in this zone increases, enhancing the transport of reactants and as a result increase of the global consumption speed. This enhancement is not considered in the formulation of the local consumption speed (see Eq. (1.19b)), which can be the reason for the difference observed between the local and global consumption speeds [6]. It is shown [12, 36, 37, 43–49] that, in addition to the preheat zone, the reaction zone also broadens with increasing the turbulence intensity, which may also contribute to the increase of the gas diffusivity. Both Gülder [10] and Nivarti et al. [9] performed theoretical calculations and showed that the enhancement of gas diffusivity inside the flame region can allow for elaborating the reason for the increase of the global consumption speed with increasing the turbulence intensity and as a result the difference between the local and global consumption speed values reported in for example [6, 9–12, 14, 100, 101]. Specifically, study of Gülder [10] suggests that the ratio of the global and local consumption speeds can be obtained using

$$\frac{S_{\mathrm{T,GC}}}{S_{\mathrm{T,LC}}} = \left[1 + ScRe_{l_{\mathrm{T}}}^{\frac{1}{2}}\right] \frac{\delta'_{\mathrm{L}}}{l_{\mathrm{T}}}, \tag{1.22}$$

where Sc and l_{T} are the Schmidt number and the Taylor length scale (see Eq. (1.13)), respectively. The Reynolds number estimated based on the Taylor length scale is given by $Re_{l_{\mathrm{T}}} = u' l_{\mathrm{T}}/\nu$, where ν is the reactants kinematic viscosity estimated at 300 K. δ'_{L} is the laminar flame thickness calculated using the reactant thermophysical properties estimated at 300 K (compared to δ_{L} in Eq. (1.4), which is estimated at the reaction zone temperature). Compared to Gülder [10], Nivarti et al. [9] proposed the following equation for the ratio of the global and local consumption speeds.

$$\frac{S_{\mathrm{T,GC}}}{S_{\mathrm{T,LC}}} = \left(1 + Ka^{\frac{2}{3}}\right)^{\frac{1}{2}}. \tag{1.23}$$

In both Gülder [10] and Nivarti et al. [9], the preheat and reaction zones thicknesses are

not measured; and, as a result, it is not known whether the enhancement of gas diffusivity is due to the broadening of only the preheat zone or both the preheat and reaction zones. This requires further investigations.

The second question is related to the behavior of the global consumption speed itself with changing the turbulence intensity. As hypothesized by Damköhler [6, 18], also known as the Damköhler's first hypothesis, increasing $u'/S_{\mathrm{L},0}$ is expected to increase the global consumption speed linearly. This is given by

$$\frac{S_{\mathrm{T,GC}}}{S_{\mathrm{L},0}} = 1 + \frac{u'}{S_{\mathrm{L},0}}. \tag{1.24}$$

Similarly, studies of [15, 102] suggest linear relations exist between $S_{\mathrm{T,GC}}/S_{\mathrm{L},0}$ and $u'/S_{\mathrm{L},0}$. Specifically, Bradley [15] proposed that, in the absence of flame stretch, the normalized global consumption speed can be obtained from

$$\frac{S_{\mathrm{T,GC}}}{S_{\mathrm{L},0}} = 1.5\frac{u'}{S_{\mathrm{L},0}}. \tag{1.25}$$

Also, the study of Lewis and Von Elbe [102] suggests

$$\frac{S_{\mathrm{T,GC}}}{S_{\mathrm{L},0}} = \sqrt{1 + \left(\frac{2u'}{S_{\mathrm{L},0}}\right)^2}, \tag{1.26}$$

which simplifies to a nearly linear variation at large turbulence intensities, which is given by

$$\frac{S_{\mathrm{T,GC}}}{S_{\mathrm{L},0}} \approx 2\frac{u'}{S_{\mathrm{L},0}}. \tag{1.27}$$

Compared to the results discussed above, studies of [6, 11, 12, 78, 101, 103] show that, at relatively intense turbulence conditions, the global consumption speed plotted against the turbulence intensity bends towards the axis of $u'/S_{\mathrm{L},0}$. This is referred to as the bending behavior in the literature, see for example [6, 11, 12, 78, 101, 103]. Considering the non-

linear nature of the burning velocity, several studies proposed models for prediction of the global consumption speed. For example, Yakhot [17] utilized the flame front location and the velocity fluctuations field to estimate $S_{\mathrm{T,GC}}$ and suggested

$$\frac{S_{\mathrm{T,GC}}}{S_{\mathrm{L},0}} = \exp\left(\frac{\left(\frac{u'}{S_{\mathrm{L},0}}\right)^2}{\left(\frac{S_{\mathrm{T,GC}}}{S_{\mathrm{L},0}}\right)^2}\right). \tag{1.28}$$

Ronney and Yakhot [16] modified the model developed by Yakhot [17] and took into account the effect of the flame broadening. They [16] suggested that the normalized global consumption speed is given by

$$\frac{S_{\mathrm{T,GC}}}{S_{\mathrm{L},0}} = \left(X_{\mathrm{R}}^2 - 2X_{\mathrm{R}} + 2\right)^{\frac{1}{2}} \exp\left(\frac{1 - n_{\mathrm{R}}^{\frac{2}{3}} Re_{\mathrm{R}}^{-\frac{1}{2}} X_{\mathrm{R}} \frac{u'}{S_{\mathrm{L},0}}}{1 - n_{\mathrm{R}}^{\frac{2}{3}} Re_{\mathrm{R}}^{-\frac{1}{2}} \frac{S_{\mathrm{T,GC}}}{S_{\mathrm{L},0}}}\right), \tag{1.29}$$

where Re_{R} is

$$Re_{\mathrm{R}} = \sqrt{\frac{Re_{\mathrm{T}}^2}{0.471\left(1 - \left(\frac{\eta_{\mathrm{K}}}{\Lambda}\right)^{\frac{2}{3}}\right)}}, \tag{1.30}$$

and n_{R} is calculated utilizing

$$n_{\mathrm{R}} = \frac{\frac{\eta_{\mathrm{K}}}{\Lambda}}{Re_{\mathrm{R}}^{-\frac{3}{4}}}. \tag{1.31}$$

In Eq. (1.29), X_{R} is determined by solving

$$\left(28.1 A_{\mathrm{R}}^{-2}\left(1 - n_{\mathrm{R}}^{\frac{2}{3}} Re_{\mathrm{R}}^{-\frac{1}{2}}\right)\right) X_{\mathrm{R}}^3 - X_{\mathrm{R}}^2 + 2X_{\mathrm{R}} - 2 = 0, \tag{1.32}$$

where A_{R} is set to 6 in [16].

Peters [14] considered influence of the small and large scale turbulence on flame surface area and developed an analytical model for estimation of the global consumption speed. This model suggests that the global consumption speed can be obtained using [14]

$$\frac{S_{\mathrm{T,GC}}}{S_{\mathrm{L},0}} = 1 - \frac{0.39}{2}\frac{\Lambda}{\delta_{\mathrm{L}}} + \left(\left(\frac{0.39}{2}\frac{\Lambda}{\delta_{\mathrm{L}}}\right)^2 + 0.78\frac{u'\Lambda}{S_{\mathrm{L},0}\delta_{\mathrm{L}}}\right)^{\frac{1}{2}}. \tag{1.33}$$

Compared to [14, 16, 17], Kobayashi [13] and Wabel et al. [11] obtained empirical models for estimating the global consumption speed. Specifically, Kobayashi [13] proposed the following equation for calculation of the global consumption speed, which can be used to estimate the burning velocity at the given pressures of P.

$$\frac{S_{\mathrm{T,GC}}}{S_{\mathrm{L},0}} = 2.9 \left[\left(\frac{P}{P_0} \right) \left(\frac{u'}{S_{\mathrm{L},0}} \right) \right]^{0.38}, \tag{1.34}$$

where P_0 is the atmospherics pressure. Wabel et al. [11] suggested that

$$\begin{aligned} \frac{S_{\mathrm{T,GC}}}{S_{\mathrm{L},0}} &= \sqrt{1 + c_1 \left(\frac{u'}{S_{\mathrm{L},0}} \right)^2} \left(\frac{c_2}{c_2 + \frac{u'}{S_{\mathrm{L},0}}} \right) \\ &\times \left(1 + c_3 \sqrt{\left(\frac{u'}{S_{\mathrm{L},0}} \right) \left(\frac{\Lambda}{\delta_{\mathrm{P,L},0}} \right) \left(\frac{\Lambda'}{\delta_{\mathrm{P,L},0}} \right)} \left(\frac{\delta_{\mathrm{P}}}{\delta_{\mathrm{P,L},0}} - 1 \right) \right), \end{aligned} \tag{1.35}$$

where Λ' is the transverse integral length scale, which is equated to the slot width of the turbulence generating plate in [11]. In Eq. (1.35), $c_1 = 1.01$, $c_2 = 22.6$, and $c_3 = 3.21 \times 10^{-5}$ are empirical constants set to fit the prediction of Eq. (1.35) to the results of experiment in [11]. In the literature, several reasons such as nonlinear variation of gas diffusivity with the turbulence intensity [6, 9, 18, 52] as well as the flame quenching [15, 41, 104, 105] are suggested to elaborate the non-linear behavior of the bending phenomenon. However, a potential relation between the flame quenching (or extinction) and the bending behavior has not been studied.

1.2.5 Effect of the hydrogen enrichment on turbulent premixed flames

In spite of the emerging interest in the hydrogen-enriched methane combustion, there exist limited number of studies in the literature that used hydrogen-enriched methane-air premixed flames. Thus, the effect of hydrogen-enrichment on turbulent premixed flames is not well understood and further investigations are required. Compared to methane, hydrogen has a larger reactivity, which increases the laminar flame speed [27, 106–109].

This facilitates operation of gas turbine engines at leaner conditions and larger reactants bulk flow rates [25, 27, 110–114]. In the following, the existing knowledge regarding the flame structure and burning velocity of hydrogen-enriched methane-air turbulent premixed flames are reviewed.

The internal structure of hydrogen-enriched turbulent methane-air premixed flames has been recently investigated in Zhang et al. [115]. They [115] studied both the preheat and reaction zone thicknesses variations with varying the hydrogen-enrichment percentage (up to 60%) and turbulence intensity ($u'/S_{L,0}$ varying between 3 and 12.5). They [115] showed that, similar to the methane-air turbulent premixed flames, increasing the turbulence intensity can lead to broadening of the hydrogen-enriched methane-air flames preheat zone. However, Zhang et al. [115] showed that the reaction zone thickness does not change by increasing the turbulence intensity. Although the study of [115] provides insight into the internal structure of hydrogen-enriched methane-air premixed flames at relatively moderate turbulence intensities, the preheat and reaction zone thicknesses of these flames pertaining to relatively intense turbulence conditions remain to be investigated.

Few experimental investigations [106, 116] have studied the effect of hydrogen-enrichment on the local and global consumption speeds of turbulent premixed flames. Both Halter et al. [106] and Guo et al. [116] showed that increasing the hydrogen-enrichment percentage increases the global consumption speed normalized by the unstretched laminar flame speed. Results of Guo et al. [116] suggest that the normalized global consumption speed also increases with increasing the turbulence intensity. The values of the local consumption speed are not reported in [106], however, Guo et al. [116] showed that increasing both the hydrogen-enrichment percentage and the turbulence intensity increase the local consumption speed normalized by the unstretched laminar flame speed. Although these studies [106, 116] elaborated the effect of the hydrogen-enrichment and turbulence intensity on the local/global consumption speeds, their investigations are performed for $u'/S_{L,0} \lesssim 5$. For larger turbu-

lence intensities, values of the local and global consumption speeds for hydrogen-enriched methane-air premixed flames remain to be measured.

1.3 Objectives

This thesis aims to address six objectives. Although past studies related to the heat release rate [8, 36, 43, 53–55, 61, 70, 77, 79, 117–122] provide a significant insight into the internal structure of the turbulent premixed methane-air flames, influence of hydrogen-enrichment on the preheat and reaction zones is unknown and remains to be investigated, especially at large turbulence intensities. Even for the methane-air flames, most studies in the literature are limited to the small and moderate turbulence intensities and there exist contradictory results regarding the broadening of preheat and reaction zones at large turbulence intensities. Also, the reason for the potential broadening of the preheat and reaction zones is not well understood. Thus, the first objective of the present dissertation is to measure the preheat and reaction zone thicknesses of hydrogen-enriched methane-air premixed flames pertaining to relatively intense turbulence conditions. To the author's best of knowledge, such information is not available in the literature. To achieve the above goal, an accurate method should be used to estimate the spatial variation of the heat release rate for the premixed flames, since the reaction zone thickness depends on the heat release rate structure. While there exist models in the literature (see for example [59, 67]) for visualizing the preheat and reaction zones of the pure methane-air flames, a framework should be developed to track the heat release rate in hydrogen-enriched methane-air flames. In this thesis, it is aimed to develop a mathematical model that allows estimating the heat release rate of hydrogen-enriched methane-air flames.

Deviation of the premixed flames from the flamelet behavior (non-flamelet behavior) can be studied using both broadening of the preheat and reaction zones as well as the variations of chemical spices within the flame region versus temperature [6]. The former is

related to the first objective of this study discussed earlier while the latter is experimentally challenging since it requires conducting simultaneous PLIF of the chemical species and, for example, Rayleigh scattering (for temperature measurement). The second objective of this thesis is to develop a method that allows for quantifying the non-flamelet behavior of turbulent premixed flames using only the OH and CH_2O PLIF signals (without measuring the temperature). Using the proposed method, the non-flamelet behavior is quantified for the premixed flames to investigate its relation with the broadening of the preheat and reaction zones.

After quantifying the preheat and reaction zone thickness as well as the non-flamelet behavior, it is of significant importance to understand the reason for the potential broadening of the preheat and reaction zones as well as the non-flamelet behavior. The third objective of this dissertation is to elaborate the reason for the potential broadening of the flames and the non-flamelet behavior using local turbulent flow measurements (such as measuring vorticity and swirling strength). This has been a matter of debate over the past several decades in combustion science.

Potential broadening of the preheat and reaction zones and as a result the non-flamelet behavior has implications for how fast highly turbulent hydrogen-enriched methane-air premixed flames burn. Specifically, the flamelet based models for calculation of the burning velocity can no longer be used provided there exists a considerable amount of the reaction zone broadening. The fourth objective of this thesis is to develop a framework for estimation of a heat release rate marker that does not rely on the flamelet assumption. Then, using this framework, the thesis aims to discuss reasons for the difference between the local and global consumption speeds reported in the literature. The fifth objective of the present thesis is to characterize the bending behavior reported in the literature and to develop a mathematical formulation that allows for estimating the amount of bending.

Relatively large background turbulence intensities can lead to flame extinction events,

surrounding air entrainment, and as a result reactants dilution, which can change the flame structure and burning velocity. Although some past investigations, see for example [8, 121], considered mitigating the reactants dilution using a large pilot flame (referred to as back-support), several past investigations in experimental turbulent premixed combustion research did not utilize a back-support or their back-support could not surround the entire flame, see for example [1, 36]. Thus, the lack of back-support can lead to air entrainment and flame extinction as suggested by studies of [8, 43, 123]. This is speculated to locally dilute the reactants (decrease the fuel-air equivalence ratio) and lead to stratification of the reactants [49, 124, 125]. This may locally decrease the burning velocity and the adiabatic flame temperature, and increase the local turbulence intensity and Karlovitz number, which may contribute to the broadening of the preheat and reaction zones [6, 49]. Nevertheless, further investigations are required to study the influence of the lack of back-support and the resultant flame extinction on the flame structure and burning velocity. Addressing this question is challenging since the flame extinction, itself, is usually influenced by varying background turbulent flow characteristics in past studies. The last objective of the present dissertation is to investigate the influences of lack of back-support on both flame structure and burning velocity by keeping the background turbulence unchanged.

1.4 Outline

In the following, the outline and chapter-by-chapter content of the dissertation are summarized.

Chapter 1: Introduction

In this chapter, motivation for the current dissertation was discussed first. Then, the relevant background was reviewed to highlight the existing knowledge gaps in the literature. Specifically, internal structure of a laminar flame was illustrated, the planar laser-induced

fluorescence method for estimating the premixed flames heat release rate were discussed, and the knowledge related to turbulent premixed flames internal structure as well as the burning velocity was reviewed. This was followed by the review of literature related to the influence of hydrogen-enrichment on both internal structure and burning velocity of the premixed flames. Finally, the knowledge gaps and the objectives of the thesis were discussed.

Chapter 2: Experimental methodology

The experimental setup including the burner, the turbulence generators, and the co-flow setting are discussed in this chapter. Then, the utilized diagnostics are explained. Several diagnostics are used to study the premixed flames tested in this thesis. Simultaneous planar laser-induced fluorescence of hydroxyl radical and formaldehyde molecule are utilized to study the internal structure, burning velocity, and heat release rate marker of the premixed flames. Stereoscopic particle image velocimetry is used to obtained the velocity of the non-reacting and reacting flows (simultaneous with PLIF of OH and CH_2O) to characterize the turbulent flow and explore the underlying reasons for the potential broadening of the premixed flames preheat and reaction zones. This is followed by the coordinate system utilized in this dissertation. Finally, the tested conditions are presented.

Chapter 3: Data reduction

In this chapter, first, a new model is proposed that allows for estimating the hydrogen-enriched methane-air flames local heat release rate based on the OH and CH_2O PLIF data. Then, the procedure for reducing the raw PLIF data and generating processed OH and CH_2O PLIF signals are explained. The method for calculating the preheat and reaction zone thicknesses is also illustrated in this chapter. Finally, the potential errors and uncertainties regrading the calculation of these thicknesses are discussed. Specifically, effects of image filtering, three-dimensional orientation of a flame, imaging resolution, optical blur, and

laser sheet thickness on the estimation of the preheat and reaction zone thicknesses are discussed.

Chapter 4: Structure of turbulent premixed flames at large turbulence intensities

The internal structure of hydrogen-enriched methane-air flames at large turbulence intensities is studied in this chapter. The preheat and reaction zone thicknesses are obtained for the flames with $u'/S_{\mathrm{L},0}$ up to 44.6, Karlovitz number up to 76.0, and with up to 70% of hydrogen-enrichment by volume. Then, a framework is developed and tested for quantifying potential non-flamelet behavior of the premixed flames. Finally, the correlation between the local turbulent flow characteristics and flame structure is investigated. Specifically, vorticity, swirling strength, and specific kinetic energy are obtained for the vortices and the underlying reasons for the potential broadening of the preheat and the reaction zones are investigated. Influences of the turbulence generating mechanism on the turbulent flow characteristics and the flame internal structure are discussed in this chapter.

Chapter 5: Burning velocity of turbulent premixed flames at large turbulence intensities

This chapter is related to the burning velocity of hydrogen-enriched methane-air premixed flames. Local consumption speed is calculated for the tested premixed flames and is compared with those exist in the literature. The local consumption speed formulation takes into account the flamelet assumption, which considers a thin reaction zone structure for the premixed flames. Thus, a potential broadening of the reaction zone and the non-flamelet behavior lead to an inaccurate estimation of the burning velocity based on the local consumption speed formulation. To address this problem, a new formulation and parameter, which do not take into account the flamelet assumption, are proposed for estimating the

burning velocity of the hydrogen-enriched methane-air flames. This parameter is referred to as the heat release rate marker. The values of the normalized (by that of the corresponding laminar flame) heat release rate marker are compared with those of the normalized global consumption speeds from the literature, which are also not dependent on the flamelet assumption. Then, in this chapter, the reason for the discrepancy between the normalized local and global consumption speeds (normalized heat release rate marker) values in the literature is discussed. Also, the reason for the bending behavior of the global consumption speed/heat release rate marker is investigated and a model is proposed for estimating the burning velocity of the hydrogen-enriched methane-air turbulent premixed flames.

Chapter 6: Effect of lack back-support on the flame structure and burning velocity

In this chapter, effects of lack of back-support, air entrainment, and flame extinction on the premixed flames are investigated. To achieve this goal, the background turbulence is kept unchanged and influences of the lack of back-support and flame extinction on the values of the preheat and reaction zone thicknesses, the non-flamelet behavior, the local consumption speed, and the heat release rate marker are studied. Finally, the observed trends are analyzed and the underlying reasons for the observed trends are discussed.

Chapter 7: Conclusions

The findings relevant to Chapters 4, 5, and 6 are summarized in Chapter 7. These findings suggest solutions to some of the ongoing research questions about the internal structure and burning velocity of the hydrogen-enriched methane-air turbulent premixed flames. However, further experimental/numerical efforts are necessary and future investigations are required to improve our understand regarding the internal structure and burning velocity of these flames. Having an accurate and comprehensive understanding regarding

the hydrogen-enriched methane-air flames is necessary since it facilitates improved design of the combustors, which can enhance their performance and reduce their emissions. The recommended future steps and research directions for future studies of the hydrogen-enriched methane-air turbulent flames are presented at the end of Chapter 7.

Chapter 2

Experimental methodology

This chapter consists of four sections. In the first section, the experimental setup utilized in this thesis is elaborated. In the second section, the utilized diagnostics are presented. The coordinate system used in this dissertation is presented in the third section. Finally, the tested experimental conditions are summarized in the last section.

2.1 Experimental setup

The setup used in this thesis is a Bunsen burner identical to that utilized in the study of Tamadonfar and Gülder [85]. This burner consists of an expansion section, a settling chamber (with 5 mesh screens) for flow conditioning purposes, a contraction section, and a nozzle with exit diameter of 22.2 mm. The burner schematic and the burner nozzle technical drawing are shown in Figs. 2.1 and 2.2(a), respectively. A mixture of 75% hydrogen and 25% methane (volumetric percentages) is injected through the burner rim, generating a pilot flame, see Fig. 2.1. The volumetric flow rate of the pilot flow is only 2% of the main flow, which is small, and as a result, the pilot flame is not expected to influence the main Bunsen flames. In order to investigate the effect of the lack of back-support on the internal structure and burning rate of the premixed flames, a co-flow setup was manufactured and integrated with the Bunsen burner (see Figs. 2.1 and 2.2(a)). As can be seen in Fig. 2.1, air is injected through the co-flow setup to generate a negative back-support for the tested flames. To produce a uniform co-flow and for flow conditioning purposes, the region denoted by "CF" (which highlights the co-flow) in Fig. 2.2(a) is filled with beads. Also, two mesh

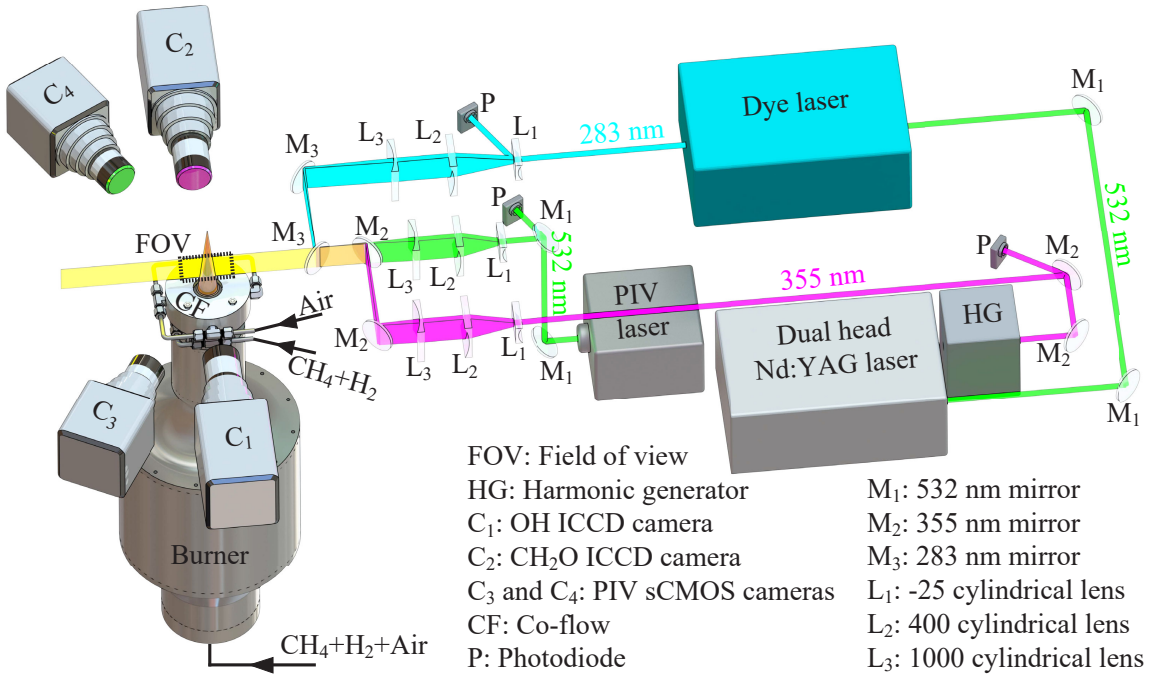

Fig. 2.1. Schematic of the experimental setup and diagnostics.

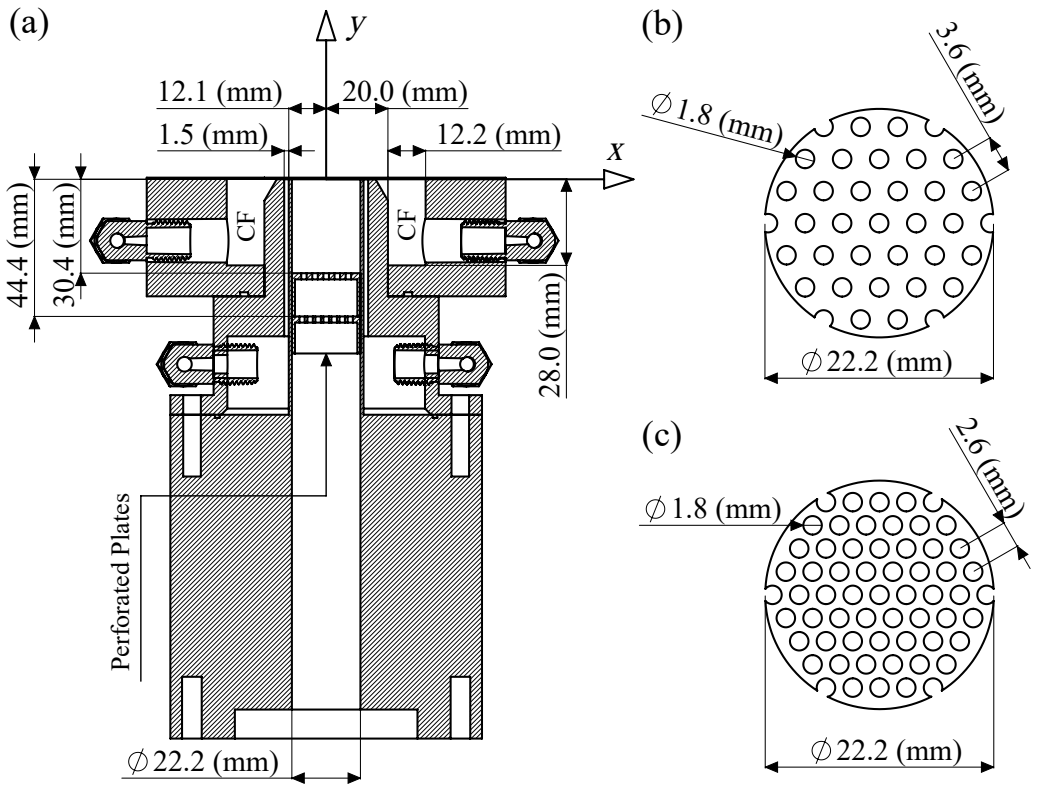

Fig. 2.2. Technical drawing of (a) the burner nozzle as well as (b and c) the perforated plates.

screens are installed on top of the co-flow setup to ensure the flow uniformity.

In order to generate a relatively wide range of turbulence intensities, three different

turbulence generating mechanisms are used. Specifically, zero, one, or two perforated plates were utilized. For the conditions with no perforated plate (which is the first turbulence generating mechanism), turbulence is primarily produced by the mesh screens as well as the Kelvin-Helmholtz instability in the jet shear layer, similar to [94, 126, 127]. For the second turbulence generating mechanism, a perforated plate with 1.8 mm circular holes arranged in a hexagonal pattern, with the technical drawing shown in Fig. 2.2(c), is placed 44.4 mm upstream of the nozzle exit plane. This plate generates a blockage ratio of 60%. For the third turbulence generating mechanism, one perforated plate (identical to that used for the second turbulence generating mechanism) is positioned 44.4 mm, and a second plate (see Fig. 2.2(b)) is located 30.4 mm upstream of the burner exit plane, see Fig. 2.2(a). The second perforated plate also has holes positioned on a hexagonal arrangement with a diameter of 1.8 mm. The blockage ratio of this plate is 77%.

2.2 Diagnostics

Simultaneous planar laser-induced fluorescence (PLIF) of hydroxyl radical (OH) and formaldehyde molecule (CH_2O) as well as simultaneous or separate stereoscopic particle image velocimetry (SPIV) were performed in this thesis. Specifically, the separate SPIV experiments in the present thesis were performed for the non-reacting flow conditions and to characterize the background turbulent flow. For pure methane-air flames, simultaneous SPIV experiments were also performed to characterize turbulent flow characteristics of the reacting flows. This section is divided into two subsections. The PLIF and SPIV diagnostics details are provided in the first and second subsections, respectively.

2.2.1 Planar laser-induced fluorescence

A dual-head Nd:YAG pump laser (Quanta Ray PIV400) and a frequency-doubled dye laser (Sirah Precision Scan) were used for the PLIF measurements. Two laser pulses with

wavelengths of 532 nm and 355±3 nm were produced by the pump laser using harmonic generators. As shown in Fig. 2.1, the 532 nm beam was used to pump the dye laser to generate a 283 nm (282.94±0.005 nm) beam, with a pulse energy and duration of about 11 mJ and 6 ns, respectively. This beam was used to excite $Q_1(6)$ line of the OH A-X system (1,0) vibrational band [67, 128–134]. The 355 nm beam was used to excite the $\tilde{A}^1A_2 - \tilde{X}^1A_1 4_0^1$ vibronic manifold of CH_2O similar to [128, 130–132, 134–137]. The pulse energy and duration of this beam were about 300 mJ and 7 ns, respectively. Using mirrors ($M_1 - M_3$) and cylindrical lenses ($L_1 - L_3$) shown in Fig. 2.1, the 283 nm and 355 nm beams were converted to coincident laser sheets with the thickness and height of about 250 μm and 40 mm, respectively. Two PIMAX ICCD cameras (see, C_1 and C_2 in Fig. 2.1), each equipped with a Nikkor UV lens and a bandpass filter with center wavelength of 320±20 nm (for OH) and Coastal Optics UV lens and a Schott GG 395 longpass filter (for CH_2O), were used to collect the PLIF signals. Data acquisition rate was set to 1 Hz for the PLIF system. The projected spatial resolution of both cameras was 89 μm per pixel. The knife edge technique [138, 139] was used to obtain the line spread functions of both cameras. It was calculated that the optical system effective resolution (the full width at half maximum of the line-spread function) is 263 μm. Image filtering was not used for estimation of this resolution. Two photodiodes, shown in Fig. 2.1, are utilized to collect pulse-to-pulse variations of the 283 nm and 355 nm beams energies, which are utilized for reduction of the PLIF data discussed in the next Chapter.

2.2.2 Stereoscopic particle image velocimetry

The SPIV system consists of a dual-cavity, double-pulse, Nd:YAG laser (BSL Twins CFR PIV200) as well as C_3 and C_4 sCMOS cameras (LaVision Imager sCMOS), which are equipped with Scheimpflug adapters and Tokina lenses, see Fig. 2.1. The laser generates pairs of 532 nm beams with a 4–33 μs separation time (depending on the tested mean bulk

flow velocity). M_1 mirror as well as $L_1 - L_3$ cylindrical lenses (see Fig. 2.1) are utilized to convert the PIV laser beams to laser sheets that are coincident with those of the PLIF lasers. The field of view and the projected spatial resolution of the SPIV cameras are 84 mm×70 mm and 29.3 μm/pixel, respectively. Data acquisition rate was set to 1 Hz for the SPIV system. Olive oil is atomized using a TSI Six-Jet atomizer, generating sub-micron droplets for the SPIV experiments. The Stokes number of the droplets depends on the tested condition (discussed later) and was estimated using the formulation provided in [94]. All estimated Stokes numbers are smaller than about 0.2, indicating that the generated droplets track the velocity fluctuations properly. Pre-processing, processing, and post-processing algorithms were implemented using LaVision DaVis 8.4 software to ensure accuracy of the generated velocity data. Specifically, a sliding minimum filter was used to remove the background first. Following this, two steps of cross-correlation were applied to the data with integration window sizes of 32×32 pixels^2 and 16×16 pixels^2. 50% overlap was used for both interrogation window sizes. Then, spurious vectors with cross-correlation peak-ratio less than 1.5 were eliminated. Finally, outlier vectors were removed using a median based filter [140] in LaVision DaVis 8.4. The vector removal generates some regions especially in the preheat zone with no velocity data. Lack of the velocity data can lead to sharp velocity gradients and as a result incorrect vorticity/swirling strength calculations. However, since the spatial locations of no-velocity data are available in the velocity post-processing step, inaccurate vorticity/swirling strength data was removed prior to further analysis. PLIF and SPIV images were registered and mapped to one physical coordinate system using a three-dimensional LaVision Type 20 target plate. LaVision DaVis 8.4 software was used to calculate the velocity vectors.

Several methods are proposed to estimate the uncertainty of the particle image velocimetry data in the past, see for example [141–146]. Two sources of error, which are related to the particle images correlation as well as the limited resolution of the SPIV measurements, are

expected to influence the reported velocity statistics in this thesis. Studies of [141, 147–150] suggest that the displacement vector calculated using the cross-correlation technique (related to the present thesis) can feature a maximum of about 0.08 pixels uncertainty pertaining to the in-plane motion of the seed particles. Using the angle between the cameras utilized in the present study along with the results of Prasad [151], it is estimated that the uncertainty related to the out-of-plane motion of the seed particles in the present study is about 0.14 pixels. Such errors in estimation of the in-plane and out-of-plane displacements of the seed particles are expected to lead to about 2 and 3% uncertainties in estimation of the corresponding velocities, respectively. The limited spatial resolution of the SPIV measurements leads to unresolved motion of turbulent eddies and as a result underestimation of the reported turbulence intensities [152–155]. In the present thesis, the smallest turbulence length scale can become about 40 times smaller than the utilized integration window size. Thus, the turbulent motion pertaining to sub-interrogation window size cannot be resolved here and this may contribute to error in estimation of the reported velocity statistics.

2.3 Coordinate system

A Cartesian coordinate system, presented in Fig. 2.3, is used in the present dissertation. The origin of the coordinate system is at the intersection of the burner centerline and the nozzle exit plane. The $x-$ and $y-$axes are at the imaging plane and lie inside the laser sheets. The $z-$axis is normal to the $x-y$ plane. The PLIF and SPIV field of views, shown by a green dashed window in Fig. 2.3, are coincident. In the figure, the flow characterization region (FCR) highlights the location at which the non-reacting turbulent flow characteristics are averaged.

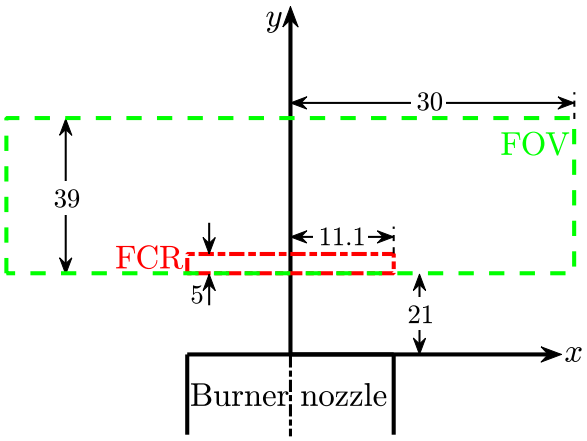

Fig. 2.3. The coordinate system, field of view, and flow characterization region (FCR). The dimensions are in mm.

2.4 Tested conditions

Two sets of experiments with the total number of 73 test conditions are performed in this thesis. The first set, which includes 68 conditions, pertain to the Bunsen flames without a co-flow. The details corresponding to these conditions are tabulated in Table 2.1. Mixture of methane (grade 2 with 99% chemical purity) and hydrogen (grade 5 with 99.999% chemical purity) is used as the fuel in this thesis. The fuel-air equivalence ratio (ϕ) for all tested conditions is 0.7. All of the test conditions labels are provided in the first column of Table 2.1. In this column, U# and H# indicate the tested mean bulk velocity (U) and the volume-based hydrogen-enrichment percentage (H_2%). Four mean bulk flow velocities of 5, 15, 25, and 35 m/s are examined, which are provided in the second column of the table. H_2% is varied from 0 to a maximum of 70%, with the corresponding values provided in the third column of Table 2.1. In the label of each tested condition, T# indicates the number of utilized perforated plates. Conditions with zero (T0), one (T1), and two (T2) perforated plates are highlighted by the blue, green, and red colors in the table, respectively. The second set of experiment includes 5 test conditions and pertain to Bunsen flames with a co-flow. Details pertaining to this set of experiments are summarized in Table 2.2. For these conditions, $U = 5$ m/s, $\phi = 0.7$, and two perforated plates are utilized with H_2%

being either 0 or 20%. In Table 2.2, C# indicates volumetric flow rate of co-flow ($\dot{Q}_{\mathrm{Co-flow}}$) in SLPM (standard liter per minute). For H_2 = 0%, 100, 200, and 300 SLPM of $\dot{Q}_{\mathrm{Co-flow}}$ were tested. A stable flame was not formed for $\dot{Q}_{\mathrm{Co-flow}}$ = 400 SLPM. For H_2 = 20%, data was only collected for $\dot{Q}_{\mathrm{Co-flow}}$ = 100 and 200 SLPM as the flame was not stable at $\dot{Q}_{\mathrm{Co-flow}}$ = 300 SLPM.

Cantera simulations [50] with the GRI-Mech 3.0 are used to estimate the unstretched laminar flame speeds ($S_{\mathrm{L},0}$). Accuracy of using GRI-Mech 3.0 for simulating laminar hydrogen-enriched methane-air flames is discussed in Appendix A. The laminar flame thicknesses (δ_{L}) are calculated using Eq. (1.4). Root Mean Square (RMS) of the velocity fluctuations along the y (u'), x (v'), and z (w') directions as well as the integral (Λ, see Eq. (1.12)), Taylor (l_{T}, see Eq. (1.13)), and Kolmogorov (η_{K}, see Eq. (1.14)) length scales are averaged within the red dotted-dashed window of Fig. 2.3, and the obtained results are presented in Tables 2.1 and 2.2. The non-reacting flows pertaining to the first turbulence generating mechanism (0 turbulence generator) feature the Kelvin-Helmholtz instability. This instability is generated by the jet shear layer, can influence the values of the RMS velocity and integral length scale, and does not correspond to the background turbulent flow. Thus, using the proper orthogonal decomposition (POD) technique [156], the Kelvin-Helmholtz modes are obtained and excluded from the non-reacting flow data pertaining to zero perforated plates (see Appendix B for more details). The turbulent Reynolds (Re_{T}), Damköhlder (Da), and Karlovitz (Ka) numbers are estimated using Eqs. (1.11), (1.18), and (1.17) with the corresponding values provided in Tables 2.1 and 2.2. The effective Lewis number (L_{eff}) of the fuel and air mixture was estimated using the formulations provided in Appendix C, with the corresponding values presented in the last columns of the Tables 2.1 and 2.2.

All test conditions related to Table 2.1 are overlaid on the Borghi-Peters [5, 74] diagram, as shown in Fig. 2.4. The results in this figure suggest that flames with U = 5 m/s and no perforated plate pertain to the wrinkled flames regime. Flames with U = 5 m/s and one

Table 2.1. Tested experimental conditions. For all conditions, $\phi = 0.7$. U, $S_{L,0}$, u', v', and w' are in m/s and δ_L, η_K, l_T and Λ are in mm. No co-flow exists for these test conditions.

	U	H_2%	$S_{L,0}$	δ_L	u'	v'	w'	η_K	l_T	Λ	u'/U	$u'/S_{L,0}$	Λ/δ_L	Re_T	Da	Ka	Le_{eff}
U5H00T0	5	0	0.19	0.33	0.15	0.04	0.07	0.23	0.48	2.1	0.03	0.8	6.4	19	8.4	0.3	1.03
U5H10T0	5	10	0.21	0.31	0.15	0.04	0.07	0.23	0.48	2.1	0.03	0.7	6.7	19	9.6	0.2	1.00
U5H20T0	5	20	0.23	0.30	0.15	0.04	0.07	0.23	0.48	2.1	0.03	0.7	7.1	19	10.8	0.2	0.97
U5H30T0	5	30	0.25	0.28	0.15	0.04	0.07	0.23	0.49	2.1	0.03	0.6	7.5	19	12.6	0.2	0.93
U5H40T0	5	40	0.27	0.26	0.15	0.04	0.07	0.24	0.49	2.1	0.03	0.5	8.1	19	15.1	0.1	0.91
U5H50T0	5	50	0.31	0.24	0.15	0.04	0.07	0.24	0.49	2.1	0.03	0.5	8.8	18	18.6	0.1	0.88
U5H60T0	5	60	0.36	0.21	0.15	0.04	0.07	0.24	0.49	2.1	0.03	0.4	9.8	18	24.8	0.1	0.87
U5H70T0	5	70	0.44	0.19	0.15	0.04	0.07	0.24	0.50	2.1	0.03	0.3	11.2	18	33.1	0.1	0.86
U15H00T0	15	0	0.19	0.33	1.70	1.36	0.54	0.04	0.19	3.9	0.11	8.7	11.9	410	1.4	7.4	1.03
U15H20T0	15	20	0.23	0.30	1.70	1.36	0.54	0.04	0.19	3.9	0.11	7.5	13.1	405	1.7	5.7	0.97
U15H40T0	15	40	0.27	0.26	1.70	1.36	0.54	0.04	0.20	3.9	0.11	6.2	15.0	397	2.4	3.9	0.91
U15H60T0	15	60	0.36	0.21	1.70	1.36	0.54	0.04	0.20	3.9	0.11	4.7	18.2	387	4.0	2.4	0.87
U25H00T0	25	0	0.19	0.33	3.24	2.46	1.26	0.03	0.14	3.9	0.13	16.6	11.9	783	0.7	19.6	1.03
U25H40T0	25	40	0.27	0.26	3.24	2.46	1.26	0.03	0.14	3.9	0.13	11.8	15.0	759	1.3	10.4	0.91
U35H00T0	35	0	0.19	0.33	3.72	2.96	1.83	0.02	0.13	3.6	0.11	19.1	11.0	829	0.6	25.1	1.03
U35H40T0	35	40	0.27	0.26	3.72	2.96	1.83	0.02	0.13	3.6	0.11	13.5	13.9	804	1.0	13.3	0.91
U5H00T1	5	0	0.19	0.33	0.34	0.25	0.30	0.13	0.36	2.7	0.07	1.7	8.3	57	4.7	0.8	1.03
U5H10T1	5	10	0.21	0.31	0.34	0.25	0.30	0.13	0.36	2.7	0.07	1.6	8.7	57	5.4	0.7	1.00
U5H20T1	5	20	0.23	0.30	0.34	0.25	0.30	0.13	0.36	2.7	0.07	1.5	9.1	56	6.0	0.6	0.97
U5H30T1	5	30	0.25	0.28	0.34	0.25	0.30	0.13	0.36	2.7	0.07	1.4	9.7	56	7.0	0.5	0.93
U5H40T1	5	40	0.27	0.26	0.34	0.25	0.30	0.13	0.36	2.7	0.07	1.2	10.5	55	8.4	0.4	0.91
U5H50T1	5	50	0.31	0.24	0.34	0.25	0.30	0.13	0.37	2.7	0.07	1.1	11.4	55	10.3	0.3	0.88
U15H00T1	15	0	0.19	0.33	0.98	0.71	0.83	0.06	0.22	2.8	0.07	5.0	8.6	173	1.7	3.9	1.03
U15H20T1	15	20	0.23	0.30	0.98	0.71	0.83	0.06	0.22	2.8	0.07	4.4	9.5	171	2.1	2.9	0.97
U15H40T1	15	40	0.27	0.26	0.98	0.71	0.83	0.06	0.22	2.8	0.07	3.6	10.9	168	3.0	2.0	0.91
U15H60T1	15	60	0.36	0.21	0.98	0.71	0.83	0.06	0.22	2.8	0.07	2.7	13.2	163	4.9	1.2	0.87
U15H70T1	15	70	0.44	0.19	0.98	0.71	0.83	0.06	0.22	2.8	0.07	2.2	15.1	160	6.6	0.9	0.86
U25H00T1	25	0	0.19	0.33	1.57	1.17	1.36	0.04	0.16	2.6	0.06	8.1	7.9	253	1.0	8.2	1.03
U25H20T1	25	20	0.23	0.30	1.57	1.17	1.36	0.04	0.16	2.6	0.06	7.0	8.7	250	1.2	6.2	0.97
U25H40T1	25	40	0.27	0.26	1.57	1.17	1.36	0.04	0.17	2.6	0.06	5.7	10.0	245	1.7	4.3	0.91
U25H60T1	25	60	0.36	0.21	1.57	1.17	1.36	0.04	0.17	2.6	0.06	4.3	12.1	239	2.9	2.6	0.87
U35H00T1	35	0	0.19	0.33	2.19	1.71	1.94	0.03	0.14	2.5	0.06	11.3	7.6	341	0.7	13.7	1.03
U35H10T1	35	10	0.21	0.31	2.19	1.71	1.94	0.03	0.14	2.5	0.06	10.5	8.0	339	0.8	12.0	1.00
U35H20T1	35	20	0.23	0.30	2.19	1.71	1.94	0.03	0.14	2.5	0.06	9.7	8.4	337	0.9	10.4	0.97
U35H30T1	35	30	0.25	0.28	2.19	1.71	1.94	0.03	0.14	2.5	0.06	8.9	9.0	334	1.0	8.8	0.93
U35H40T1	35	40	0.27	0.26	2.19	1.71	1.94	0.03	0.14	2.5	0.06	8.0	9.7	331	1.2	7.3	0.91
U35H50T1	35	50	0.31	0.24	2.19	1.71	1.94	0.03	0.14	2.5	0.06	7.0	10.6	327	1.5	5.7	0.88
U35H60T1	35	60	0.36	0.21	2.19	1.71	1.94	0.03	0.14	2.5	0.06	6.0	11.7	322	2.0	4.3	0.87
U35H70T1	35	70	0.44	0.19	2.19	1.71	1.94	0.03	0.14	2.5	0.06	5.0	13.3	316	2.6	3.1	0.86
U5H00T2	5	0	0.19	0.33	1.10	0.84	0.89	0.06	0.26	4.6	0.22	5.6	13.9	311	2.5	3.6	1.03
U5H10T2	5	10	0.21	0.31	1.10	0.84	0.89	0.06	0.26	4.6	0.22	5.3	14.6	309	2.8	3.1	1.00
U5H20T2	5	20	0.23	0.30	1.10	0.84	0.89	0.06	0.26	4.6	0.22	4.9	15.4	307	3.2	2.7	0.97
U5H30T2	5	30	0.25	0.28	1.10	0.84	0.89	0.06	0.26	4.6	0.22	4.4	16.4	304	3.7	2.3	0.93
U5H40T2	5	40	0.27	0.26	1.10	0.84	0.89	0.06	0.26	4.6	0.22	4.0	17.6	301	4.4	1.9	0.91
U15H00T2	15	0	0.19	0.33	3.70	2.80	2.76	0.03	0.15	5.0	0.25	19.0	15.3	1151	0.8	21.1	1.03
U15H10T2	15	10	0.21	0.31	3.70	2.80	2.76	0.03	0.15	5.0	0.25	17.7	16.0	1144	0.9	18.6	1.00
U15H20T2	15	20	0.23	0.30	3.70	2.80	2.76	0.03	0.15	5.0	0.25	16.4	16.9	1136	1.0	16.1	0.97
U15H30T2	15	30	0.25	0.28	3.70	2.80	2.76	0.03	0.15	5.0	0.25	15.0	18.0	1127	1.2	13.6	0.93
U15H40T2	15	40	0.27	0.26	3.70	2.80	2.76	0.03	0.15	5.0	0.25	13.4	19.4	1116	1.4	11.2	0.91
U15H50T2	15	50	0.31	0.24	3.70	2.80	2.76	0.03	0.15	5.0	0.25	11.9	21.1	1103	1.8	8.9	0.88
U15H60T2	15	60	0.36	0.21	3.70	2.80	2.76	0.03	0.15	5.0	0.25	10.2	23.4	1086	2.3	6.7	0.87
U15H70T2	15	70	0.44	0.19	3.70	2.80	2.76	0.03	0.15	5.0	0.25	8.4	26.7	1065	3.1	4.7	0.86
U25H00T2	25	0	0.19	0.33	6.04	4.75	4.72	0.02	0.11	4.6	0.24	31.0	14.1	1730	0.5	45.9	1.03
U25H10T2	25	10	0.21	0.31	6.04	4.75	4.72	0.02	0.11	4.6	0.24	28.9	14.8	1720	0.5	40.5	1.00
U25H20T2	25	20	0.23	0.30	6.04	4.75	4.72	0.02	0.11	4.6	0.24	26.8	15.6	1708	0.6	35.1	0.97
U25H30T2	25	30	0.25	0.28	6.04	4.75	4.72	0.02	0.11	4.6	0.24	24.4	16.6	1694	0.7	29.7	0.93
U25H40T2	25	40	0.27	0.26	6.04	4.75	4.72	0.02	0.11	4.6	0.24	22.0	17.8	1677	0.8	24.4	0.91
U25H50T2	25	50	0.31	0.24	6.04	4.75	4.72	0.02	0.11	4.6	0.24	19.4	19.4	1657	1.0	19.3	0.88
U25H60T2	25	60	0.36	0.21	6.04	4.75	4.72	0.02	0.11	4.6	0.24	16.6	21.6	1632	1.3	14.6	0.87
U25H70T2	25	70	0.44	0.19	6.04	4.75	4.72	0.02	0.12	4.6	0.24	13.8	24.6	1600	1.8	10.3	0.86
U35H00T2	35	0	0.19	0.33	8.70	6.79	6.80	0.01	0.10	5.1	0.25	44.6	15.4	2729	0.3	76.0	1.03
U35H10T2	35	10	0.21	0.31	8.70	6.79	6.80	0.01	0.10	5.1	0.25	41.7	16.1	2713	0.4	67.0	1.00
U35H20T2	35	20	0.23	0.30	8.70	6.79	6.80	0.01	0.10	5.1	0.25	38.6	17.0	2695	0.4	58.0	0.97
U35H30T2	35	30	0.25	0.28	8.70	6.79	6.80	0.01	0.10	5.1	0.25	35.2	18.1	2673	0.5	49.1	0.93
U35H40T2	35	40	0.27	0.26	8.70	6.79	6.80	0.01	0.10	5.1	0.25	31.7	19.5	2647	0.6	40.4	0.91
U35H50T2	35	50	0.31	0.24	8.70	6.79	6.80	0.01	0.10	5.1	0.25	27.9	21.3	2615	0.8	32.0	0.88
U35H60T2	35	60	0.36	0.21	8.70	6.79	6.80	0.01	0.10	5.1	0.25	24.0	23.6	2575	1.0	24.2	0.87
U35H70T2	35	70	0.44	0.19	8.70	6.79	6.80	0.01	0.10	5.1	0.25	19.8	26.9	2525	1.4	17.0	0.86

Table 2.2. Tested experimental conditions for the co-flow experiment. For all conditions, $U = 5$ m/s, $\phi = 0.7$, $u' = 1.10$ m/s, $v' = 0.84$ m/s, $w' = 0.89$ m/s, $u'/U = 0.22$, $\eta_K = 0.06$ mm, $l_T = 0.26$ mm, and $\Lambda = 4.6$ mm. $S_{L,0}$, δ_L, and $\dot{Q}_{Co-flow}$ are in m/s, mm, and SLPM, respectively.

	H_2%	$\dot{Q}_{Co-flow}$	$S_{L,0}$	δ_L	$u'/S_{L,0}$	Λ/δ_L	Re_T	Da	Ka	Le_{eff}
U5H00T2C100	0	100	0.19	0.33	5.6	13.9	311	2.5	3.6	1.03
U5H00T2C200	0	200	0.19	0.33	5.6	13.9	311	2.5	3.6	1.03
U5H00T2C300	0	300	0.19	0.33	5.6	13.9	311	2.5	3.6	1.03
U5H20T2C100	20	100	0.23	0.30	4.9	15.4	307	3.2	2.7	0.97
U5H20T2C200	20	200	0.23	0.30	4.9	15.4	307	3.2	2.7	0.97

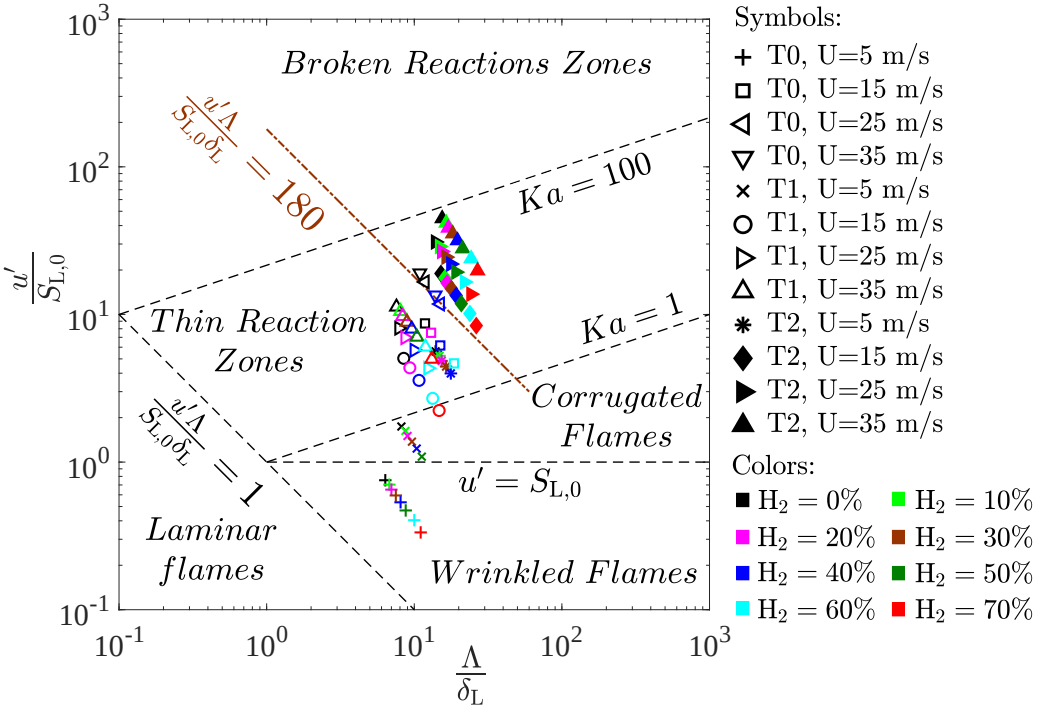

Fig. 2.4. The tested experimental conditions overlaid on the Borghi–Peters diagram [5].

perforated plate as well as condition U15H70T1 pertain to the corrugated flames regime. The rest of the tested conditions are positioned in the thin reaction zones regime. In Fig. 2.4, the newly-suggested border of $u'\Lambda/(S_{L,0}\delta_L) = 180$ [6, 8], which separates the flames with thin and broadened preheat zones, is also presented. This border suggests that the conditions pertaining to $U = 15, 25$, and 35 m/s with 2 perforated plates as well as condition U35H00T0 are expected to feature a broadened preheat zone. Conditions U25H00T0, U25H40T0, and U35H40T0 are positioned near the border of $u'\Lambda/(S_{L,0}\delta_L) = 180$. The rest of the tested conditions are expected to feature a relatively thin preheat zone. The predictions of the Borghi-Peters diagram related to thin and broadened preheat zones are discussed in detail

later in Chapter 4. Tested conditions related to Table 2.2 are not overlaid on the Borghi-Peters diagram as their positions in the diagram are similar to those of U5H00T2 and U5H20T2.

Chapter 3

Data reduction

This chapter is divided into three sections. In the first one, a new model is developed for estimating the heat release rate of the hydrogen-enriched methane-air flames. In the second section, the data reduction procedure for generating processed OH and CH_2O PLIF signals from the raw data is illustrated. Finally, in the last section, a method for calculating the preheat and reaction zone thicknesses as well as the corresponding uncertainties are also discussed.

3.1 A framework for improved prediction of the heat release rate

This subsection aims to develop a model that facilitates improved estimation of the heat release rate (HRR) using PLIF measurements. A brief background related to application of the PLIF technique for prediction of the HRR is provided in Section 1. In this subsection, the model proposed by Chi et al. [7] and Marshall and Pitz [71] is modified to predict the hydrogen-enriched laminar premixed flames HRR.

Equation (1.9) suggest that the time rate of change of the formyl radical (related to heat release rate) is proportional to the multiplication of the formaldehyde and the hydroxyl PLIF signals. In fact, several past investigations utilized Eq. (1.9) to qualitatively study the variation of HRR in methane-air premixed flames, see e.g. [36, 53–55, 128, 129, 157]. Although $CH_2O_{PLIF}OH_{PLIF}$ allows for qualitative study of the turbulent premixed methane-

air flames heat release rate, its adequacy for studying that for hydrogen-enriched methane-air flames remains to be investigated. In the following, a mathematical model that relates CH_2O_{PLIF} and OH_{PLIF} signals with the true heat release rate is proposed. This model is developed for freely propagating pure and hydrogen-enriched methane-air laminar premixed flames. These flames were simulated using the Cantera package [50] with the GRI-Mech 3.0. The simulations were performed for the fuel-air equivalence ratios ranging from 0.5 to 1.0 with steps of 0.1, and hydrogen enrichment percentage ranging from 0% to 90% with steps of 10%. For brevity, the results presented here only pertains to $\phi = 0.5$, 0.7, and 1.0 as well as H_2% of 0%, 30%, 50%, and 70%.

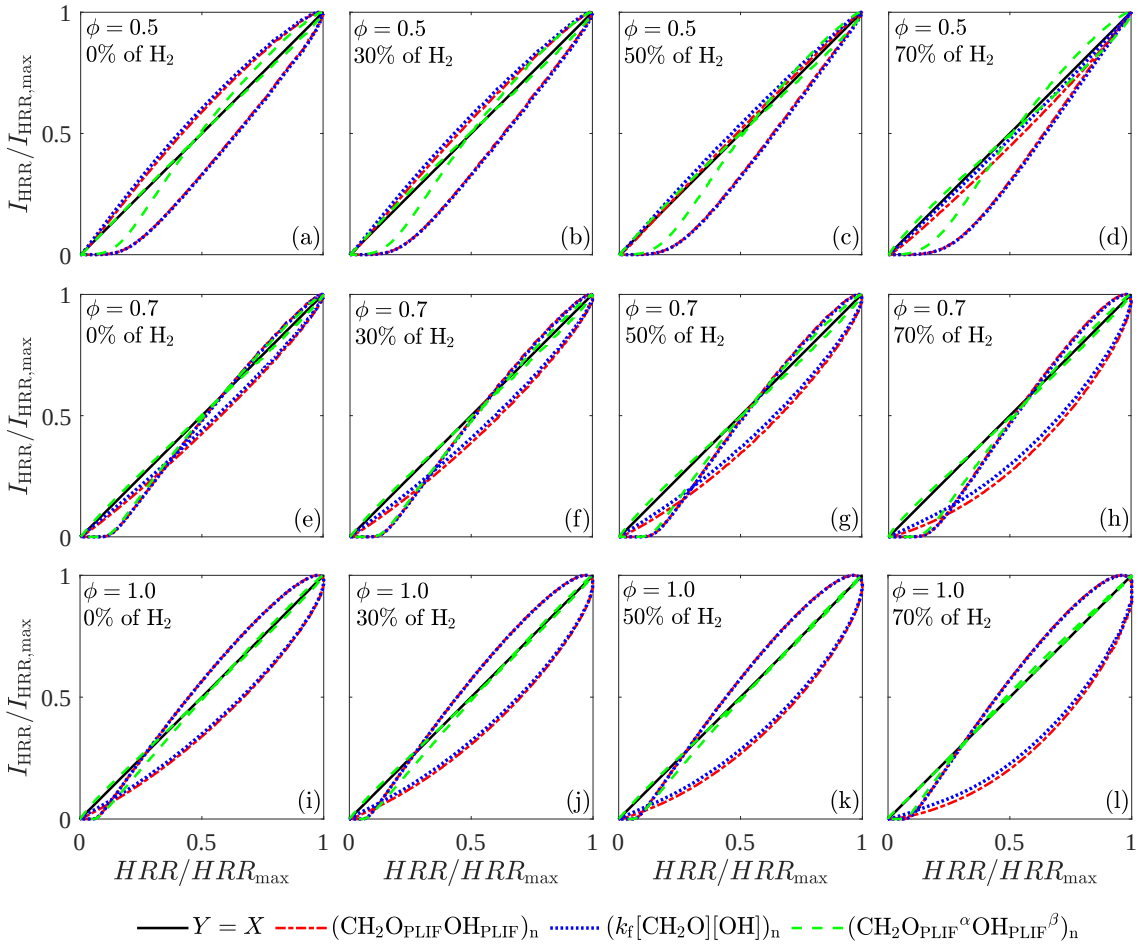

Fig. 3.1. Variations of predicted versus true heat release rates. The results are normalized by the corresponding maximum values. The solid black line, red dotted-dashed curve, blue dotted curve, and green dashed curves pertain to $Y = X$, $CH_2O_{PLIF}OH_{PLIF}$, $k_f(T)[CH_2O][OH]$, and $CH_2O_{PLIF}{}^{\alpha}OH_{PLIF}{}^{\beta}$, respectively.

Variations of the HRR estimated from the right-hand-sides (RHS) of Eqs. (1.9) and (1.6), $CH_2O_{PLIF}OH_{PLIF}$ and $k_f(T)[CH_2O][OH]$, versus the true heat release rate (obtained from the simulations) are shown in Fig. 3.1 by the red dotted-dashed and blue dotted curves, respectively. Please not that, in Fig. 3.1, the results are normalized by their corresponding maximum values. This is highlighted by index "n" in the figure legend. I_{HRR} refers to the heat release rate markers, which are the estimations of the heat release rate from the RHS of Eqs. (1.6) and (1.9). Comparison of these variations shows that the predictions of both Eqs. (1.6) and (1.9) agree, suggesting that $g(T)$ is proportional to $k_f(T)$ not only for pure but also for hydrogen-enriched methane-air premixed flames. The results in Fig. 3.1 show that moving from the reactants to the products, the right hand sides of Eqs. (1.6) and (1.9) increase, reach to their maximum values at the flame front; then, they decrease to about zero at the products forming elliptic shapes. Although the results from the right hand sides of Eqs. (1.6) and (1.9) agree, they do not allow for accurate prediction of the true heat release rate, which is related to the deviation of the elliptic loops from the line of $Y = X$. The results in Fig. 3.1 show that, generally, increasing the fuel-air equivalence ratio as well as the hydrogen-enrichment percentage increase the deviations of the elliptic loops from the line of $Y = X$. These deviations are speculated to be linked to activation of important chemical reactions (other than Eq. (1.5)) that contribute to the heat release rate. Assessing the contribution of other reactions to the heat release rate of pure methane-air flames is experimentally challenging. Also, estimation of $k_f[OH][CH_2O]$, itself, is experimentally challenging due to the potential necessity for estimation of the temperature required for correlating the PLIF signals and the corresponding concentrations of CH_2O and OH, see Eqs. (1.7) and (1.10). To address these complexities, a model/marker that allows for reliable estimation of the heat release rate from the CH_2O and OH PLIF signals is proposed below.

$$I_{HRR} \propto {CH_2O_{PLIF}}^{\alpha} {OH_{PLIF}}^{\beta}. \tag{3.1}$$

Equation (3.1) is developed based on a power-law relation between the PLIF intensities of CH_2O and OH, which is similar to that proposed in Marshal and Pitz [71] as well as Chi et al. [7] for hydrogen-air and pure methane-air premixed flames, respectively. In Eq. (3.1), the combination of α and β was optimized such that the mean distance between the points on the predicted normalized heat release rate (in Fig. 3.1) and the line of $Y = X$ is minimized. The optimized values of α and β for the rest of all tested conditions are provided in Table 3.1. Details of the optimization process is discussed in following.

Table 3.1. Optimized values of α and β used in calculation of I_{HRR}.

			ϕ					
			0.5	0.6	0.7	0.8	0.9	1.0
H_2%	0	α	0.75	0.85	0.92	0.96	0.98	0.99
		β	0.94	0.91	0.86	0.83	0.80	0.79
	10	α	0.75	0.85	0.92	0.95	0.96	0.98
		β	0.93	0.90	0.85	0.81	0.78	0.77
	20	α	0.74	0.85	0.92	0.94	0.95	0.97
		β	0.92	0.89	0.84	0.79	0.76	0.75
	30	α	0.74	0.83	0.92	0.92	0.94	0.97
		β	0.90	0.86	0.82	0.76	0.73	0.73
	40	α	0.75	0.82	0.88	0.92	0.93	0.95
		β	0.89	0.84	0.78	0.73	0.70	0.69
	50	α	0.74	0.80	0.85	0.88	0.89	0.92
		β	0.87	0.80	0.73	0.68	0.64	0.64
	60	α	0.71	0.77	0.82	0.83	0.87	0.88
		β	0.83	0.75	0.67	0.61	0.58	0.57
	70	α	0.67	0.72	0.80	0.78	0.80	0.78
		β	0.77	0.67	0.60	0.52	0.49	0.47
	80	α	0.61	0.67	0.69	0.69	0.69	0.69
		β	0.69	0.58	0.47	0.40	0.36	0.34
	90	α	0.53	0.56	0.56	0.55	0.54	0.54
		β	0.57	0.43	0.28	0.22	0.17	0.15

In the optimization process, the Eq. (1.10) along with the mole fractions of OH and CH_2O were used to estimate the synthetic CH_2O_{PLIF} and OH_{PLIF} in Eq. (3.1). To the best knowledge of the author, information for relating PLIF signals and the mole fractions data is only available for pure methane-air flames in the literature, which is Eq. (1.10). Using this equation for prediction of the synthetic PLIF signals for hydrogen-enriched methane-air flames is speculated to lead to uncertainty. In the optimization procedure, for each

condition, first, large intervals pertaining to variations of these parameters were considered ($\alpha \in [0, 2]$ and $\beta \in [0, 2]$). Then, these intervals were divided into 201 segments each, and several combinations of α and β were selected, leading to $201 \times 201 = 40,401$ combinations. Then, for each combination, the deviation (E) of the estimated I_{HHR} (RHS of Eq. (3.1)) from the true HRR was obtained using

$$E = \frac{\Sigma_{i=1}^{i=N_{\mathrm{t}}} |(\mathrm{CH_2O_{PIF}}(i)^{\alpha} \mathrm{OH_{PIF}}(i)^{\beta})_{\mathrm{n}} - HRR(i)_{\mathrm{n}}|}{N_{\mathrm{t}}}, \tag{3.2}$$

where N_{t} is the total number of data points used in the Cantera simulations to resolve the laminar premixed flame, and i is the summation variable. The values of E were estimated for 40,401 combinations of α and β and for all conditions. The contours of E for the condition with $\phi = 0.7$ and H2 = 0% is shown in Fig. 3.2(a). The results in the figure suggest that there exists a combination of α and β that leads to minimized value of E. This combination of α and β is shown by the cross data symbol in Fig. 3.2(a), and was used for estimation of the heat release rate marker in Eq. (3.1).

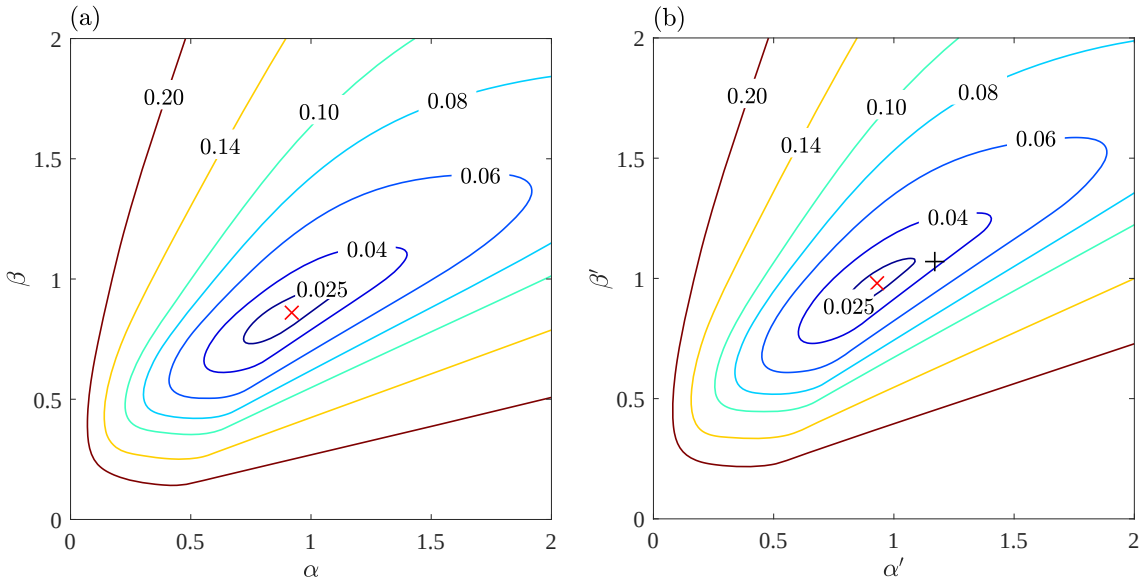

Fig. 3.2. (a) and (b) are contours of E and E', respectively. The cross data symbol is the combinations of (α,β) and (α',β') that minimize E and E', respectively. The plus data symbol is extracted from the study of Chi et al. [7].

Compared to the present investigation, Chi et al. [7] used concentrations of CH_2O and

OH species to estimate the heat release rate marker using

$$I_{HRR} \propto [\mathrm{CH_2O}]^{\alpha'}[\mathrm{OH}]^{\beta'}, \tag{3.3}$$

where α' and β' are optimized in order to accurately predict the heat release rate. Following a procedure similar to that used for α and β, a deviation function (E') can be introduced to estimate the optimized values of α' and β'. This function is given by

$$E' = \frac{\Sigma_{i=1}^{i=N_\mathrm{t}} |([\mathrm{CH_2O}](i)^{\alpha'}[\mathrm{OH}](i)^{\beta'})_\mathrm{n} - HRR(i)_\mathrm{n}|}{N_\mathrm{t}}. \tag{3.4}$$

Contours of E' (for the condition with $\phi = 0.7$ and H2 = 0%) are shown in Fig. 3.2(b). The results in Fig. 3.2(b) suggest that the optimized value of α' and β' are 0.93 and 0.98, respectively. Results of Chi et al. [7] suggest that the optimized values of α' and β' are 1.17 and 1.07, respectively. These values are overlaid on Fig. 3.2(b). Note that α' and β' are denoted by s_2 and s_1 in Chi et al. [7] for $[\mathrm{CH_2O}]$ and [OH] exponents, respectively. The optimized values of these parameters in [7] ($\alpha' = 1.17$ and $\beta' = 1.07$) are shown by the plus data symbol in Fig. 3.2(b), which are respectively different by about 26% and 9% from those obtained here (see the cross data symbol in Fig. 3.2(b)). The reason for this difference is speculated to be linked to the method used in [7] for estimation of the $[\mathrm{CH_2O}]$ and [OH] exponents. Specifically, in Chi et al. [7], the exponents (s_1 and s_2) are estimated such that the prediction of Eq. (3.3) RHS normalized by the corresponding maximum is close to the normalized true heat release rate for several fuel-air equivalence ratios ranging from 0.6 to 1.4. However, in the present dissertation, these exponents are estimated for fixed values of ϕ and hydrogen-enrichment percentage. Nevertheless, the results of Eq. (3.1), compared to those of Eq. (3.3), are more convenient for experimental assessment of the heat release rate. This is because Eq. (3.1) only requires information regarding the $\mathrm{CH_2O}$ and OH PLIF intensities (which are readily available from experiments); however, application of Eq. (3.3)

requires temperature information in addition to these species PLIF intensities for estimation of their concentrations.

The predictions of the model proposed in Eq. (3.1) for the optimized values of α and β are shown by the green dashed curves in Fig. 3.1. As can be seen, the predictions of this model are noticeably more accurate than those obtained based on the RHS of Eqs. (1.6) and (1.9). Thus, the model in Eq. (3.1) along with the optimized values of α and β (provided in Table 3.1) were used for the heat release rate marker estimation discussed in this thesis.

3.2 Reduction of the PLIF data

For each test condition, 500 pairs of OH and CH_2O PLIF images were collected simultaneously. The PLIF data is used to study both the internal structure as well a heat release rate marker of the tested flames. The process related to reducing the raw PLIF images is discussed in this subsection. Figures 3.3(a) and (b) show two representative frames of the raw OH and CH_2O PLIF images, respectively. These frames are related to condition U5H40T1. In order to correct the PLIF images for the effect of the background noise, separate 500 pairs of images were collected for each test condition using the PLIF cameras while the lasers were turned off. The mean background images were subtracted from the corresponding OH and CH_2O PLIF data. Mean background images related to the OH and CH_2O cameras (for condition U5H40T1) are presented in Figs. 3.4(a) and (b), respectively. The background images contain contribution from the flame chemiluminescence, and this contribution is removed from the PLIF images as a result of background subtraction. Then, the obtained PLIF images are normalized by the corresponding laser profiles. The profile of the 283 nm laser sheet is obtained from separate acetone PLIF experiments. For these, a homogeneous mixture of acetone was injected towards the lase sheet. The ICCD camera C_1 (see Fig. 2.1) was equipped with a 305 nm longpass filter. Then, 500 acetone PLIF images were collected, averaged, and used to obtain the two-dimensional OH PLIF laser profile. The 355 nm laser

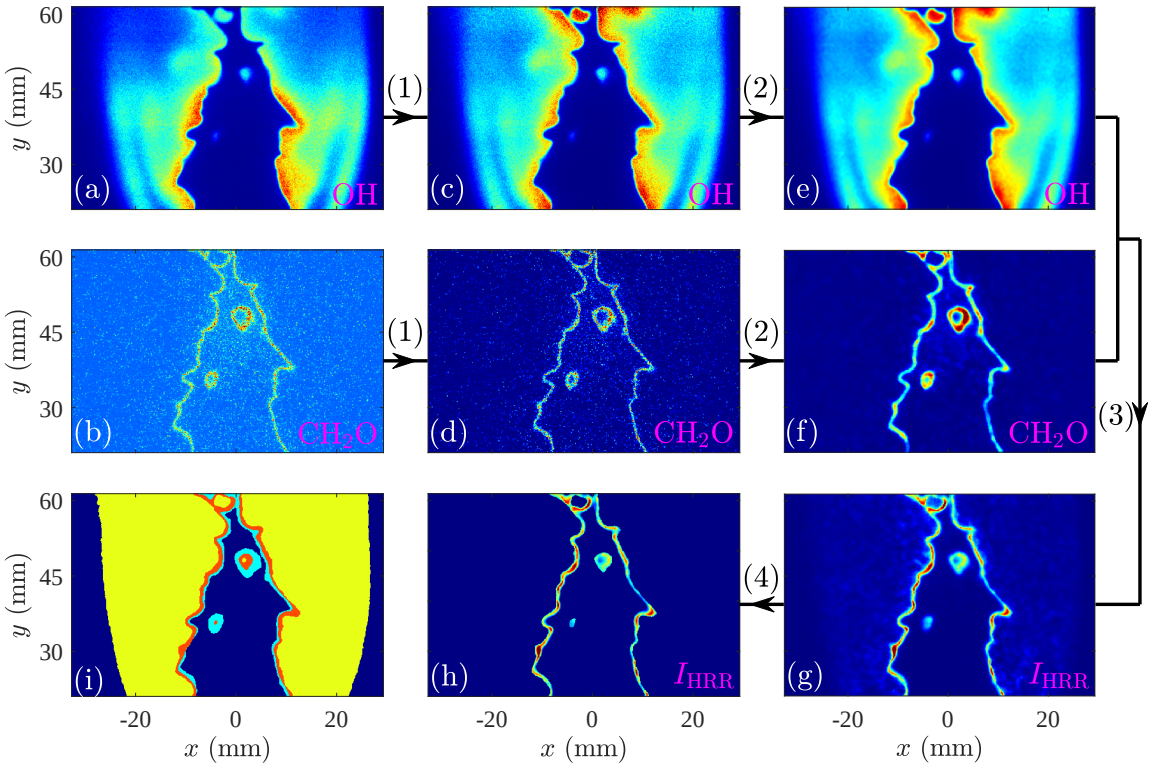

Fig. 3.3. Procedures for reducing OH (a, c, and e) as well as CH_2O (b, d, and f) PLIF images. (g) and (h) are the estimated I_{HRR} before and after the thresholding process, respectively. (i) presents the preheat (cyan), reaction (red), and combustion products (yellow) zones. Process (1) corresponds to the background noise, laser profile, and laser pulse energy corrections. Process (2) pertains to applying the median-based filter. Process (3) corresponds to estimation of the heat release rate from the OH and CH_2O PLIF images. Process (4) pertains to thresholding I_{HRR}. The results pertain to U5H40T1 test condition.

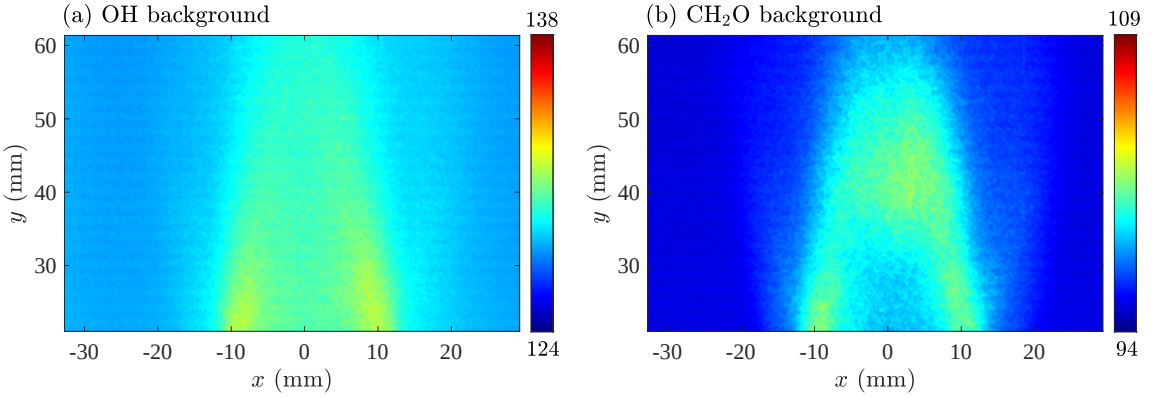

Fig. 3.4. Mean background image pertaining to (a) OH and (b) CH_2O cameras, respectively. The results pertain to Flame U5H40T1 condition.

sheet profile, which was used to normalized the CH_2O PLIF images, was acquired similarly except that the longpass filter was removed from the camera and Rayleigh scattering images were collected (by running air instead of homogeneous mixture of acetone).

As discussed in Chapter 2, two photodiodes were used to capture the laser pulse energy variations of both 283 and 355 nm beams. These were used to normalize both the OH and CH_2O PLIF images (after laser profile correction) in order to remove the effect of the shot-to-shot variation of the lasers pulse energies. Figures 3.3(c) and (d) show the representative frames of OH and CH_2O PLIF images corrected for the effects of background noise, laser profile, and shot-to-shot laser energy variations. These corrections are shown as process (1) in Fig. 3.3. After applying the corrections related to process (1), in order to decrease the remaining background noise, similar to [2, 3, 8, 36, 55, 81, 158], 7×7 and 11×11 pixels^2 median-based filters were applied to the OH and CH_2O PLIF images, respectively. This is shown by process (2) in Fig. 3.3. Similar results are obtained using the Wiener [122] and Gaussian [121, 159] filters. Care was taken to ensure that the utilized filters do not influence the results, with further details provided in the next section. Figures 3.3(e) and (f) present the background subtracted, laser profile and energy corrected, and median-based filtered OH and CH_2O PLIF images, respectively. After process (2), the local, normalized, and relative heat release rate marker (I_{HRR}) was obtained (see process (3) in Fig. 3.3), using the model presented in the previous section (see Eq. (3.1)). This model suggests that the heat release rate is proportional to ${CH_2O_{PLIF}}^{\alpha} \times {OH_{PLIF}}^{\beta}$, with α and β depending on the tested fuel-air equivalence ratio and the hydrogen-enrichment percentage (see Table 3.1). Please note that using the conventional method for calculation of I_{HRR} (i.e. $\alpha = \beta = 1$ [8, 36, 53–55, 67, 128, 129, 157]) leads to similar results and the non unity values of α and β do not influence the conclusions of the thesis. Figure 3.3(g) presents I_{HRR} pertaining to the raw data shown in Figs. 3.3(a and b).

In order to remove the erroneous data during generation of I_{HRR}, the results were thresholded. This is shown by process (4) in Fig. 3.3. It is important to highlight that the OH and CH_2O PLIF images were not thresholded prior to generation of the local heat release rate marker. Instead, the thresholding was performed after generation of this marker, which is

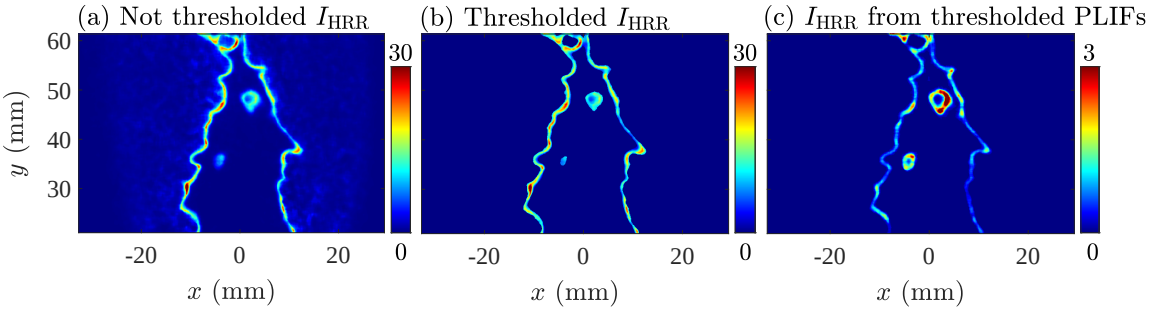

Fig. 3.5. A sample I_{HRR} (a) without thresholding, (b) with thresholding the results in (a), and (c) with thresholding OH and CH_2O PLIF images using 10% of their corresponding global maxima prior to generation of I_{HRR}. The results pertain to test condition U5H40T1.

further discussed here. The local heat release rate marker shown in Fig. 3.3(g) (not thresholded) is presented in Figs. 3.5(a). Also shown in the figure are the thresholded results after generation of I_{HRR}, and this parameter generated using thresholded OH and CH_2O PLIF images. The former and the latter are shown in Figs. 3.5(b) and (c), respectively. The results in Figs. 3.5(b) are thresholded based on 30% of the corresponding global maximum of I_{HRR}, and the results in Figs. 3.5(c) are obtained using OH and CH_2O PLIF images thresholded using 10% of their corresponding global maxima prior to generation of I_{HRR}. As can be seen, thresholding the PLIF images prior to generation of the local heat release rate marker can significantly influence the values of this parameter, which can be seen by comparing the maximum values in Figs. 3.5(a) and (c). As can be seen, thresholding the PLIF signals before generating I_{HRR} can also slightly change the flame structure. However, as comparison of the results in Figs. 3.5(a) and (b) show, the I_{HRR} maximum value and the flame structure are not significantly influenced when this parameter is thresholded after generation of ${CH_2O_{PLIF}}^{\alpha} \times {OH_{PLIF}}^{\beta}$ images.

For all tested conditions, 30% of ${CH_2O_{PLIF}}^{\alpha} \times {OH_{PLIF}}^{\beta}$ global maximum was used for thresholding. This percentage is fixed for all tested conditions. The effect of the threshold value on the local heat release rate marker is presented in Fig. 3.6. The results in Figs. 3.6(a–e) and Figs. 3.6(f–j) pertain to flames with $Ka = 0.1$ (U5H40T0) and 40.4 (U35H40T2), respectively. The first, second, third, fourth, and fifth columns show instan-

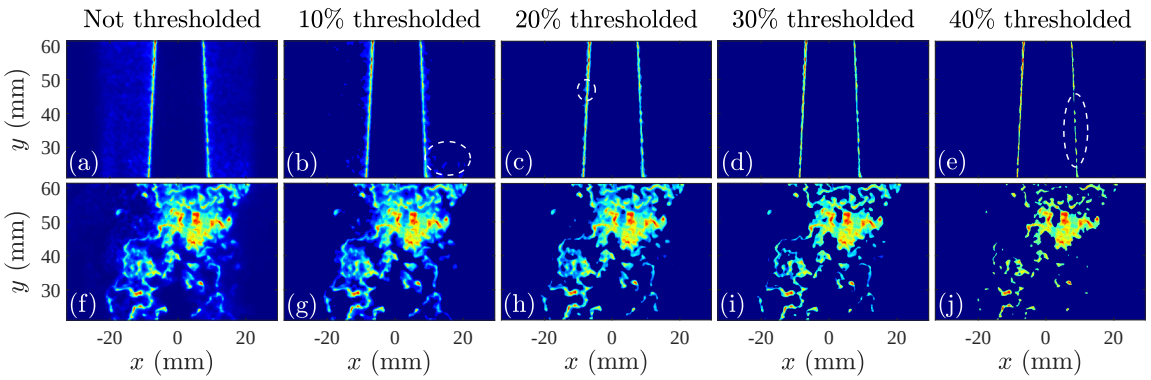

Fig. 3.6. (a–e) and (f–j) present snapshots of the local heat release rate marker for $Ka = 0.1$ (U5H40T0) and $Ka = 40.4$ (U35H40T2), respectively. The results in the first, second, third, fourth, and fifth columns highlight the local heat release rate marker without thresholding, and with 10, 20, 30, and 40% thresholding of the corresponding global maximum, respectively.

taneous images of the local heat release rate marker without thresholding, 10%, 20%, 30%, and 40% thresholding of the corresponding global maximum. Results in Fig. 3.6(a) show that, for nearly laminar conditions, the un-thresholded I_{HRR} may predict non-zero values at very large distances from $x = 0$ and inside the products, which is not realistic. This suggests thresholding I_{HRR} is necessary prior to further analysis. Also, as highlighted by the white dashed ellipses in Figs. 3.6(b and c), 10 and 20% thresholding does not allow for removing all of the erroneous data, and 40% thresholding excessively removes the local heat release rate marker data. As can be seen, 30% threshold is sufficient and necessary for removing noise while keeping the signal for the test conditions of the present thesis. As a result, the 30% threshold was used here. Figure 3.3(h) demonstrate the final thresholded local heat release rate marker.

3.3 A method for estimating preheat and reaction zone thicknesses

The PLIF data was used to estimate the preheat and reaction zones thicknesses. Similar to [8, 53, 54], pixels that feature I_{HRR} values larger than 50% of the global maximum

highlight the reaction zone. The leading edge of the preheat zone is where CH_2O PLIF signal equals 35% of the maximum CH_2O PLIF signal in the reactants side [53, 55]. The trailing edge of the preheat zone is the leading edge of the reaction zone. The preheat and reaction zones for the representative frames presented in Fig. 3.3 are shown by the cyan and red colors in Fig. 3.3(i), respectively. After removing the regions pertaining to the reaction zone, the combustion products are defined as the regions where OH PLIF signal is larger than 15% of the global maximum. Please note that the selected threshold for the combustion product does not influence the conclusion of this study. The combustion products are shown by the yellow color in Fig. 3.3(i).

For highly turbulent premixed flames, due to their relatively complex structure (compared to laminar and moderately turbulent flames), the conventional method of preheat/reaction zone thickness calculation cannot be used. Please note that, in this thesis, highly turbulent premixed flames are tested. Here, the thickness (for both preheat and reaction zones) is defined as the total zone area divided by half of the zone total perimeter. For example, for a disk, the thickness calculated from the above definition is the radius of the disk. For a hollow disk (radii r_1 and r_2, with $r_1 > r_2$), the thickness obtained from the above definition is $(\pi r_1^2 - \pi r_2^2)/(\pi r_1 + \pi r_2)$, which equates to $r_1 - r_2$. For complex structures, such as that shown in Fig. 3.7, the thickness equates to $2\Sigma_{i=1}^{i=4} A_i / \Sigma_{i=1}^{i=6} p_i$. For this structure, $\Sigma_{i=1}^{i=4} A_i$ is the total structure area, which pertains to two islands featuring two holes (A_1 and A_2) as well as two pockets (A_3 and A_4). $\Sigma_{i=1}^{i=6} p_i$ is the total perimeter of the structure shown in Fig. 3.7.

Five parameters may potentially lead to the uncertainty in estimation of the preheat and reaction zone thicknesses. These parameters are filtering the PLIF images (process (2) in Fig. 3.3), three-dimensional orientation of the flames, imaging resolution, optical blur, and laser sheet thickness. Influences of these factors are discussed in the following.

The median-based filtering improves the quality of the PLIF images by removing the

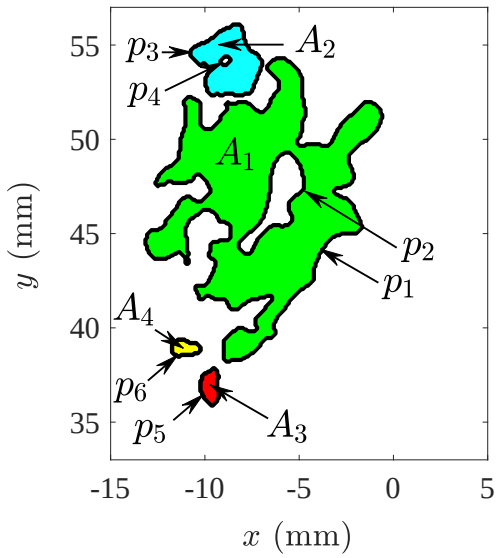

Fig. 3.7. A representative preheat/reaction zone structure. The thickness of this structure is $2\Sigma_{i=1}^{i=4}A_i/\Sigma_{i=1}^{i=6}p_i$. $\Sigma_{i=1}^{i=4}A_i$ and $\Sigma_{i=1}^{i=6}p_i$ are the total structure area and perimeter, respectively.

"salt-and-pepper" noise. Figures 3.8(a) and (b) present two representative OH and CH_2O PLIF images only corrected for the effect of background and laser profile/energy. Figure 3.8(c) is the heat release rate maker estimated from the results in Figs. 3.8(a) and (b) and is not thresholded. The results pertain to flame with $Ka = 76.0$. Similar to the results in Figs. 3.8(a–c), the heat release rate marker was obtained after applying the median-based filters with the corresponding sizes shown in Figs. 3.8(d and e), Figs. 3.8(g and h), and Figs. 3.8(j and k). The corresponding generated heat release rate markers are shown in Figs. 3.8(f, i, and l). As can be seen, changing the median-based filter size does not significantly change the structure of the local heat release rate marker, yet application of this filter allows for removing the "salt-and-pepper" noise.

The results presented in Fig. 3.8 pertain to one snapshot. In order to statistically assess the effect of filtering on the flame thickness, the probability density functions of the normalized preheat and reaction zone thicknesses for the conditions shown in Figs. 3.8(g–l), which pertain to the most turbulent condition (U35H00T2), were evaluated and presented in Figs. 3.9(a) and (b), respectively. In the figure, the solid black and dashed blue curves pertain to OH and CH_2O PLIF images after applying the median-based filters with window

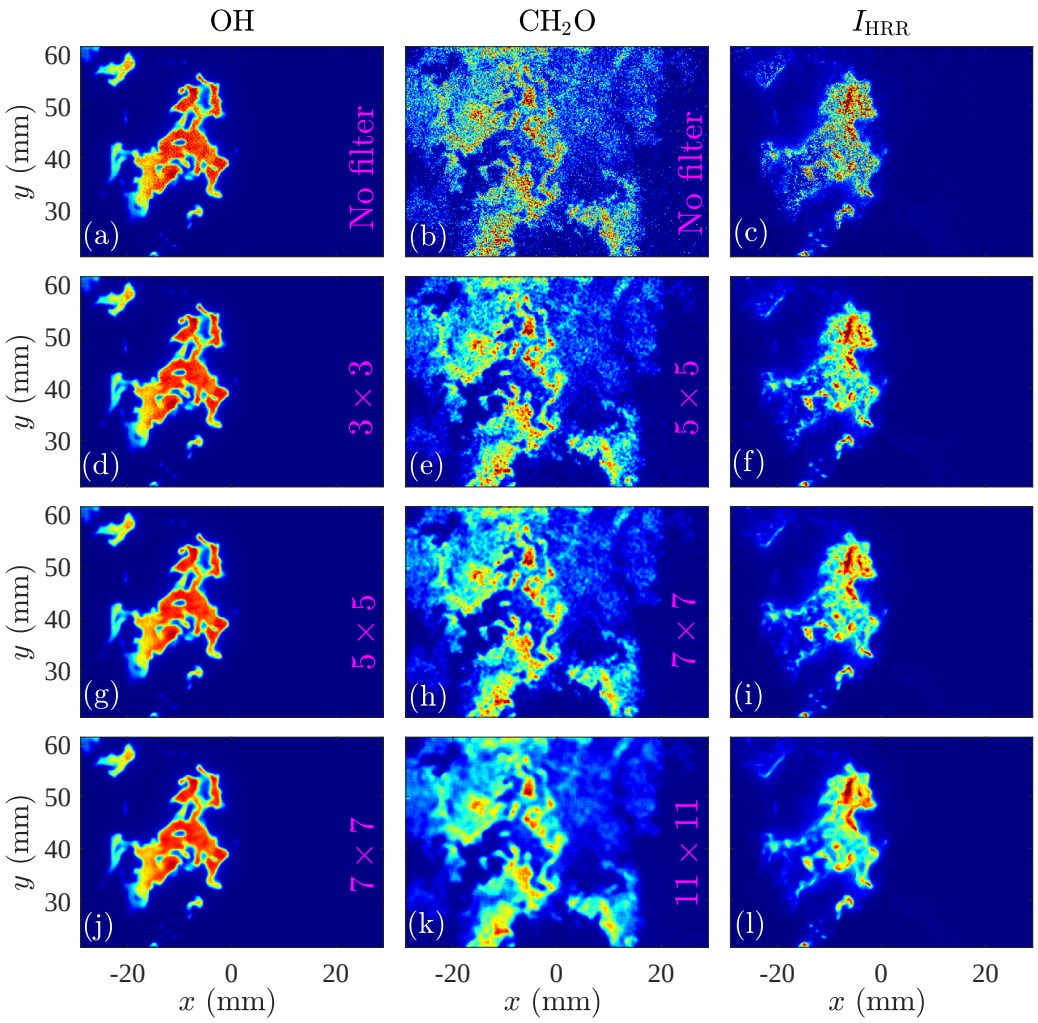

Fig. 3.8. Effect of the median-based filtering on the local heat release rate marker. The results pertain to the flame with $Ka = 76.0$ (U35H00T2). The results in the first, second, and third columns pertain to OH PLIF, CH_2O PLIF, and I_{HRR}, respectively.

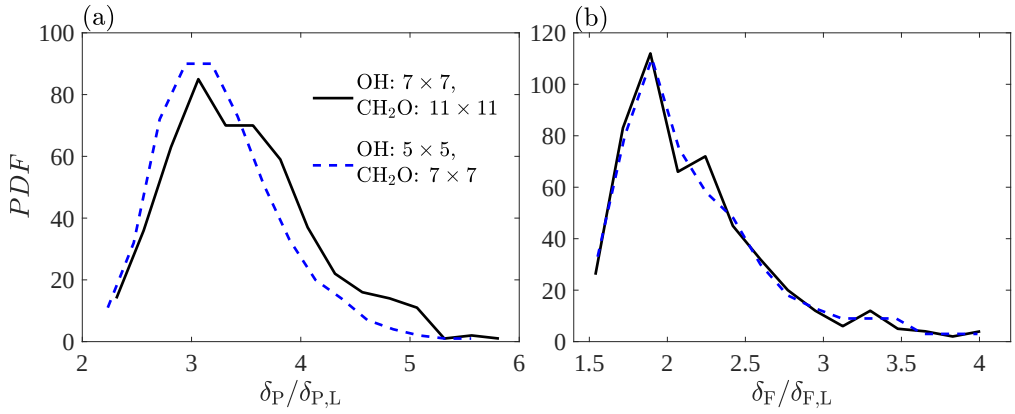

Fig. 3.9. (a) and (b) are the probability density functions of the normalized preheat and reaction zone thicknesses, respectively. The results pertain to the flame with $Ka = 76.0$ (U35H00T2).

sizes of 7×7 and 11×11 as well as 5×5 and 7×7, respectively. As can be seen, changing the filter size does not significantly influence the probability density functions of the preheat and reaction zone thicknesses. Similar results were obtained from the rest of the tested conditions.

Effect of three-dimensional orientation of the flame is studied in past investigations [76, 121, 160–166]. For example, study of Rosell et al. [121] shows that for a flame with $Ka = 60$, the estimated preheat and reaction zone thicknesses can be influenced by three-dimensionality of the flame up to 8% and 11%, respectively. Since this Karlovitz number is close to the maximum tested Ka of the present study (which is $Ka = 76$), the effect of three-dimensionality on the reported results is not expected to be too large. The Full Width at Half Maximum (FWHM) of the line-spread function in the present study is 263 μm, which is the PLIF imaging resolution. The Direct Numerical Simulation results presented in Lapointe and Blanquart [97] suggest that, for turbulent premixed flames with similar Karlovitz numbers, the standard deviation of the flame curvature times the laminar flame thickness is about 0.5 (see Fig. 9(a) in [97]). This corresponds to about 0.66 mm in the present study, which can be properly resolved considering the imaging resolution of 263 μm. Also, the largest curvature reported in Lapointe and Blanquart [97] (which has a very small probability of occurrence) is about 3 times the standard deviation of the flame curvature (see the extent of the horizontal axis in Fig. 8(b) of [97]). This implies that the largest curvature reported in [97] is about 1.5 times the inverse of the laminar flame thickness. Thus, the smallest flame radius calculated and reported in [97] is two-third of the laminar flame thickness. This is nearly 0.22 mm and is about the imaging resolution of the present study. Such corrugations can be detected with the utilized diagnostics, and any potentially thickened reaction zones is not expected to be influenced by the present imaging resolution.

The FWHM of the line-spread function in the present study (263 μm) corresponds to about three pixels, which suggests that the blurring parameter σ_{blur} [66] of the present

study is about 263 μm $\times$ 0.5/89 μm per pixel $\approx$1.5 pixels. The laser sheet thickness (δ_{laser} = 0.25 mm) normalized by the laminar flame thickness (δ_{L} = 0.33 mm) is $\delta_{\text{laser}}/\delta_{\text{l}}$ = 0.76. σ_{blur}, the normalized laser sheet thickness, along with the results in Figs. 14 and 15 of [66] suggest that the effect of laser sheet thickness as well as blurring on our measured preheat and reaction zone thicknesses is less than 8%, which is small. Although, as the turbulence intensity and Karlovitz number increase, flames feature corrugations with larger curvature (smaller radius) [97], the study of Wabel et al. (see Fig. 22 of [66]) suggests that the effect of laser sheet thickness and blurring on the probability density function of curvature is not significant at δ_{laser} and σ_{blur} similar to those of the present study. Note that the Karlovitz number utilized in Wabel et al. [66] (Ka = 65) is close to the largest Karlovitz number tested in here ($Ka = 76$).

Chapter 4

Structure of turbulent premixed flames at large turbulence intensities

In this chapter, the structure of turbulent premixed flames subject to large turbulence intensities is studied. This chapter is divided into three sections. In the first section, the preheat and reaction zone thicknesses are estimated for pure and hydrogen-enriched methane-air turbulent premixed flames. The second and third sections pertain to pure methane-air turbulent premixed flames. In the second section, a framework is developed to study the flamelet/non-flamelet behavior of turbulent premixed flames. In the last section, the correlation between the local turbulent flow characteristics and flame internal structure is presented to study the underlying reasons for the potential broadening of the preheat and reaction zones.

4.1 Preheat and reaction zones thicknesses

Representative planar laser-induced fluorescence images pertaining to the test conditions of U5H00T0 ($Ka = 0.3$), U5H40T0 ($Ka = 0.1$), U35H00T2 ($Ka = 76.0$), and U35H40T2 ($Ka = 40.4$) are presented in the first, second, third, and fourth rows of Fig. 4.1, respectively. The results in the first and second columns are representative hydroxyl and formalde-

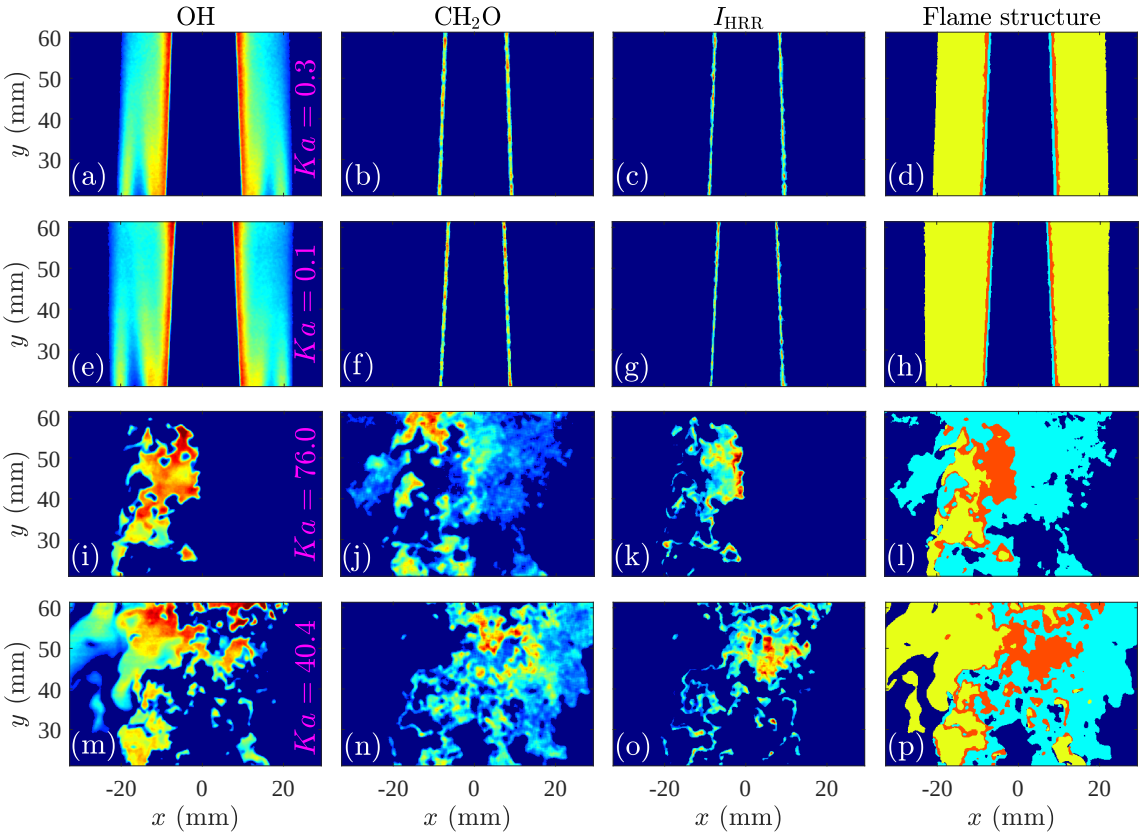

Fig. 4.1. Representative OH (first column) and CH_2O (second column) PLIF images as well as the HRR (third column). The preheat, reaction, and combustion products zones are respectively shown by the cyan, red, and yellow colors in the last column. The first, second, third, and fourth rows pertain to the test conditions of U5H00T0, U5H40T0, U35H00T2, and U35H40T2, respectively.

hyde PLIF data. The third column is I_{HRR} estimated utilizing the procedure discussed in Chapter 3. The corresponding preheat, reaction, and combustion products zones were also obtained using the procedure discussed in Chapter 3, and these zones are shown by the cyan, red, and yellow colors in the last column of Fig. 4.1, respectively. For both pure and hydrogen-enriched methane-air flames with $Ka = 0.3$ (U5H00T0) and 0.1 (U5H40T0), both preheat and reaction zones remain relatively thin, see the cyan and red regions in Figs. 4.1(d and h). However, for the pure and hydrogen-enriched flames, as the Karlovitz number increases to large values, the preheat and reaction zones broaden significantly (see Figs. 4.1(l and p)). This observation is consistent with the results presented in [12, 36, 37, 43–49].

Following the procedure elaborated in Chapter 3, the thicknesses of both preheat and reaction zones were estimated for each frame of the tested conditions. For the conditions

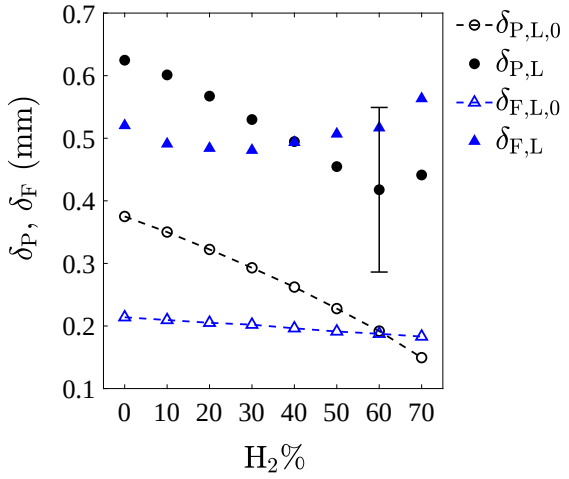

Fig. 4.2. Laminar flame preheat and reaction zone thicknesses versus hydrogen-enrichment percentage. The indices L and L, 0 pertain to values measured experimentally and estimated from the Cantera simulations for laminar flames, respectively.

with the smallest mean bulk flow velocity and no turbulence generator, the flames are nearly laminar. The averaged preheat ($\delta_{P,L}$) and reaction ($\delta_{F,L}$) zone thicknesses for nearly laminar flames versus the tested hydrogen-enrichment percentage are shown in Fig. 4.2. In the figure, the solid black circular ($\delta_{P,L}$) and solid blue triangular ($\delta_{F,L}$) data points highlight the preheat and reaction zone thicknesses measured experimentally in this thesis pertaining to the test conditions of the nearly laminar premixed flames. The open black circular and open blue triangular data points are the preheat ($\delta_{P,L,0}$) and reaction zone ($\delta_{F,L,0}$) thicknesses obtained from Cantera simulations of a freely propagating laminar flame. As can be seen, increasing the hydrogen-enrichment percentage from 0% to 70% decreases $\delta_{P,L,0}$ from about 0.38 to 0.15 mm, however, $\delta_{F,L,0}$ remains nearly constant and about 0.2 mm. The length of the error bar in Fig. 4.2 is the resolution of the PLIF measurements. The results show that, generally, increasing H_2% from 0 to 70% decreases $\delta_{P,L}$. As can also be seen, the variation in the thickness of the reaction zone is within the imaging resolution. Thus, the results presented in Fig. 4.2 suggest that the influences of H_2% on experimentally measured preheat and reaction zone thicknesses for nearly laminar flames follow those predicted by the Cantera simulations. However, the experimentally measured values of $\delta_{P,L}$ and $\delta_{F,L}$ are

about 2.5 times larger than the corresponding values obtained from the Cantera simulations, which are about 0.2–0.4 mm. This observation is consistent with that reported in past studies, see for example [8].

The instantaneous reaction and preheat zone thicknesses were calculated for all frames and test conditions in Table 2.1. The averaged preheat (δ_P) and reaction (δ_F) zone thicknesses for all tested conditions are presented in Figs. 4.3(a) and (b), respectively. The results in Fig. 4.3(a) show that, for a fixed value of u', increasing the hydrogen-enrichment percentage decreases the turbulent flames preheat zone thickness, which is similar to that observed for laminar flames, see Fig. 4.2. The results in Fig. 4.3(b) suggest that, compared to hydrogen-enrichment, the turbulent premixed flame reaction zone thickness is more influenced by u'. In order to normalize the effect of hydrogen addition, u' was divided by the corresponding laminar flame speed, and the results in Figs. 4.3(a) and (b) were presented in Figs. 4.3(c) and (d), respectively. In order to estimate the maximum uncertainty associated with δ_P and δ_F, the test condition of U35H00T2 was repeated three times, the maximum deviation from the mean value was estimated, and the corresponding error bars were overlaid on Figs. 4.3(c) and (d), respectively. The probability density functions of the test conditions with the largest instantaneous preheat and reaction zone thicknesses, which correspond to U35H30T2 and U35H10T2 test conditions, are overlaid by the hot color bar contour on Figs. 4.3(c) and (d), respectively.

The values of the (mean) preheat ($\delta_P/\delta_{P,L}$) and reaction zone ($\delta_F/\delta_{F,L}$) thicknesses normalized by the corresponding experimentally measured laminar flame counterparts are presented in Figs. 4.3(e) and (f), respectively. Overlaid on Fig. 4.3(e) are the normalized preheat zone thickness pertaining to the studies of Skiba et al. [8] and Wang et al. [12], which are shown by the solid red and blue triangular data points, respectively. To aid the discussions, fits to the results of [8] and [12] were obtained and shown by red dotted-dashed and blue dotted curves, respectively. The studies of [8, 12] correspond to pure methane-air

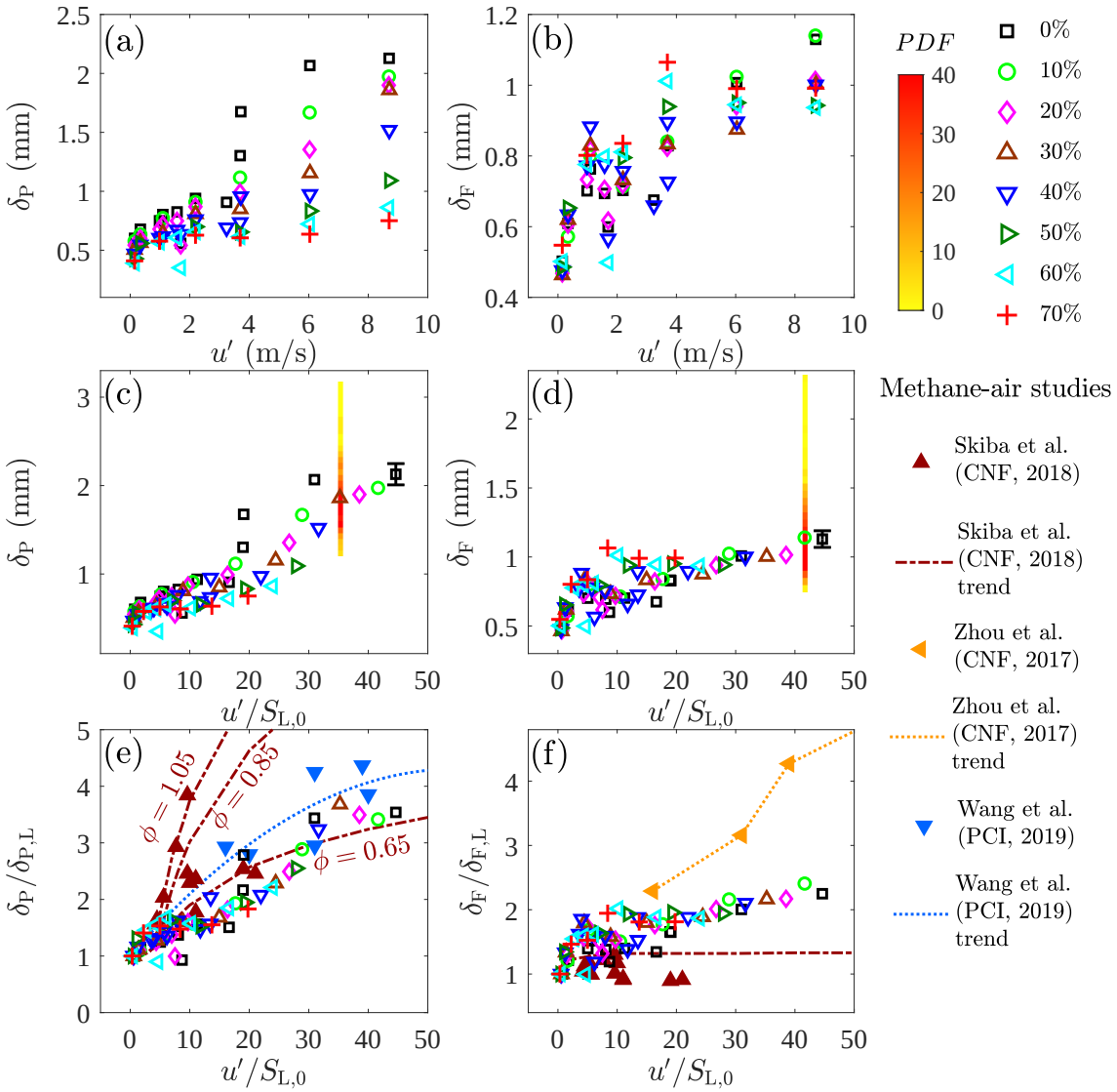

Fig. 4.3. (a and b) are the mean preheat and reaction zone thicknesses presented versus u', highlighting the effect of hydrogen-enrichment. (c and d) are the mean preheat and reaction zone thicknesses presented versus $u'/S_{L,0}$. (e and f) are the results in (c and d) normalized by $\delta_{P,L}$ and $\delta_{F,L}$ (which were presented in Fig. 4.2).

flames. Unlike the present study that the fuel-air equivalence ratio is fixed and equals 0.7, results of [8] pertain to the fuel-air equivalence ratios of 0.65, 0.85, and 1.05, and those of [12] pertain to $\phi = 0.4$, 0.7, and 1.0. Comparison of the results of this thesis with those of Skiba et al. [8] and Wang et al. [12] at a similar fuel-air equivalence ratio (0.65 and 0.7) suggests that the values of $\delta_P/\delta_{P,L}$ nearly collapse. The results show that, for both pure and hydrogen-enriched methane-air flames, the preheat zone features broadening, and this becomes more pronounced with increasing the turbulence intensity. The broadening

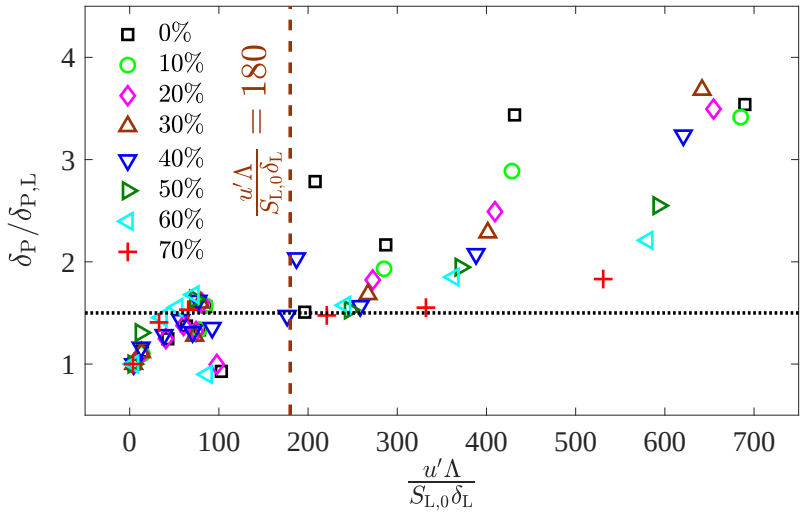

Fig. 4.4. Variation of the normalized mean preheat zone thickness versus $u'\Lambda/(S_{L,0}\delta_L)$ for all tested conditions. The dashed line of $u'\Lambda/(S_{L,0}\delta_L) = 180$ is the border proposed in Skiba et al. [8] and Driscoll et al. [6].

of the preheat zone for hydrogen-enriched methane-air turbulent premixed flames has been recently reported in the study of Zhang et al. [115]. However, the tested conditions in [115] correspond to a maximum turbulence intensity of about 12.5. The results of the present thesis suggest this broadening extends to $u'/S_{L,0} \approx 42$ (for 10% hydrogen-enrichment).

Driscoll et al. [6] and Skiba et al. [8] suggest that the turbulent premixed methane-air flames with $u'\Lambda/(S_{L,0}\delta_L) \gtrsim 180$ may feature preheat zone broadening. Variation of the normalized mean preheat zone thickness versus $u'\Lambda/(S_{L,0}\delta_L)$ is presented in Fig. 4.4 for all tested conditions in Table 2.1. As can be seen, test conditions with $u'\Lambda/(S_{L,0}\delta_L) \gtrsim 180$ feature $\delta_P/\delta_{P,L} \gtrsim 1.5$, however, those with $u'\Lambda/(S_{L,0}\delta_L) \lesssim 180$ feature $\delta_P/\delta_{P,L} \lesssim 1.5$. For pure methane-air turbulent premixed flames, the results presented here agree with those of [6, 8]. The results presented in Fig. 4.4 suggest that the border of $u'\Lambda/(S_{L,0}\delta_L) \approx 180$ can also be used for predicting the preheat zone broadening of hydrogen-enriched methane-air turbulent premixed flames.

The normalized reaction zone thickness data reported in the studies of Skiba et al. [8] and Zhou et al. [36] are presented by the solid red and orange triangular data points, respectively, in Fig. 4.3(f). To aid the discussions, fits to the normalized reaction zone thicknesses of [8]

and [36] were obtained and are shown by the red dotted-dashed and orange dotted curves, respectively. Results of the present thesis show that increasing the turbulence intensity increases the normalized reaction zone thickness as shown in Fig. 4.3(f). This increasing trend is similar for all tested hydrogen-enrichment percentages and agrees well with the increasing trend in the study of Zhou et al. [36]. However, the amount of the reaction zone broadening in our study is smaller than that reported by Zhou et al. [36]. This is speculated to be attributed to the different tested fuel-air equivalence ratios and the geometry of the utilized burners. Compared to the results of the present thesis and those of [36], Skiba et al. [8] suggest that the reaction zone thickness remains nearly constant and does not vary by increasing the turbulence intensity. The reason for the controversial observation reported for the reaction zone thickness is discussed in Chapter 4.3. Nevertheless, the broadening of the reaction zone for hydrogen-enriched methane-air flames shown in Fig. 4.3(b, d, and f) at relatively large turbulence intensities is reported in the present thesis for the first time.

Dinkelacker et al. [167] argued that the three dimensional nature of the flames may lead to uncertainty in estimation of the averaged turbulent premixed flame thickness. They [167] suggested that, instead of the mean, the most probable values obtained from 2D measurements should be used for estimation of the flame thicknesses. Such analysis is also performed in the present thesis for the conditions in Table 2.1. The normalized most probable values as well as the normalized full width at half maximum (FWHM) of the preheat and reaction zone thicknesses are presented in the first and second rows of Fig. 4.5, respectively. In this figure, δ'_{P} and δ'_{F} are the most probable values of the preheat and reaction zone thicknesses, and $FWHM_{\mathrm{P}}$ and $FWHM_{\mathrm{F}}$ are their respective full width at half maximum values. The results are normalized by the most probable values of the preheat ($\delta'_{\mathrm{P,L}}$) and reaction ($\delta'_{\mathrm{F,L}}$) zone thicknesses obtained from the corresponding nearly laminar flames (which pertain to the smallest tested mean bulk flow velocity and with no turbulence generator in Table 2.1). The values of $\delta'_{\mathrm{P,L}}$ and $\delta'_{\mathrm{F,L}}$ are provided in Table 4.1. Results in Fig. 4.5 suggest that

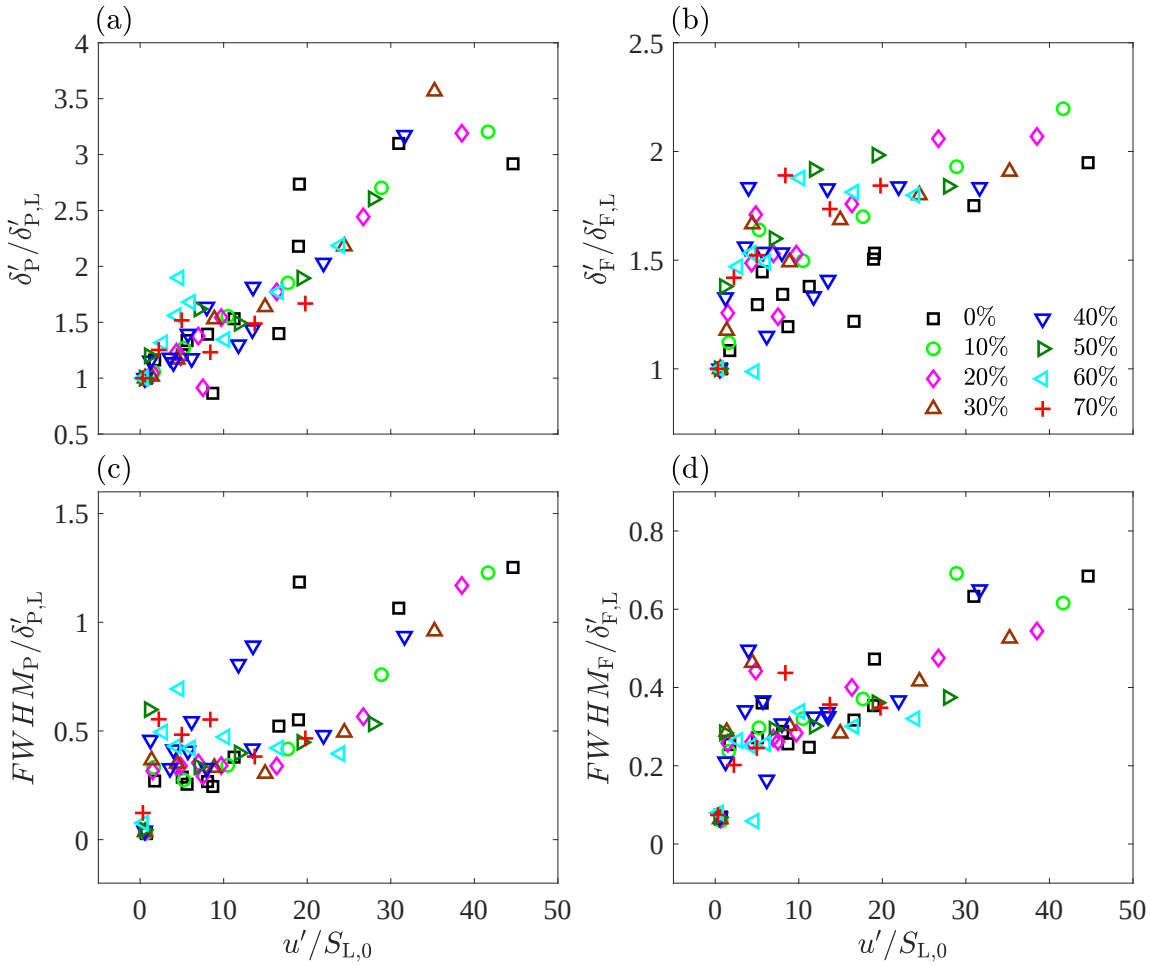

Fig. 4.5. The normalized most probable (a and b) and FWHM (c and d) values of the preheat and reaction zone thicknesses.

increasing the turbulence intensity from 0 to about 50 increases the normalized most probable values of the preheat and reaction zone thicknesses by a factor of about 3.5 and 2.2, which are similar to the results obtained from Fig. 4.3. In essence, the results presented in Fig. 4.3 and Fig. 4.5 show that both the preheat and reaction zones of the pure and hydrogen-enriched methane-air turbulent premixed flames can feature significant amount of broadening. For example, the preheat and reaction zone thicknesses can feature values that are respectively 6.3 and 4.9 times those of the laminar flame counterparts as shown by the probability density functions in Figs. 4.3(a and b). The flame broadening discussed above suggests that the tested flames may not feature the flamelet behavior. This is further discussed in the following section.

Table 4.1. Most probable values of the preheat and reaction zone thicknesses pertaining to the smallest tested mean bulk flow velocity (5 m/s) and with no turbulence generator (the nearly laminar conditions).

	U5H00T0	U5H10T0	U5H20T0	U5H30T0	U5H40T0	U5H50T0	U5H60T0	U5H70T0
$\delta'_{P,L}$ (mm)	0.60	0.57	0.54	0.51	0.47	0.43	0.39	0.40
$\delta'_{F,L}$ (mm)	0.51	0.48	0.46	0.47	0.47	0.48	0.50	0.55

4.2 Flamelet and non-flamelet behavior of premixed flames

In Driscoll et al. [6], it is discussed that the flamelet assumption holds if variations of species mass fractions versus mean progress variable (or temperature) are similar to those of a laminar flame. Similar to this, comparison of the variation of OH versus CH_2O PLIF signals with those of laminar flame is utilized in this thesis to study the flamelet/non-flamelet behavior of the premixed flames. Specifically, variations of the OH versus CH_2O PLIF data normalized by their corresponding maxima are presented in Figs. 4.6(a–d) for four representative frames of conditions U5H00T0, U35H00T0, U35H00T1, and U35H00T2. The flame structure related to the results in Figs. 4.6(a–d) are presented in Figs. 4.6(e–h), respectively. Overlaid on Figs. 4.6(a–d) are the variation of the normalized synthetic OH versus CH_2O PLIF data obtained from the Cantera simulations of a freely propagating laminar premixed pure methane-air flame with $\phi = 0.7$, which is the fuel-air equivalence ratio tested for all conditions. In Figs. 4.6(a–d), data with OH and CH_2O PLIF signals smaller than 10% of the corresponding maxima are shown by the blue color. OH and CH_2O PLIF signals are available inside the entire presented field of view. The blue data points in Fig. 4.6 include preheat zone (regions with a large CH_2O and very small OH PLIF signals), products (regions with a large OH and very small CH_2O PLIF signals), as well as regions significantly far from the flame (either towards the products or inside the cold reactants). The last group of points are located close to the origin of the OH versus CH_2O scatter plots.

Following the above discussions, data with considerable deviation from that of the freely propagating laminar flame towards $OH/OH_{max} = CH_2O/CH_2O_{max} = 1$ features non-flamelet behavior. Such data is shown by the red color in Fig. 4.6. Specifically, for a given

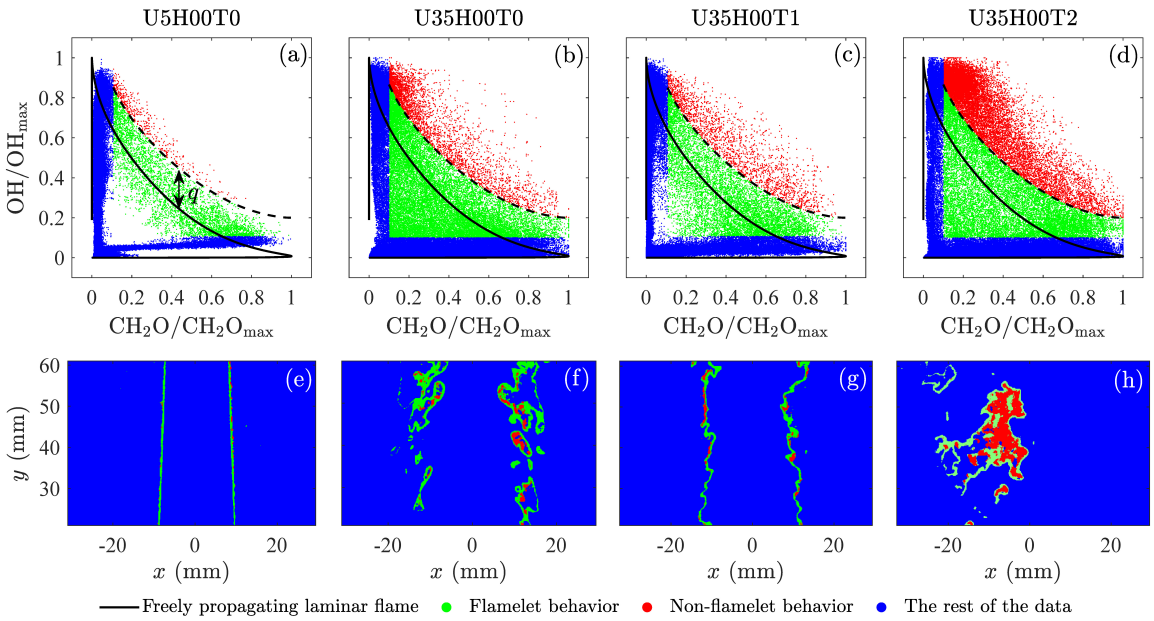

Fig. 4.6. (a–d) Variations of OH versus CH_2O PLIF data for four representative frames of conditions U5H00T0, U35H00T0, U35H00T1, and U35H00T2. (e–h) Regions of the flames in the first row featuring the flamelet (green color) and non-flamelet (red color) behaviors.

CH_2O/CH_2O_{max}, the red color highlights the data points for which the corresponding OH PLIF data is larger than that of a freely propagating laminar flame by q, see Fig. 4.6(a). For the results presented here, $q = 0.2$. The border highlighted by $q = 0.2$ is shown by the black dashed curves in Fig. 4.6(a–d). The data limited between the red and blue colored data points are highlighted by the green color and pertains to the flamelet behavior. Please note that only data with considerable deviations towards $OH/OH_{max} = CH_2O/CH_2O_{max} = 1$ was considered as the non-flamelet behavior. The reason for this is discussed in detail in Appendix D. The pixels that correspond to the red and green colors in Figs. 4.6(a–d) are highlighted by the corresponding red and green color pixels shown in Figs. 4.6(e–h). As can be seen in Fig. 4.6(h), for the largest tested Karlovitz number, the red data points (related to the non-flamelet behavior) highlight majority of the thickened reaction zone. This means that the non-flamelet behavior is related to the broadened reaction zones and both (broadening of the reaction zone as well as deviation of OH versus CH_2O PLIF signals from that of the laminar flame towards $OH/OH_{max} = CH_2O/CH_2O_{max} = 1$) are consistent.

Please note that changing the threshold used for highlighting the blue data points (related to reactants, preheat zone, and products), which was set to 10%, as well as q (which was set to 20%) change the number of data points highlighted by the blue, red, and green colors in Fig. 4.6, but it does not change the above conclusions. As discussed in Appendix D, the value of $q = 0.2$ was selected based on the Cantera simulations of premixed stretched laminar flames, ensuring that the deviation of the PLIF data from the freely propagating laminar flame data is not due to the flame stretch.

In order to quantify the non-flamelet behavior, the total number of the red data points (N_{NF}) in Figs. 4.6(a–d) divided by the sum of the red and green data points ($N_{\mathrm{FL}} + N_{\mathrm{NF}}$) was used. This ratio is referred to as $\mathcal{N}\%$ and is given by

$$\mathcal{N}\% = \frac{100 N_{\mathrm{NF}}}{N_{\mathrm{NF}} + N_{\mathrm{FL}}}. \tag{4.1}$$

$\mathcal{N}\%$ was calculated for each frame and for all pure methane-air conditions presented in Table 2.1. Variations of $\mathcal{N}\%$ versus the preheat and reaction zone thicknesses (for all frames and tested methane-air conditions) are presented in Figs. 4.7(a) and (b), respectively. Please note that $\mathcal{N}\%$, δ_{P}, and δ_{F} are calculated for all of the frames and for all of the 12 pure methane-air experimental conditions in Table 2.1. Since 500 frames are recorded for each reacting condition, 12 conditions of pure methane $-$ air flames $\times$ 500 frames/condition $\times$ 1 data point/frame = 6000 data points are overlaid on Fig. 4.7. The results in Figs. 4.7 are color-coded, highlighting the effect of the utilized turbulence generator. Specifically, the blue, green, and red colors pertain to the turbulence generating mechanism with zero, one, and two turbulence generator(s), respectively. This is highlighted by # TG(s) in the figure. Also, overlaid on the figure are the trends of variations shown by the dotted-dashed lines. In order to obtain the trends, the range of variations related to δ_{P} and δ_{F} were divided into 9 bins, and the corresponding $\mathcal{N}\%$ data were averaged and shown by the cross data symbol

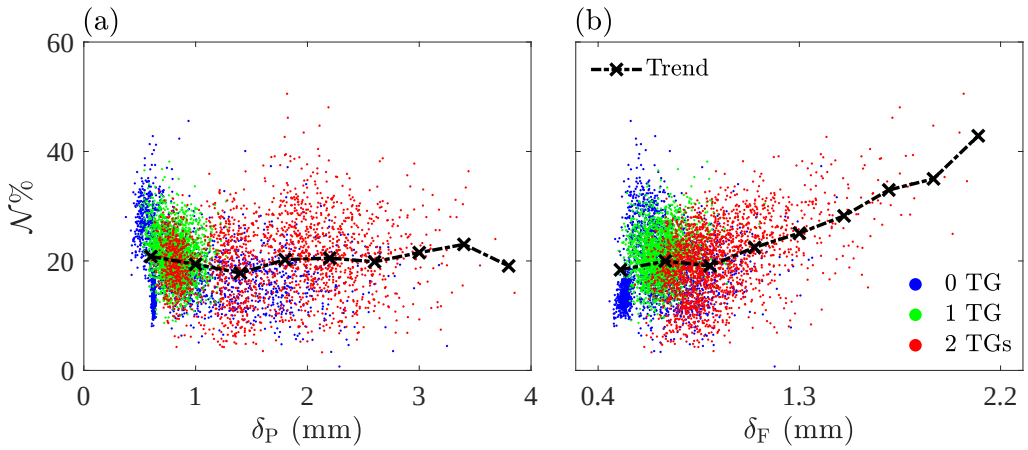

Fig. 4.7. Variation of the instantaneous non-flamelet behavior ($\mathcal{N}\%$) with (a) preheat and (b) reaction zone thicknesses for pure methane-air flames. # TG is the number of utilized turbulence generators.

for each bin. The results in Fig. 4.7(b) show that $\mathcal{N}\%$ is positively related to the reaction zone thickness. However, $\mathcal{N}\%$ is not sensitive to variation of the preheat zone thickness. This is because this parameter is estimated using the red and green data points shown in Fig. 4.6, which primarily pertain to the reaction zone but not the preheat zone.

The averaged values of $\mathcal{N}\%$ for all tested methane-air conditions in Table 2.1 are presented in Fig. 4.8. A sensitivity analysis was performed to investigate effect of q (discussed earlier) on the results shown in Fig. 4.8, and the details are provided in Appendix D. Overlaid on Fig. 4.8 are the error bars. Specifically, for each condition, the length of the error bar is equal to the standard deviation of the data corresponding to the tested condition. As can be seen, generally, the mean value of $\mathcal{N}\%$ increases with increasing $u'/S_{L,0}$. However, there are some exceptions. For example, the blue data point pertaining to $u'/S_{L,0} = 8.8$ (which is related to condition U15H00T0) features relatively large mean value of $\mathcal{N}\%$. This data point is not an outlier. The reason for this deviation is because the interacting turbulent flow is primarily dominated by the Kelvin-Helmholtz instability in the shear layer of the Bunsen flame for U15H00T0 condition. Details of how this instability influences the non-flamelet behavior are discussed in Appendix E. The reason for flamelet/non-flamelet

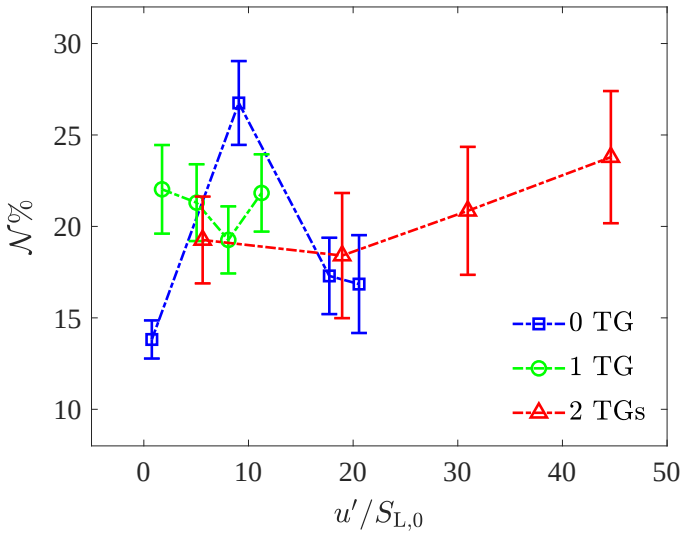

Fig. 4.8. Variation of the average non-flamelet behavior ($\mathcal{N}\%$) versus turbulence intensity ($u'/S_{L,0}$) for pure methane-air flames.

behavior and/or the thickening of the preheat and reaction zones can be best investigated using the local turbulent flow structure, which is discussed in the following section.

4.3 Correlation between the local turbulent flow characteristics and the flame internal structure

In order to investigate the underlying reason for thickening of the preheat and reaction zones, the component of the vorticity vector normal to the measurement plane ($\omega = \partial u/\partial x - \partial v/\partial y$ with u and v being the velocity vectors along y and x directions, respectively) was estimated first. Contours of ω pertaining to four representative frames (the same frames presented in Fig. 4.6) pertaining to U5H00T0, U35H00T0, U35H00T1, and U35H00T2 conditions are presented in the first row of Fig. 4.9. Note that the white regions in the figure are those in which ω was not calculated due to either lack of seed particles and/or inaccurate velocity gradients. In the figure, negative values (blue) pertain to clockwise-rotating eddies, and positive values (red) pertain to counter clockwise-rotating eddies. Also overlaid on Figs. 4.9(a), (b), (c), and (d) are the black contours, which high-

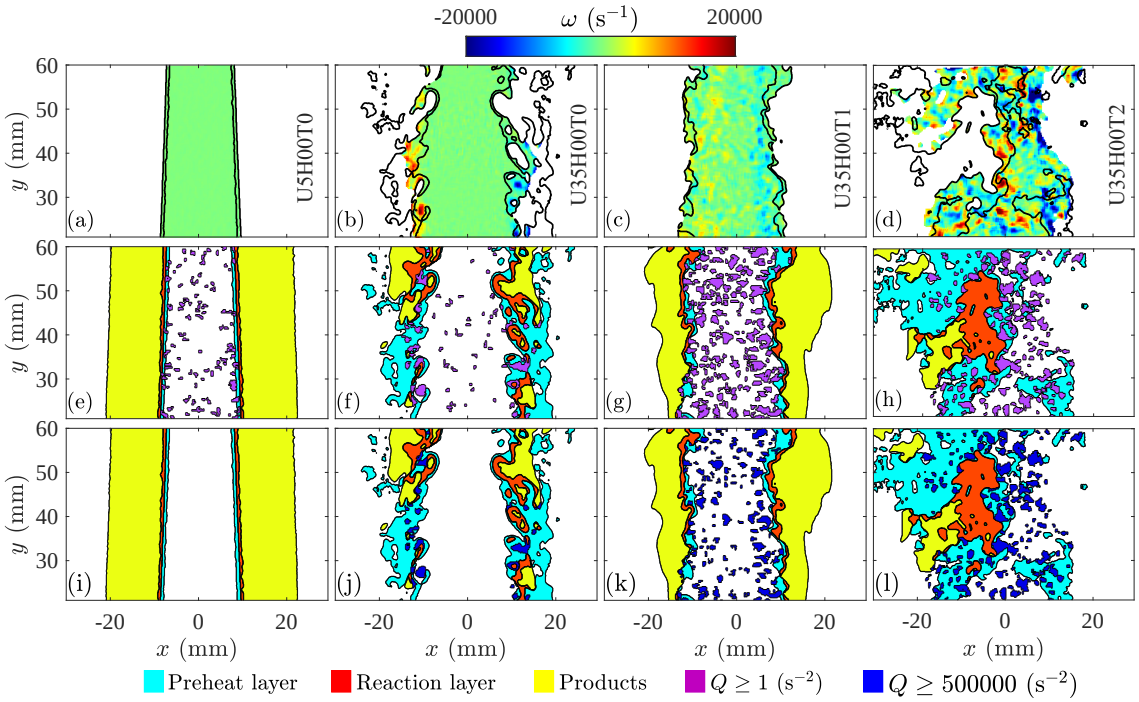

Fig. 4.9. (a–d) are preheat zone borders along with the vorticity. (e–h) and (i–l) show overlay of the flow structures using $Q \geq 1$ and $Q \geq 500000$, respectively, on the flame structure. In (e-l), the regions colored by cyan, red, and yellow pertain to the preheat, reaction, and combustion products zones, respectively. The first, second, third, and fourth columns pertain to U5H00T0, U35H00T0, U35H00T1, and U35H00T2 conditions, respectively.

light the borders of the preheat zone. Comparison of the preheat zone borders and the contours of ω shows that the eddies with relatively large value of vorticity may exist inside the reactants and preheat zones for U35H00T2 condition, see Fig. 4.9(d). Since vorticity can feature contribution from the strain rate, in addition to the vorticity, the Q–criterion was also utilized to study the interaction of the turbulent flow structures with the flames. The eddies were identified and characterized in the present investigation using the swirling strength (Q), which is given by [168, 169]:

$$Q = -\frac{1}{2}\left[\left(\frac{\partial u}{\partial y}\right)^2 + 2\frac{\partial u}{\partial x}\frac{\partial v}{\partial y} + \left(\frac{\partial v}{\partial x}\right)^2\right]. \tag{4.2}$$

The Q–criterion allows to highlight regions where the rotation rate is considerably larger than the strain rate [168–171]. The second and third rows of Fig. 4.9, highlight regions

with $Q \geq 1$ s^{-2} and $Q \geq 500000$ s^{-2} using the purple and blue colors, respectively, for the corresponding frames shown in the first row of the figure. In this figure, the preheat and reaction zones are shown by the cyan and red colors, respectively; and, data with yellow color pertains to the combustion products. Comparison of the second and third rows of Fig. 4.9 suggests that the size of the eddies are not significantly sensitive to the selected value of Q in the present study. However, as Fig. 4.9 shows, weaker vortices can be also detected using a smaller value of Q. Results in Figs. 4.9(h) and (l) show that the size of the eddies are considerably smaller than or on the order of the preheat and reaction zones. This means that such eddies have penetrated into and exist inside the preheat zone.

In order to investigate the relation between the preheat and reaction zone thicknesses and the local turbulent flow characteristics, mean of the swirling strength of the vortices (where $Q > 0$) located in the reactants (Q_{R}) and preheat zone (Q_{P}) were estimated and presented in Fig. 4.10 for pure methane-air conditions (without hydrogen-enrichment) in Table 2.1. The results are normalized by the corresponding value of the swirling strength estimated in the reactants for the nearly laminar condition pertaining to pure methane-air flame ($Q_{\mathrm{R,L}} = 2157$ s^{-2}, which corresponds to U5H00T0 condition). In the figure legend, 0 TG, 1 TG, and 2 TGs refer the first, second and third turbulence generating mechanism, respectively. The maximum error of the swirling strength pertains to Q_{P} of U35H00T0 condition and is shown by the error bar in Fig. 4.10. The error is estimated using the maximum deviation of the data obtained for three sets of experiments (accounting for repeatability) related to the same condition, with each set containing 500 frames. The results in Fig. 4.10 show that increasing the turbulence intensity ($u'/S_{\mathrm{L},0}$) increases both Q_{R} and Q_{P} considerably. Specifically, for the third turbulence generating mechanism, increasing $u'/S_{\mathrm{L},0}$ to about 45 increases both Q_{R} and Q_{P} to values that are about 8000 times $Q_{\mathrm{R,L}}$. Similar behavior is observed for the absolute value of the vorticity. However, since the vorticity is influenced by the effect of shear (strain rate) as well, swirling strength is more

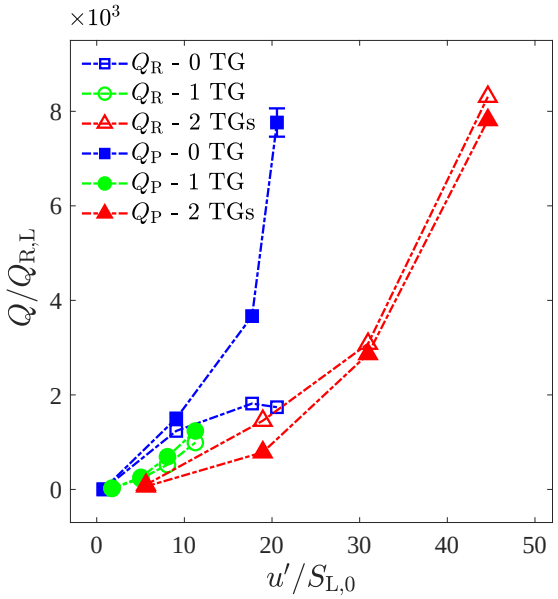

Fig. 4.10. Variation of the mean value of swirling strength inside the reactants (Q_R) and preheat zone (Q_P) for pure methane-air flames in Table 2.1.

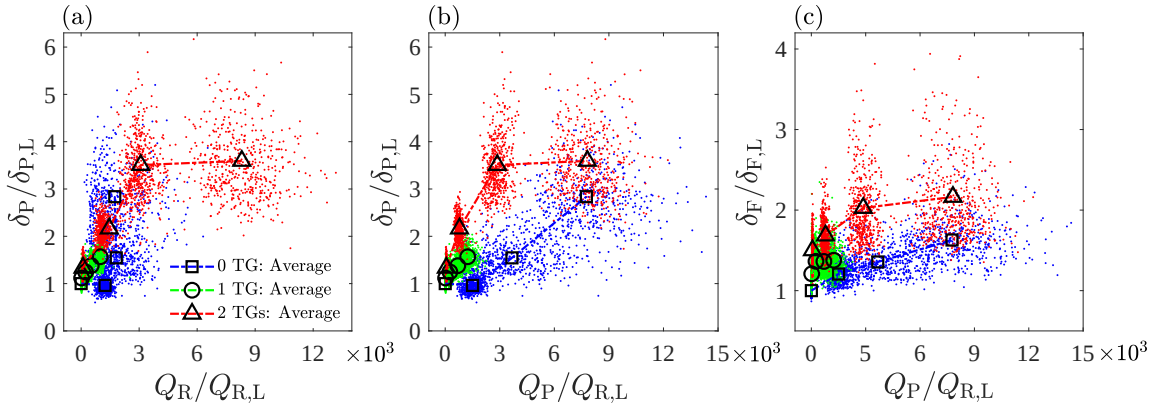

Fig. 4.11. Variation of the mean and instantaneous normalized preheat zone thickness versus the normalized swirling strength calculated inside the reactants (a) and preheat zone (b). Variation of the mean and instantaneous normalized reaction zone thickness versus the normalized swirling strength inside the preheat zone (c).

accurate for characterizing the turbulent eddies. For the rest of the analyses, only the results pertaining to Q is considered. The increase of vorticity and swirling strength (by increasing the turbulence intensity) in the reactants and preheat zone is consistent with results of past investigations, see for example, effect of turbulence intensity on vorticity fields presented in DNS of Lapointe et al. [172].

Comparison of the results in Figs. 4.3 and 4.10 suggests that there may exist a positive correlation between the mean value of the swirling strength (calculated in both reactants

and preheat zone) and the preheat and reaction zone thicknesses. In order to investigate this, the normalized values of δ_P versus the normalized values of Q_R and Q_P were obtained for each frame of the methane-air flames, and the results are presented by the scatter plots in Figs. 4.11(a and b), respectively. Similarly, the normalized values of δ_F versus normalized Q_P were calculated and presented in Fig. 4.11(c). The results in Fig. 4.11 are color-coded based on the utilized turbulence generating mechanism (the blue, green, and red data points correspond to the first, second, and the third turbulence generation mechanism). Also overlaid on Fig. 4.11 are the averaged values of the scatter plots, which are shown by large black square, circular, and triangular data symbols. The results presented in Fig 4.11 suggest that δ_P and δ_F are positively correlated with Q_R and Q_P. Please note that, since the seed particles evaporate at the reaction zone, velocity (and as a result the swirling strength data) is not available in the reaction zone. Thus, variation of δ_F with swirling strength in the reaction zone cannot be presented. Also, since the preheat zone is positioned between the reactants and the reaction zone, the variations of the normalized reaction zone thickness versus the swirling strength estimated in the reactants are not of interest and are not presented. In Fig 4.11(a), the data related to the first turbulence generating mechanism (0 TG) features a relatively larger slope compared to the data pertaining to the second and third turbulence generating mechanisms. This is because, for the first turbulence generating mechanism (no perforated plate) and at large mean bulk flow velocities (more than 5 m/s), see Fig. 4.9, the flame structure is mostly influenced by the turbulence generated in the jet shear layers [94]. Specifically, for such conditions, the shear layers roll-up (due to the Kelvin-Helmholtz instability) and the generated eddies reside in the preheat zone as can be seen in the second column of Fig. 4.9. These eddies feature relatively strong swirling strength compared to those inside the reactants. As a result, Q_P related to the first turbulence generating mechanism can increase up to about 10000 times $Q_{R,L}$ while Q_R only increases to about 3000 times $Q_{R,L}$ (see the extent of the blue data in Fig. 4.11(a and b)). Nevertheless,

the positive correlations between the preheat and reaction zones thicknesses and the swirling strength suggest that the broadening of both preheat and reaction zones may be potentially due to the penetration of the eddies into these zones. This is investigated in more detail in the following.

Using different turbulence generating mechanisms leads to different turbulent flow characteristics (see Figs. 4.9, 4.10, and 4.11). Considering that the preheat and reaction zone thicknesses are impacted by the characteristics of the interacting eddies, it can be inferred that the turbulence generating mechanisms significantly influence the flame structure. In fact, this is speculated to be the reason for the different trends reported in this thesis, Zhou et al. [36], and Skiba et al. [8] for the variation of the reaction zone thickness with $u'/S_{\mathrm{L},0}$. For example, in the study of Skiba et al. [8], turbulence is generated using a slotted plate along with impinging jets. However, in the present thesis, combination of perforated plates are utilized. This difference may cause different turbulence spectra, different eddy size distributions, and as a result, altered reaction zones thickness.

In order to highlight the effect of the turbulence generating mechanism on the preheat/reaction zones, the eddy size distribution as well as the eddy specific kinetic energy were estimated here. The equivalent radius of an eddy ($\mathcal{R}$) was estimated using

$$\mathcal{R} = 2\frac{\mathcal{A}}{\mathcal{C}}, \tag{4.3}$$

where $\mathcal{A}$ and $\mathcal{C}$ are the area and circumference of eddies with $Q > 0$ s^{-2}, similar to those shown in Fig. 4.9(e–h). The lower bound of the Q–criterion is selected to be zero allowing to visualize all eddies. Please note that, for a perfectly circular eddy structure, $\mathcal{R}$ equates to the radius of the circle. For conditions U5H00T0, U35H00T0, U35H00T1, and U35H00T2, $\mathcal{R}$ was calculated for all of the eddies in all of the frames and the probability density function (PDF) of $\mathcal{R}$ is shown in Fig. 4.12. As discussed in Appendix F, the smallest eddy diameter

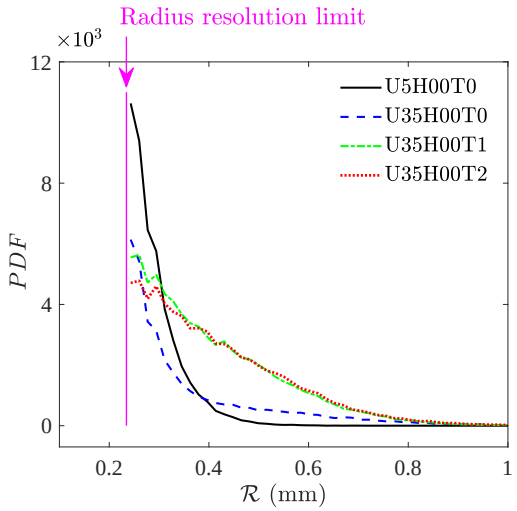

Fig. 4.12. Probability density functions of eddy size ($\mathcal{R}$) distribution for conditions U5H00T0, U35H00T0, U35H00T1, and U35H00T2.

that can be resolved in the present thesis equals the interrogation window size, i.e. 0.47 mm. Thus, the smallest detectable eddy radius is 0.23 mm. For this reason, eddies with radius smaller than 0.23 mm (diameter smaller than the interrogation window size) are removed from the analyses. The results in Fig. 4.12 show that the distribution of $\mathcal{R}$ is similar for conditions U5H00T0 and U35H00T0, for which both mesh screens in the settling chamber and Kelvin-Helmholtz instability are responsible for generation of turbulence. Also, the distribution of $\mathcal{R}$ is similar for conditions U35H00T1 and U35H00T2 for which turbulence is generated using the perforated plate(s). However, comparison of results related to conditions U5H00T0 and U35H00T0 with those related to conditions U35H00T1 and U35H00T2 suggests that the distribution of $\mathcal{R}$ is different for these two different types of turbulence generating mechanisms, which confirms that different types of turbulence generating mechanisms lead to different distribution of eddy sizes. For example, conditions U35H00T1 and U35H00T2 feature considerable number of eddies with the radius of about 0.4–0.6 mm compared to conditions U5H00T0 and U35H00T0. Similar conclusions were made for the rest of the tested pure methane-air conditions.

Although knowledge related to the probability density functions of the eddy sizes is important for elaborating the effect of turbulence generating mechanism on the preheat

and reaction zone thicknesses, a detailed understanding can be obtained using the specific kinetic energy of the eddies. The rotational kinetic energy (KE_ω) and total kinetic energy (KE), both normalized by mass, of a single eddy are given by the following equations.

$$KE_\omega = \frac{1}{2}\sum_{i}^{n_e}(r_i\zeta_i)^2, \tag{4.4a}$$

$$KE = \frac{1}{2}\sum_{i}^{n_e}\left(u_i^2 + v_i^2 + w_i^2\right), \tag{4.4b}$$

where index i indicates the i^{th} resolved data point inside a single eddy, and n_e is the total number of the data points resolved inside the same eddy. ζ_i is the rotational speed corresponding to the i^{th} data point; and, by definition, the rotation vector is half of the vorticity vector [72]. As a result, $\zeta_i = \omega_i/2$, where ω_i is the vorticity calculated corresponding to the i^{th} data point. r_i refers to the spatial distance between the i^{th} data point and the eddy's center of area. In Eq. (4.4b), u_i, v_i, and w_i are the velocity components of the i^{th} resolved data (inside the eddy) along y, x, and z directions, respectively.

The values of specific rotational and total kinetic energies were estimated for each eddy and for pure methane-air conditions in Fig. 4.12. The logarithmic (with a base of 10) joint probability density functions (JPDF) of KE_ω and KE versus $\mathcal{R}$ are presented in the first and second rows of Fig. 4.13, respectively. The first, second, third, and fourth columns pertain to conditions U5H00T0, U35H00T0, U35H00T1, and U35H00T2, respectively. The results in Figs. 4.13(a) and (e) show that eddies related to condition U5H00T0 are not energetic; and as a result, they cannot disturb the flame structure, which is in agreement with the results presented in Figs. 4.1(a–d), Fig. 4.3, and Fig. 4.6(a and e). Compared to condition U5H00T0, results in Figs. 4.13(g) and (h) show that conditions U35H00T1 and U35H00T2 feature a relatively large number of energetic eddies with radius larger than 0.23 mm. Conditions U35H00T1 and U35H00T2 also feature similar logarithmic JPDFs of KE, which is due to both flames are featuring relatively large mean bulk flow velocity of

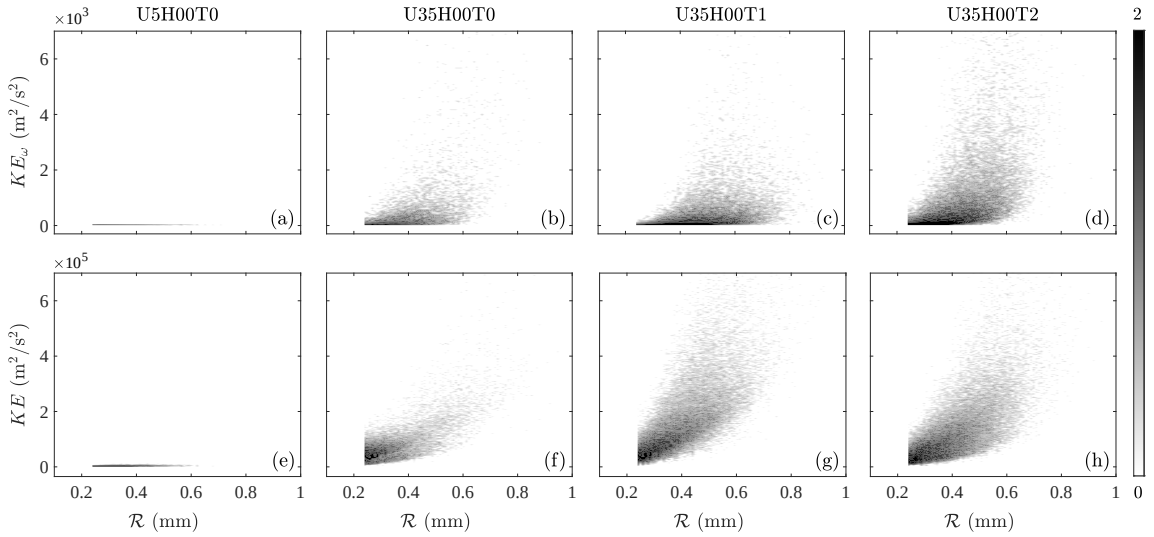

Fig. 4.13. Logarithmic joint probability density functions of (a–d) rotational kinetic energy (KE_ω), and (e–h) total kinetic energy (KE) versus eddy sizes ($\mathcal{R}$) for conditions U5H00T0, U35H00T0, U35H00T1, and U35H00T2.

35 m/s. However, comparing the results in Figs. 4.13(c) and (d) suggests that the rotational kinetic energy of the eddies related to condition U35H00T2 ($Ka = 76.0$) is significantly larger than that related to condition U35H00T1 ($Ka = 13.7$). The results in Fig. 4.13 along with those in Fig. 4.3 show that compared to the total kinetic energy, the rotational kinetic energy plays a more dominant role in determining the quality of the interaction between turbulent eddies and the internal structure of the investigated turbulent premixed flames. Results also suggest that for a given turbulence generating mechanism, increasing the Karlovitz number increases the number of the energetic eddies with radius of $\mathcal{R} \gtrsim$ 0.23 mm.

For the largest tested Karlovitz number (condition U35H00T2, see Table 2.1), comparison of the values of the integral ($\Lambda = 5.1$ mm) and Kolmogorov ($\eta = 0.01$ mm) length scales estimated in the cold flow with the smallest flow structure diameter that can be detected (0.47 mm, see Appendix F) suggests that the diameter of the smallest eddies resolved in the current thesis is about 10 times smaller than the corresponding integral length scale and is about 50 times larger than the Kolmogorov length scale. This means that our resolution cannot resolve the smallest eddies in the flow. The smallest detectable eddy (diameter of

0.47 mm) is on the order of the Taylor length scale estimated in the cold flow, see l_T in Table 2.1. Thus, it can be inferred that the measurements allow for resolving eddies with size close to the Taylor length scale and larger. In fact, as shown in Fig. 4.9, such eddies penetrate into the preheat zone. Values of the Kolmogorov and Taylor length scales were also estimated at 1500 K ($\eta_K{}^*$ and $l_T{}^*$, see Eqs. (1.15) and (1.16)). The results suggest that for condition U35H00T2, both $\eta_K{}^* = 0.1$ mm and $l_T{}^* = 0.38$ mm are smaller than the measured preheat and reaction zone thicknesses (2.25 and 1.13 mm, respectively). The relatively small size of $\eta_K{}^*$, $l_T{}^*$, and the resolved eddies (with diameter larger than 0.47 mm) compared to the reaction zone thickness (1.13 mm) along with the relatively pronounced rotational kinetic energy of the resolved eddies shown in Fig. 4.13(d) could suggest that vortices may have also penetrated into the reaction zone.

Interaction of the Taylor-size eddies with the reaction zone was hypothesized by Zimont [173] and reviewed by Driscoll [6]. For premixed flames of a different fuel (n-heptane), Lapointe et al. [172] performed DNS. The value of $u'/S_{L,0}$ for their most turbulent condition is similar to that tested in the present study. Two instantaneous iso-surfaces of temperature overlaid on the contours of vorticity presented in Fig. 4 of [172] show that increasing the turbulence intensity increases the vorticity of eddies in the reactants/preheat zones, and increases the distance between the iso-surfaces (which is related to the reaction zone thickness). These two observations are in agreement with the results presented in Figs. 4.3, 4.10, and 4.11. However, the velocity data inside the reaction zone is not available in the present thesis, and as a result, broadening of the reaction zone being due to penetration of turbulent eddies is not experimentally demonstrated. Also, since the eddy size is obtained based on the planar PIV measurements, the flow three-dimensionality can influence the reported eddy sizes as well. Both the three-dimensional nature of the eddies (and its influence on the reported eddy size) and their penetration into the reaction zone remain to be investigated experimentally.

Comparing the specific kinetic energy for conditions U35H00T0 and U35H00T1 (see the second and third columns of Fig. 4.13) shows that the number of high energy eddies is larger for U35H00T1 compared to U35H00T0. However, the results presented in Fig. 4.3 showed that the preheat and reaction zone thicknesses of condition U35H00T0 are larger than those of U35H00T1. This implies that, other than the specific kinetic energy of the eddies, there should be another reason for the broadening of these zones. The analyses show that while the reaction zones in condition U35H00T1 are surrounded by hot products, reaction zones in condition U35H00T0 are exposed to room air (compare the yellow regions, which pertain to the combustion products, in Figs. 4.9(f) and (g)) and this may play a role in the broadening of preheat and reaction zones. In fact, it is hypothesized that air entrainment dilutes the reactants and decreases the local ϕ [49, 124, 125] generating stratification. The local burning rate and adiabatic temperature decrease, local Ka increases, and the preheat and reaction zone thicknesses increase (similar arguments are provided in [49]). Thus, in addition to the relative size and energy of turbulent eddies (compared to preheat and reaction zones thicknesses) discussed in this section, the lack of back-support and air entrainment may play a role in the broadening of preheat and reaction zones reported in this thesis. The air entrainment can be accompanied by flame extinction events at large background turbulence intensities. For such conditions, eddies may locally extinct or broaden the reaction zone. It is speculated that flame extinctions and broken reaction zones lead to incomplete combustion. As a result, the combustion temperature decreases, and this also facilitates broadening of the reaction zone [6, 49]. The relation between the occurrence of local extinction events and possible broadening of the preheat and reaction zones (and the non-flamelet behavior) are not well understood in the literature and is discussed in Chapter 6.

Chapter 5

Burning velocity of turbulent premixed flames at large turbulence intensities

This chapter is divided into four sections. In the first one, the local consumption speed is investigated for premixed flames. In the second section, a parameter is introduced, which allows to estimate the burning velocity of the premixed flames and does not depend on the flamelet behavior. In the third section, the reason for the underprediction of local consumption speed and the existing discrepancy between this parameter and the global consumption speed is investigated. In the fourth section, the bending behavior for the burning velocity of the premixed flames is studied.

5.1 Local consumption speed

Prior to calculation of the heat release rate marker/burning velocity and for comparison purposes, the local consumption speed is estimated here first. This requires calculation of the mean progress variable field and the two dimensional flame surface density. The reduced OH PLIF images were utilized to obtain the mean progress variable ($\overline{c}_{\mathrm{OH}}$) in the present thesis similar to the studies of [11, 91, 92]. In order to obtain the $\overline{c}_{\mathrm{OH}}$ contours, the OH PLIF images were binarized and the binarized images were averaged over 500 frames. To

select a threshold value for OH PLIF signals, Cantera simulations of freely propagating laminar flames (with $\phi = 0.7$ and H_2 ranging from 0% to 70%) were used. The freely propagating laminar flame simulations show that, for all of the tested hydrogen-enrichment percentages, the location of maximum heat release rate (flame front location) corresponds to a location at which the normalized value of the synthetic OH PLIF signal attains ∼30% of the corresponding maximum value. Nevertheless, due to the steep gradient of the OH PLIF variation across the flame region, the mean progress variable is not substantially sensitive to the selected threshold value. More details are provided in Chapter 1.

The two-dimensional flame surface density (used in Eq. (1.19b)) was estimated by considering an interrogation window with the size of 1.5×1.5 mm^2 at a given point (see Fig. 1.4 and the relevant discussions in Chapter 1). Then, the averaged flame front length inside that window was calculated. The ratio of the average flame front length to the interrogation window area was used to estimate the flame surface density, similar to, e.g. [174, 175]. It was confirmed that increasing this window size upto about 4×4 mm^2 does not change the flame surface density results considerably. The two-dimensional variation of Σ pertaining to test conditions of U5H70T0, U35H70T1, and U35H70T2 are shown in Fig. 5.1(a–c), respectively. As can be seen, at a fixed H_2% and mean bulk flow velocity (compare Figs. 5.1(b) and (c)), increasing the turbulence intensity (by increasing the number of turbulence generators) significantly increases the flame brush thickness, while the maximum flame surface density remains constant and about 0.45 1/mm.

Equation (1.19b) pertains to integration in the $\eta - \xi$ coordinate system. The integral of flame surface density in the $\eta - \xi$ coordinate system is equal to that in the Cartesian coordinate system, see for example [11]. Thus, following Wabel et al. [11], Eq. (1.19b) can be simplified, allowing for calculations in the Cartesian coordinate system (instead of $\eta - \xi$

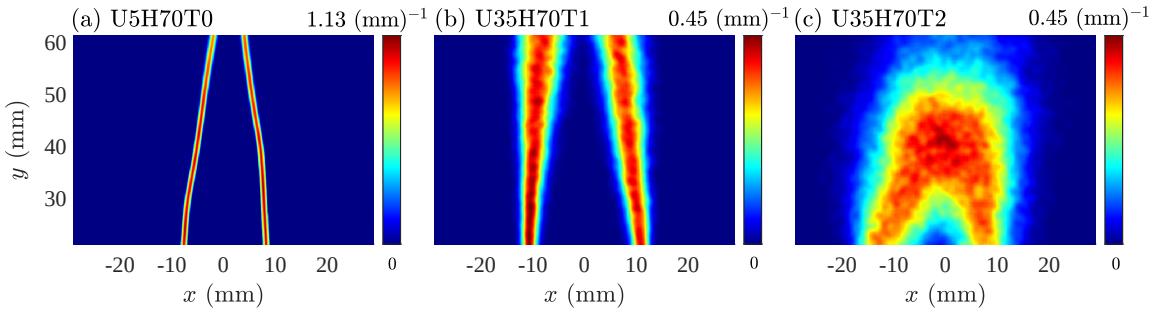

Fig. 5.1. Flame surface density estimated for test conditions of (a) U5H70T0, (b) U35H70T1, and (c) U35H70T2.

coordinate system). This equation can be written as

$$S_{\mathrm{T,LC}} = \frac{S_{\mathrm{L},0} I_0}{L_\xi} \int_{y_{\min}}^{y_{\max}} \int_{x_{\min}}^{x_{\max}} \Sigma(x,y) \mathrm{d}x \mathrm{d}y. \tag{5.1}$$

In Eq. (5.1), $x_{\min} = -30$, $x_{\max} = 30$, $y_{\min} = 21$, and $y_{\max} = 60$ mm, which mark the extents of the integration domain. Please note that in Eq. (5.1), the stretch factor (I_0) is assumed to be unity, similar to [11], since the effective Lewis number is close to unity for the tested conditions of the present study (please see the last columns of Tables 2.1 and 2.2 as well as the discussions provided in Chapter 1). The significance of using a proper laminar flame speed for local consumption speed calculation is highlighted in the study of Chakraborty et al. [176]. Also, studies of [177, 178] suggest that even for pure methane-air flames, stretch factor can increase upto about 50%. Nevertheless, measuring the stretch factor is one of the limitations of the current thesis and future investigations are required to study the effect of locally varying stretch factor on $S_{\mathrm{T,LC}}$. In addition to the effect of stretch factor, two other factors can lead to uncertainty in calculation of the local consumption speed. These are the three dimensional nature of the flames and the limitation for resolving the flame surface area. Three dimensional simulations of the premixed flames suggest that the two dimensional flame surface density would have been 15 to 30% larger provided the 3D data was experimentally available, see for example [76, 160, 165]. For the integral length scales similar to those of the present study, Wang et al. [12] show that improving the imaging

resolution from 42 to 24 μm increases the flame surface density by about 10%. Also, Skiba et al. [179] showed that, for the turbulence intensity of about 124 (which is larger than those tested in the present study), improving the resolution from 330 to 54 μm increases the estimated flame surface density by about 33%. In essence, combination of the above factors can potentially lead to about 140% increase in estimation of the local consumption speed values. Nevertheless, further investigations are required to study the effects of the aforementioned factors on the local consumption speed. Similar to several past studies (for example [11, 12]), such effects are not considered in here.

The local consumption speed was estimated using Eq. (5.1), and the results are presented in Fig. 5.2(a) for all tested conditions of Table 2.1. The results in the figure suggest that, generally, increasing the hydrogen-enrichment percentage increases the local consumption speed, which is due to the increased unstretched laminar flame speed of the reactants. Variation of the local consumption speed normalized by the freely propagating laminar flame speed versus the turbulence intensity is presented in Fig. 5.2(b) for the tested conditions of Table 2.1. The maximum uncertainty in estimation of the local consumption speed is related to the test condition of U35H00T2, and is shown by the error bar in Fig. 5.2(b). The procedure for estimation of the error bar is similar to that discussed in Chapter 4 and does not take into account the three dimensional nature of the flames and the limited imaging resolution. The results in Fig. 5.2(b) are also color-coded based on the integral length scale of the test conditions and presented in Fig. 5.2(c). Overlaid on both Figs. 5.2(b) and (c) are the data points and trends of variations extracted from Wabel et al. [11] and Wang et al. [12], which are highlighted by the red and blue colors, respectively. The integral length scale in the study of Wabel et al. [11] varies between 6.1 and 41 mm and that in Wang et al. [12] is 2.9 mm. As can be seen, variation of $S_{\mathrm{T,LC}}/S_{\mathrm{L},0}$ is significantly dependent on the integral length scale and follows two trends. For $\Lambda \lesssim 4$ mm, our results suggest that the normalized local consumption speed plateaus at about 2 following [12]; and, for $\Lambda \gtrsim 4$ mm,

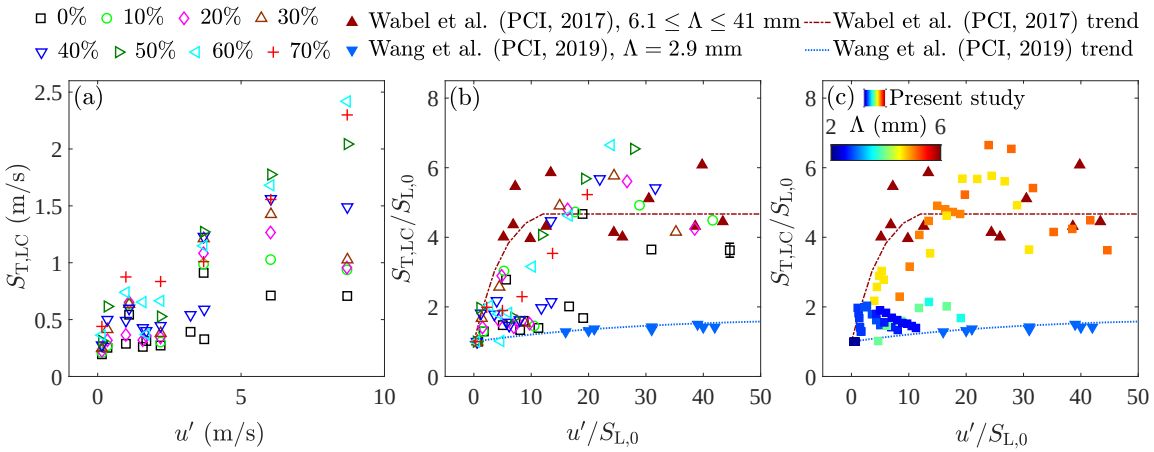

Fig. 5.2. (a) Local consumption speed ($S_{T,LC}$) versus u', (b) normalized local consumption speed ($S_{T,LC}/S_{L,0}$) versus $u'/S_{L,0}$, and (c) presents results in (b) color-coded based on the corresponding tested integral length scale.

$S_{T,LC}/S_{L,0}$ plateaus at about 5 following [11]. Plateau of the normalized local consumption speed with increase of the turbulence intensity (evident in Fig. 5.2) has been a matter of discussions in the literature. Several investigations [6, 9, 11, 12] suggested the reason for this plateau is saturation of the flame surface area with increase of $u'/S_{L,0}$ at large values of this parameter. However, the results presented in Fig. 4.3 as well as those in [12, 36, 37, 43–49] suggest that increasing the turbulence intensity broadens both the preheat and reaction zones, and as a result, the flamelet assumption may not hold for such conditions. This means that Eq. (1.19b), which is developed based on the flamelet assumption, may lead to an inaccurate estimation of the local consumption speed. Instead, in the next section, we propose a new formulation that does not rely on the flamelet assumption, which is discussed in the following.

5.2 Heat release rate marker of premixed flames

In order to develop a formulation that does not take into account the flamelet assumption, first, similar to [11, 12, 91, 92] and identical to the procedure discussed in the previous section, the OH PLIF images are binarized and the mean progress variable field ($\overline{c}_{OH}$) is obtained by averaging the binarized images. Please note this binarization is only performed

to calculate the mean progress variable fields, is conducted for flames that are reported to be both relatively thin [11] and thick [12], and does not necessarily imply a presumed structure for the reaction zone. Then, a curvilinear coordinate system $(\xi - \eta)$, with ξ and η being respectively tangent and normal to $\overline{c}_{\mathrm{OH}}$ contours are constructed. The time-average heat release rate is integrated along $\eta-$axis, which is locally normal to the mean progress variable contours of $\overline{c}_{\mathrm{OH}} = 0.5$. This integral depends on ξ and is given by

$$B_{\mathrm{T},\xi}(\xi) = \int_{\eta_{\min}}^{\eta_{\max}} \overline{HRR}_{\mathrm{T}}(\eta, \xi)\mathrm{d}\eta, \tag{5.2}$$

where $\overline{HRR}_{\mathrm{T}}(\eta, \xi)$ is the mean heat release rate of turbulent flames estimated locally. $\eta_{\min}$ and $\eta_{\max}$ are the extents of the $\eta-$axis in the domain of investigation. The turbulent flame burning rate (B_{T}) is defined as the spatially averaged (along ξ) value of $B_{\mathrm{T},\xi}(\xi)$ and is given by

$$B_{\mathrm{T}} = \frac{1}{\underbrace{\int_{\xi_{\min}}^{\xi_{\max}} \mathrm{d}\xi}_{L_{\xi,\mathrm{T}}}} \int_{\xi_{\min}}^{\xi_{\max}} \underbrace{\int_{\eta_{\min}}^{\eta_{\max}} \overline{HRR}_{\mathrm{T}}(\eta, \xi)\mathrm{d}\eta}_{B_{\mathrm{T},\xi}(\xi)} \mathrm{d}\xi. \tag{5.3}$$

In Eq. (5.3), $\xi_{\min}$ and $\xi_{\max}$ correspond to the boundaries of $\xi-$axis in the domain of investigation. In the denominator of Eq. (5.3), $L_{\xi,\mathrm{T}}$ is the length of $\overline{c}_{\mathrm{OH}} = 0.5$ contour and depends on the tested condition. Similarly, the laminar flame burning rate can be estimated from

$$B_{\mathrm{L}} = \frac{1}{L_{\xi,\mathrm{L}}} \int_{\xi_{\min}}^{\xi_{\max}} \int_{\eta_{\min}}^{\eta_{\max}} \overline{HRR}_{\mathrm{L}}(\eta, \xi)\mathrm{d}\eta\mathrm{d}\xi, \tag{5.4}$$

where $\overline{HRR}_{\mathrm{L}}(\eta, \xi)$ and $L_{\xi,\mathrm{L}}$ are the mean laminar flame heat release rate estimated locally and the laminar flame length estimated using the length of $\overline{c}_{\mathrm{OH}} = 0.5$. Estimation of the turbulent and laminar burning rates requires information regarding the true heat release rate, which can be available from DNS studies, see for example [84, 90, 97, 180]. However, the true heat release rate is not available experimentally, and the planar laser induced

fluorescence of OH and CH_2O is used to visualize the heat release rate, see for example [59, 66]. This is because the reaction of OH and CH_2O leads to generation of the formyl radical which is directly related to the heat release rate [59, 60] (see Chapter 1) for small and moderate turbulence intensities. However, at large turbulence intensities, recent studies [47, 66] suggest that the reaction of OH and CH_2O is not the only pathway to generation of heat. Thus, it is acknowledged that I_{HRR} (with details of estimation discussed in Chapter 3) is merely an approximate local marker of the heat release rate. Considering the above discussions, $\overline{HRR}$ in Eqs. (5.4) and (5.3) is replaced by $\overline{I}_{\mathrm{HRR}}$.

$$\mathcal{M}_{\mathrm{L}} = \frac{1}{L_{\xi,\mathrm{L}}} \int_{\xi_{\min}}^{\xi_{\max}} \int_{\eta_{\min}}^{\eta_{\max}} \overline{I}_{\mathrm{HRR,L}}(\eta,\xi)\mathrm{d}\eta\mathrm{d}\xi, \tag{5.5a}$$

$$\mathcal{M}_{\mathrm{T}} = \frac{1}{L_{\xi,\mathrm{T}}} \int_{\xi_{\min}}^{\xi_{\max}} \int_{\eta_{\min}}^{\eta_{\max}} \overline{I}_{\mathrm{HRR,T}}(\eta,\xi)\mathrm{d}\eta\mathrm{d}\xi. \tag{5.5b}$$

where $\mathcal{M}_{\mathrm{L}}$ and $\mathcal{M}_{\mathrm{T}}$ are referred to as the laminar and turbulent heat release rate markers, respectively. The integral of the heat release rate marker in the $\eta - \xi$ coordinate system is equal to that in the Cartesian coordinate system. As a result, Eqs. (5.5a and 5.5b) can be further simplified to

$$\mathcal{M}_{\mathrm{L}} = \frac{1}{L_{\xi,\mathrm{L}}} \int_{y_{\min}}^{y_{\max}} \int_{x_{\min}}^{x_{\max}} \overline{I}_{\mathrm{HRR,L}}(x,y)\mathrm{d}x\mathrm{d}y, \tag{5.6a}$$

$$\mathcal{M}_{\mathrm{T}} = \frac{1}{L_{\xi,\mathrm{T}}} \int_{y_{\min}}^{y_{\max}} \int_{x_{\min}}^{x_{\max}} \overline{I}_{\mathrm{HRR,T}}(x,y)\mathrm{d}x\mathrm{d}y. \tag{5.6b}$$

Although the true heat release and burning rates cannot be estimated in this thesis, the values of the heat release rate marker estimated for nearly laminar flames of this thesis can be compared against the laminar burning rate of a freely propagating flame ($B_{\mathrm{L},0}$) as well as the unstretched laminar flame speed, both obtained from Cantera simulations using GRI-Mech 3.0. Values of $\mathcal{M}_{\mathrm{L}}$ compared against $B_{\mathrm{L},0}$ and $S_{\mathrm{L},0}$ are presented in Figs. 5.3(a) and (b), respectively. As can be seen, increasing the hydrogen-enrichment percentage from 0%

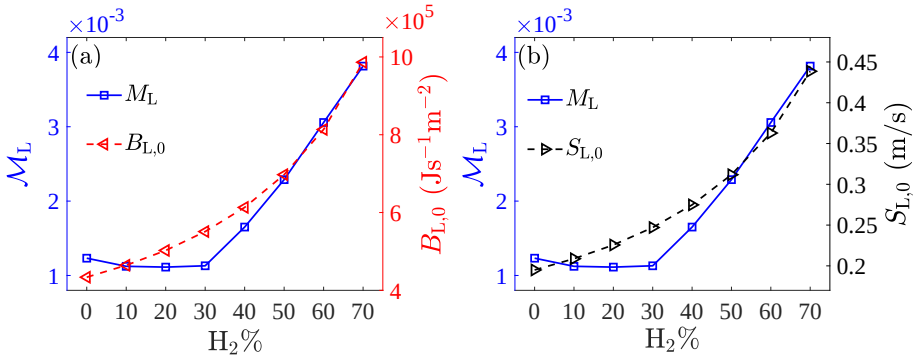

Fig. 5.3. Variations of the heat release rate marker estimated for nearly laminar premixed flames versus hydrogen-enrichment percentage compared against (a) burning rate of the corresponding freely propagating laminar flame and (b) the corresponding unstretched laminar flame speed. $\phi = 0.7$ for all presented data points.

to 70% increases $\mathcal{M}_L$, $B_{L,0}$, and $S_{L,0}$ by about 3.4, 2.8, and 2.4 folds, respectively. Results presented in Fig. 5.3 suggest that, for nearly laminar premixed flames, the formulation presented in Eq. (5.6a) for estimation of the nearly laminar premixed flames heat release rate marker yields similar results to laminar burning rate and the unstretched laminar flame speed.

Dividing Eq. (5.6b) by Eq. (5.6a) leads to

$$\frac{\mathcal{M}_T}{\mathcal{M}_L} = \frac{L_{\xi,L}}{L_{\xi,T}} \frac{\int_{y_{min}}^{y_{max}} \int_{x_{min}}^{x_{max}} \overline{I}_{HRR,T}(x,y)\mathrm{d}x\mathrm{d}y}{\int_{y_{min}}^{y_{max}} \int_{x_{min}}^{x_{max}} \overline{I}_{HRR,L}(x,y)\mathrm{d}x\mathrm{d}y}. \tag{5.7}$$

Equation (5.7) allows for estimation of the turbulent flame heat release rate marker normalized by that for the laminar flame counterpart. It was argued in Chapter 3 that I_{HRR} was thresholded by 30% of the global maximum. Our sensitivity analysis shows that changing this threshold value between 27% and 33% (i.e. ±10% of the selected threshold) changes $\mathcal{M}_T/\mathcal{M}_L$ by a maximum of about ±4% for all tested conditions. Equation (5.7) does not presume a given internal flame structure. In fact, in the following, it is shown that for flames whose internal structure follows the flamelet assumption, Eq. (5.7) leads to variation of the heat release rate marker with turbulence intensity similar to those obtained utilizing the formulation proposed by Driscoll [34], i.e. Eq. (1.19b).

Variation of $\mathcal{M}_{\mathrm{T}}$ versus u' for all tested conditions are presented in Fig. 5.4(a), highlighting the effect of hydrogen-enrichment. As can be seen, generally, increasing the hydrogen-enrichment increases $\mathcal{M}_{\mathrm{T}}$. Variation of $\mathcal{M}_{\mathrm{T}}/\mathcal{M}_{\mathrm{L}}$, estimated from Eq. (5.7), versus $u'/S_{\mathrm{L},0}$ is presented in Figs. 5.4(b). The maximum uncertainty associated with calculation of $\mathcal{M}_{\mathrm{T}}/\mathcal{M}_{\mathrm{L}}$ pertains to test condition of U35H00T2, which is shown by the error bar in the figure. Among the formulations proposed in the literature, see for example the review paper by Driscoll [34], derivation of the global consumption speed formulation does not necessarily depend on the flamelet assumption, and as a result, $S_{\mathrm{T,GC}}/S_{\mathrm{L},0}$ can be compared to $\mathcal{M}_{\mathrm{T}}/\mathcal{M}_{\mathrm{L}}$. Since the field of view of the present investigation is relatively small, the normalized global consumption speed values cannot be estimated for the present investigation; however, $S_{\mathrm{T,GC}}/S_{\mathrm{L},0}$ associated with the studies of [11, 12] are overlaid on Fig. 5.4 by the red dotted-dashed and blue dotted curves. It is important to note that, although extinctions (and as a result fuel escape) can occur for the test conditions of the present study (see for example the results in Fig. 4.1(l and p)), the values of the heat release rate marker can be compared against the normalized global consumption speed reported in, e.g. the study of [55], in which a significant flame extinction is not reported. This is because, once extinctions occur, both the numerator and the denominator of Eq. (5.6b) change accounting for such occurrence. In fact, compared to Eq. (1.19a) that may not be appropriate for calculation of the global consumption speed for events that extinctions and fuel escape happen, Eq. (5.6b) allows for such calculations.

Two trends can be observed for the variation of the normalized heat release rate marker versus the turbulence intensity. In order to highlight these trends, the data presented in Fig. 5.4(b) is color-coded based on the tested integral length scale and presented in Fig. 5.4(c). The results in the figure show that, at a fixed value of $u'/S_{\mathrm{L},0}$, increasing the integral length scale increases the normalized heat release rate marker and the normalized global consumption speed. A similar observation for the global consumption speed was

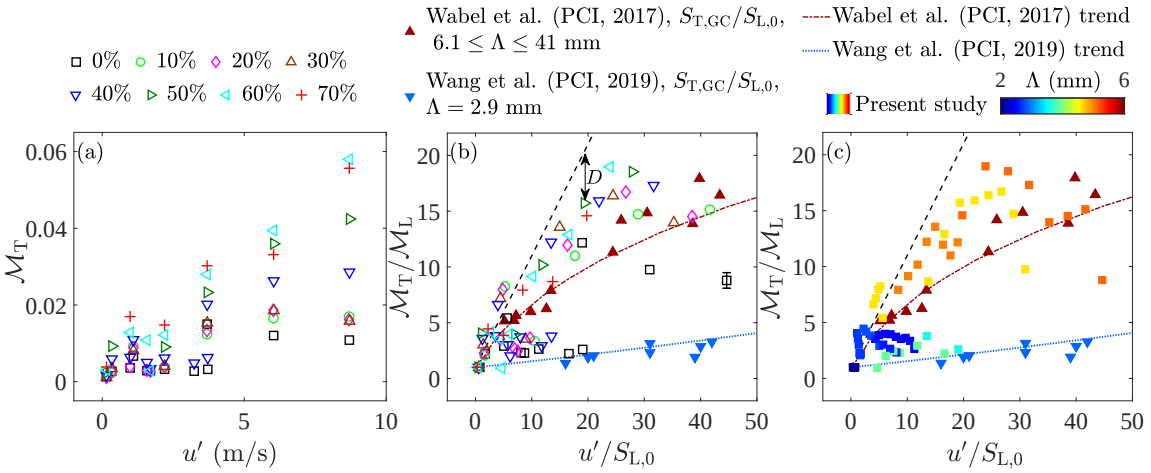

Fig. 5.4. Variations of (a) the heat release rate marker versus u' and (b) the normalized heat release rate marker ($\mathcal{M}_T/\mathcal{M}_L$) versus $u'/S_{L,0}$. (c) presents the results in (b) color-coded based on the tested integral length scale.

also reported in Kim et al. [181]. As evident in the figure, for $\Lambda \lesssim 4$ mm, the values of $\mathcal{M}_T/\mathcal{M}_L$ are close to the normalized global consumption speed pertaining to the study of Wang et al. [12]; however, for $\Lambda \gtrsim 4$ mm, the results are closer to those of Wabel et al. [11]. Comparison of the results presented in Fig. 5.4 with those in Fig. 5.2 suggests that the values of $\mathcal{M}_T/\mathcal{M}_L$ and $S_{T,GC}/S_{L,0}$ are similar, and they are both significantly larger than those of $S_{T,LC}/S_{L,0}$. The reason for this discrepancy is investigated in the next section.

5.3 Discrepancy between the local and global consumption speeds/heat release rate marker

In order to study the reason for the disparity between the values of the normalized heat release rate marker and the normalized local consumption speed, the following parameter is defined.

$$J = \frac{\mathcal{M}_T/\mathcal{M}_L}{S_{T,LC}/S_{L,0}}. \tag{5.8}$$

Variation of J versus $u'/S_{L,0}$ for the tested conditions of Table 2.1 is shown in Fig. 5.5 by the open black circular data symbol. The results presented in the figure show that the values of J are larger than unity, and this parameter, generally, increases with increasing $u'/S_{L,0}$. As

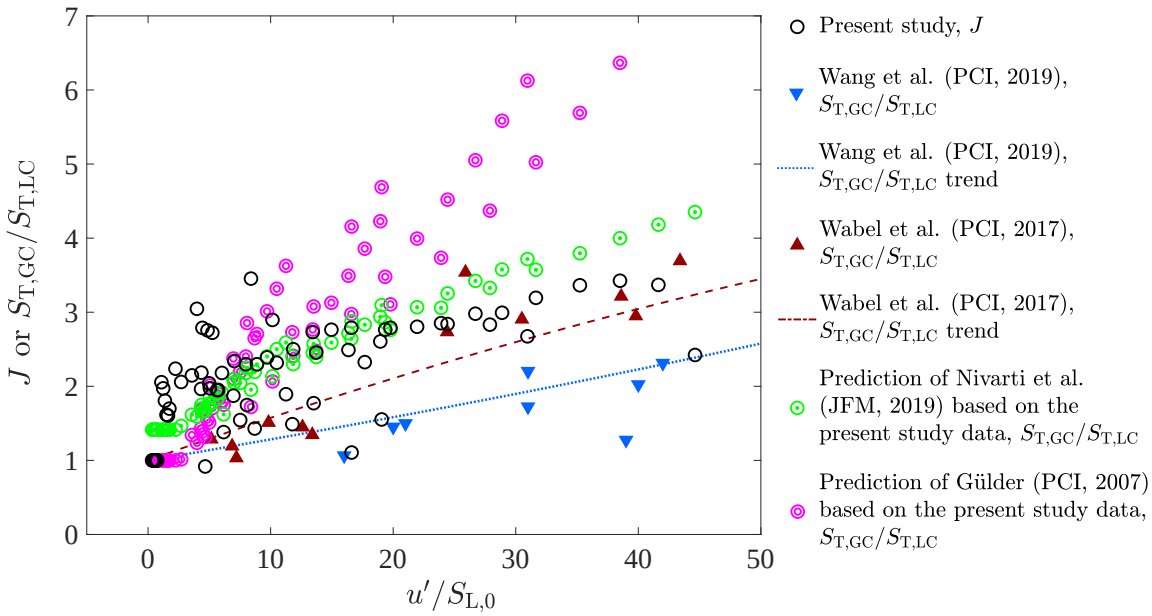

Fig. 5.5. The normalized heat release rate marker predicted by Eq. (5.7) or the global consumption speed divided by the local consumption speed versus turbulence intensity.

can be seen, for moderate turbulence intensities, the values of J are scattered. The reason for this is linked to the different utilized turbulence generating mechanisms whose relation to the internal flame structure (related to the heat release marker and local consumption speed) is studied in Chapter 4. Variation of the normalized global consumption speed divided by the normalized local consumption speed (i.e. $S_{T,GC}/S_{T,LC}$) is extracted from the studies of Wabel et al. [11] and Wang et al. [12], and their results are presented in Fig. 5.5 by the solid dark red and blue triangular data symbols, respectively. The trends of their results are also obtained and overlaid on the diagram (see dashed and dotted curves). Agreeing with the results of this thesis, those of past investigations [11, 12] also suggest that the local consumption speed underpredicts the turbulent premixed flames burning velocity.

The potential underlying reason for the underprediction of the burning velocity by the local consumption speed has been a matter of discussion over the past decades, see the review paper by Driscoll et al [6]. Gülder [10] and Nivarti et al. [9] suggested that the reason for the observed difference between the local and global consumption speed values can be explained by taking into account the enhanced diffusivity of the reactants due to penetration of small

scale eddies into the flame region. Using the mathematical formulations proposed by Nivarti et al. [9], see Eq. (1.23), and Gülder [10], see Eq. (1.22), as well as the non-dimensional parameters related to the test conditions of the present thesis (Ka, $u'/S_{\mathrm{L},0}$, and $Re_{l_{\mathrm{T}}} = u'l_{\mathrm{T}}/\nu$), the ratio of the global to local consumption speed was estimated and the results are presented in Fig. 5.5 by the green dot-and-circle as well as the pink double circle data symbols, respectively. As can be seen, the ratio of the normalized heat release rate marker to normalized local consumption speed in this study (J, the black circular data points) is close to the ratio of the global and local consumption speeds reported in the literature [11, 12]. Also, the results estimated based on the mathematical formulation proposed in Nivarti et al. [9] for $S_{\mathrm{T,GC}}/S_{\mathrm{T,LC}}$ agrees well with J obtained in the present thesis. However, values of the global consumption speed divided by the local consumption speed obtained based on Gülder's formulation [10] deviates from those of the thesis and other experimental results [11, 12] at large turbulence intensities. The reason for the deviation of the results of this thesis and past investigations [11, 12] from the prediction of the formulation provided by Gülder [10] is speculated to be possibly linked to the assumptions made for derivation of the formulation in [10]. Specifically, Gülder [10] assumed that the enhanced diffusivity occurs only at the Taylor length scale, while Nivarti et al. [9] considered enhancement of diffusivity at all length scales smaller than the laminar flame thickness.

The reason for the increasing trend pertaining to variations of J and $S_{\mathrm{T,GC}}/S_{\mathrm{T,LC}}$ with $u'/S_{\mathrm{L},0}$ is hypothesized to be linked to the internal structure of the tested flames. In order to investigate this hypothesis, variations of J verses the preheat and reaction zone thicknesses are shown in Figs. 5.6(a) and (b), respectively. As can be seen, $\delta_{\mathrm{P}}/\delta_{\mathrm{P,L}}$ and $\delta_{\mathrm{F}}/\delta_{\mathrm{F,L}}$ are positively correlated with J. Such correlation is even more pronounced for the reaction zone thickness and follows a linear trend ($J \approx 1.9(\delta_{\mathrm{F}}/\delta_{\mathrm{F,L}}) - 0.9$). One may argue that the positive correlations presented in Fig. 5.6 are self-fulfilling as both J and the preheat/reaction zone thicknesses are estimated from the PLIF measurements, and that broader flames au-

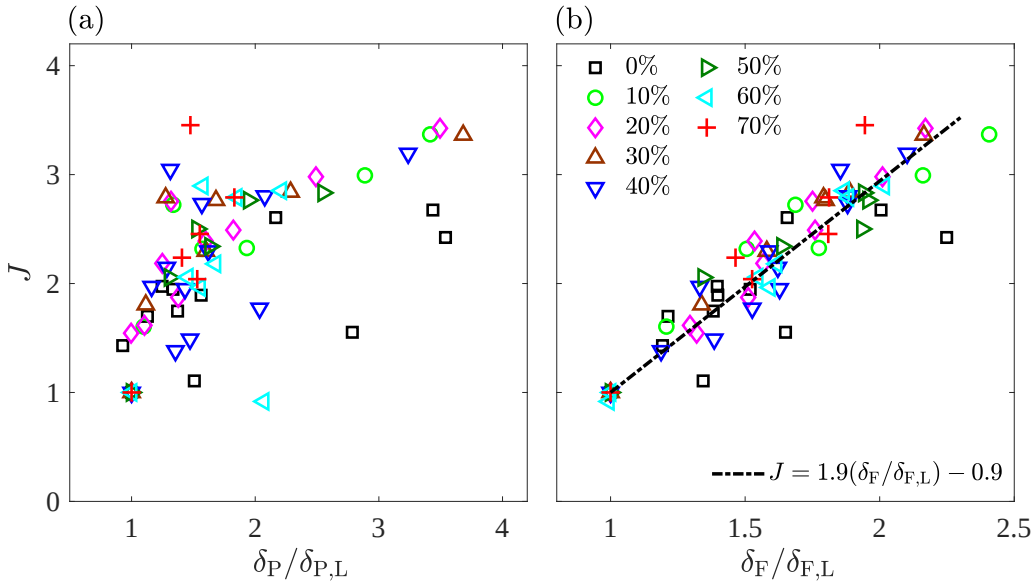

Fig. 5.6. The ratio of the normalized heat release rate marker and the normalized local consumption speed versus (a) the preheat and (b) the reaction zone thicknesses normalized by those of the corresponding laminar flame counterparts. Overlaid on (b) is the linear fit to the data.

tomatically generate larger integrand of Eq. (5.6b). In order to elaborate the reason the correlations in Fig. 5.6 are not self-fulfilling, the ratio of the global and local consumption speeds ($S_{T,GC}/S_{T,LC}$) were estimated using the formulations of Nivarti et al. [9], see Eq. (1.23), and Gülder [10], see Eq. (1.22). This parameter is independent of the heat release rate marker and depends on the test conditions of the present thesis. Variations of $S_{T,GC}/S_{T,LC}$ versus the normalized preheat and reaction zone thicknesses are presented in Figs. 5.7(a) and (b), respectively. The results estimated from the formulations of Nivarti et al. [9] and Gülder [10] are shown by the green dot-circle and pink double circle data points, respectively. The results presented in Figs. 5.7(a) and (b), similar to those in Fig. 5.6, also suggest a positive correlation between the preheat/reaction zone thickness and the ratio of the global and local consumption speeds. It is important to highlight that $S_{T,GC}/S_{T,LC}$ presented in Fig. 5.7 is not estimated based on the PLIF measurements of the present study, and the positive correlations seen in Fig. 5.6 are not self-fulfilling.

The correlation between J and $\delta_F/\delta_{F,L}$ suggests that, at the limit of $\delta_F = \delta_{F,L}$, where the flamelet assumption holds, the normalized heat release rate marker estimated from Eq. (5.7)

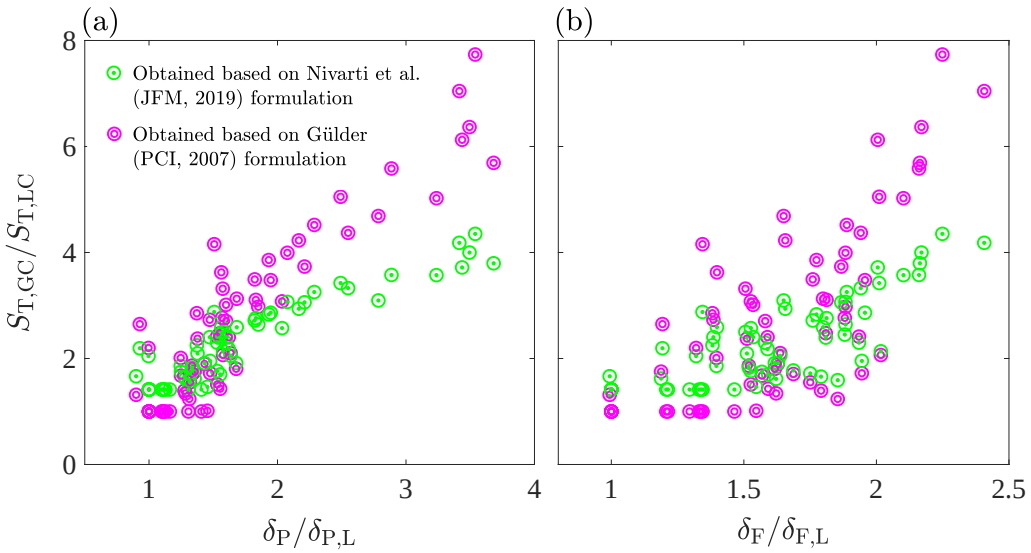

Fig. 5.7. The ratio of the global and local consumption speeds versus (a) the normalized preheat and (b) the reaction zone thicknesses. $S_{T,GC}/S_{T,LC}$ is estimated from the formulations in the studies of [9] and [10].

equals the normalized local consumption speed estimated from Eq. (1.19b). However, increasing the reaction zone thickness leads to larger values of the normalized heat release rate marker compared to the normalized local consumption speed. This means that thickening of the turbulent premixed flames is linked to the deviation of the normalized heat release rate marker (and the normalized global consumption speed) from the corresponding normalized local consumption speed values. In fact, the reason for this deviation being linked to the internal flame structure was speculated by Wabel et al. [11] earlier. However, compared to Wabel et al. [11] who suggested the reason for the difference between $S_{T,GC}$ and $S_{T,LC}$ may be due to the broadening of the preheat zone, our results show such difference is linked to the broadening of both the preheat and reaction zones. It was experimentally shown that (see Chapter 4) with increasing the turbulence intensity, the eddies can penetrate into the preheat zone. This is expected to increase the gas turbulent diffusivity, which increases the burning rate [6, 9, 10, 18], and as a result, the larger than unity values of J presented in Fig. 5.6(a). It is speculated that, similar to the preheat zone, the turbulent eddies may also penetrate into the reaction zone, leading to increase of δ_F (as evident in Fig. 4.3(b) as well as the results presented in [12, 36]), increasing the turbulent diffusivity, and as a result

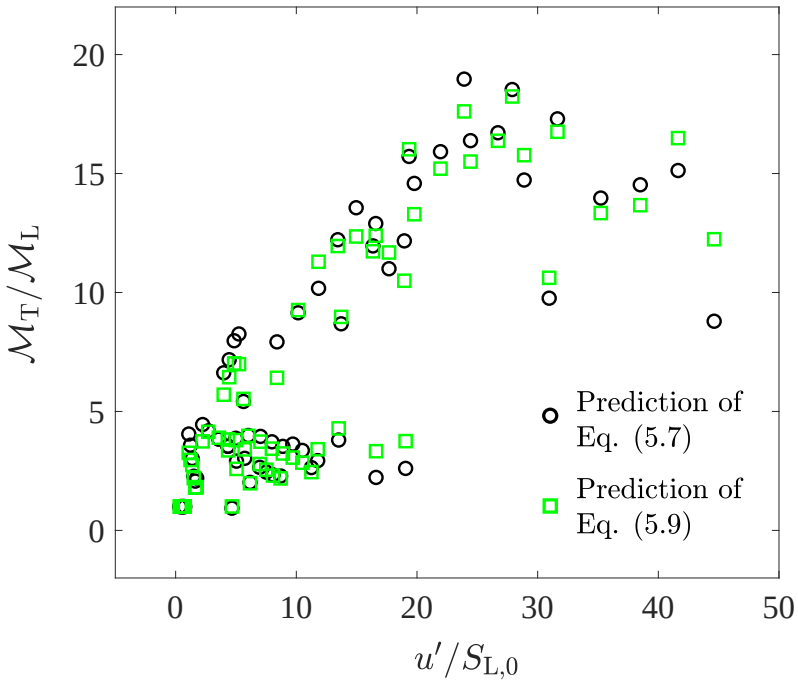

Fig. 5.8. Comparison of the normalized heat release rate marker values estimated from Eqs. (5.7) and (5.9).

increasing the flame burning rate. However, the above speculation (that is penetration of turbulent eddies into the reaction zone) remains to be investigated experimentally.

Results in Fig. 5.6(b) can be combined with Eq. (5.8) to modify the formulation of the local consumption speed suggested by Driscoll et al. [34] accounting for the reaction zone thickening. This equation is given by

$$\frac{\mathcal{M}_T}{\mathcal{M}_L} = \overbrace{[1.9(\delta_F/\delta_{F,L}) - 0.9]}^{J} I_0 \frac{\int_{y_{min}}^{y_{min}} \int_{x_{min}}^{x_{min}} \Sigma(x,y) \mathrm{d}x\mathrm{d}y}{L_\xi}. \tag{5.9}$$

The values of the normalized heat release rate marker estimated from Eq. (5.7) along with the prediction of Eq. (5.9) are presented by the circular and square data symbols in Fig. 5.8 for all test conditions. This figure shows that the local consumption speed corrected for the effect of flame thickening (Eq. (5.9)) follows the values of the heat release rate marker estimated from Eq. (5.7). This suggests the deviation between the global consumption speed and the local consumption speed is likely due to the thickening of the reaction zone.

5.4 Bending behavior of the normalized heat release rate marker

As discussed in the previous section, the disparity between the values of the normalized heat release rate marker/global consumption speed and the normalized local consumption speed can be reconciled considering the reaction zone broadening. However, the reason for variation of $\mathcal{M}_T/\mathcal{M}_L$ versus $u'/S_{L,0}$ bending towards the horizontal axis with increasing the turbulence intensity, see Fig. 5.4, is unclear in the literature, has been a matter of discussions [6], and is investigated here. This behavior is referred to as the bending behavior and is reported in past investigations, see for example [11, 12, 78, 101, 103]. Here, first, the bending behavior is characterized by estimating the difference between the values of the normalized heat release rate marker and the prediction of the Damköhler's first hypothesis [18] (shown by the black dashed line in Fig. 5.4). This difference is referred to as D and is estimated by

$$D = \left(1 + \frac{u'}{S_{L,0}}\right) - \frac{\mathcal{M}_T}{\mathcal{M}_L}. \tag{5.10}$$

For example, at $u'/S_{L,0} = 19.4$ and $H_2\% = 50\%$, D is about 4.6, which is shown by the double-sided arrow in Fig. 5.4(b). D was estimated for all tested conditions in Table 2.1, and the variation of this parameter versus u' is presented in Fig. 5.9(a). As can be seen, increasing u' and the hydrogen-enrichment increases and decreases D, respectively. To normalize for the mixture combustion chemistry, the variation of D is presented versus the turbulence intensity in Fig. 5.9(b). Also overlaid on the figure is the difference between the values of the normalized global consumption speed pertaining to the studies of [11, 12] and the dashed line in Fig. 5.4(b). The estimated values of D are also color-coded based on the integral length scale of the tested conditions and shown in Fig. 5.9(c). As can be seen, D is nearly zero for test conditions corresponding to small turbulence intensities, but it increases with increasing $u'/S_{L,0}$. Also, the results in Fig. 5.9(c) show that, at a given turbulence

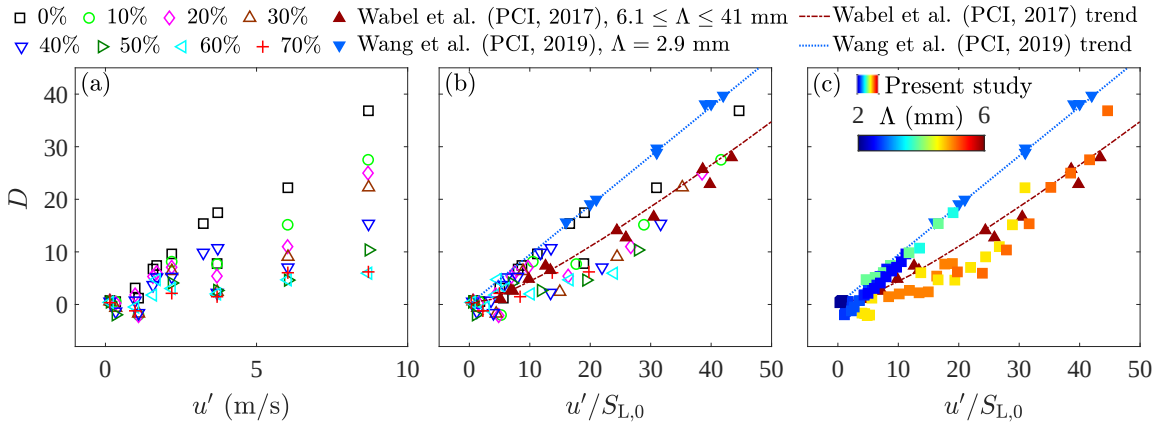

Fig. 5.9. The difference between the normalized global consumption speed/heat release rate marker and the prediction of Damköhler's first hypothesis versus (a) u' and (b) $u'/S_{L,0}$. Overlaid on (b) are the results from the studies of [11, 12]. (c) presents the results in (b) color-coded based on the tested integral length scale values.

intensity, D nearly decreases with increasing the integral length scale.

The reason for the above observations is hypothesized to be linked to pronounced occurrence of flame extinctions and as a result fuel escape at relatively intense turbulence conditions. The hydroxyl radical is a post flame species and its concentration is expected to be positively related to the completion of the combustion process [5, 63]. Thus, it is expected that generation of OH radical should be inversely related to incomplete combustion, the occurrence of extinction events, and potentially the fuel escape. In fact, occurrence of extinctions has been investigated using the OH PLIF signal in the past, see for example the studies of [8, 37, 81, 123, 182–186]. In the present thesis, the number of pixels that feature relatively large values of OH PLIF signal (more than 15% of the maximum) were obtained and averaged for all acquired frames of a given test condition, which is referred to as N_{OH}. In order to facilitate comparison between different test conditions, N_{OH} was normalized by the number of pixels that are expected to feature relatively large time-averaged OH PLIF signal, which is referred to as $N_{\overline{OH}}$. Variation of $(N_{OH}/N_{\overline{OH}})^{-1}$ versus D, u', and $u'/S_{L,0}$ are presented in Figs. 5.10(a), (b), and (c), respectively for the tested flames of Table 2.1. The maximum uncertainty for estimation of $(N_{OH}/N_{\overline{OH}})^{-1}$ corresponds to the test condition of U35H00T2, is estimated using the procedure discussed in Chapter 4, and is shown by the

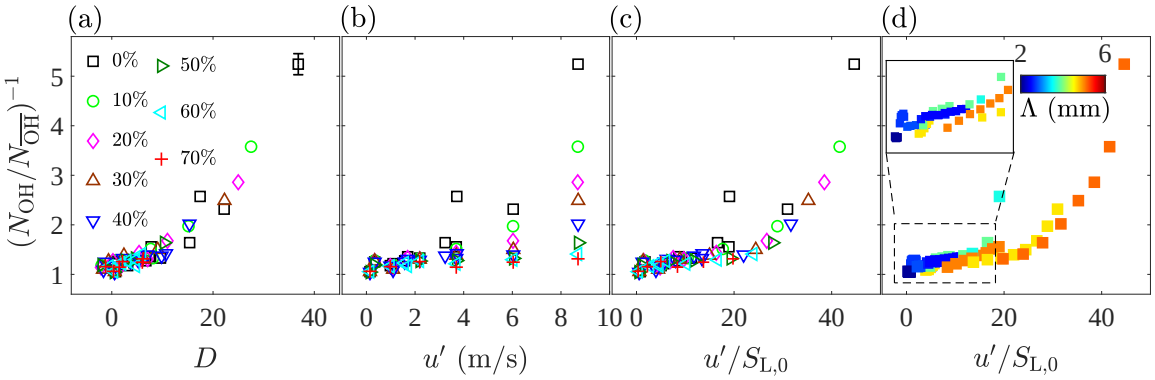

Fig. 5.10. Variations of $(N_{OH}/N_{\overline{OH}})^{-1}$ versus (a) D, (b) u', and (c) $u'/S_{L,0}$. The results in (d) are those in (c) color-coded based on the corresponding tested integral length scale values.

error bar in Fig. 5.10(a). The results in the figure show that $(N_{OH}/N_{\overline{OH}})^{-1}$ is highly correlated with D. One may argue the relation presented in Fig. 5.10(a) may be self-fulfilling as $(N_{OH}/N_{\overline{OH}})^{-1}$ and D are estimated both based on the OH PLIF measurements. In order to confirm the positive correlation in Fig. 5.10(a) is not self-fulfilling, D was estimated using the formulations of [9] and [10] (calculating the global consumption speed using Eqs. (1.23) and (1.22) and finding its deviation from Damköhler's first hypothesis [18]), which do not depend on our PLIF measurements. The results are presented in Fig. 5.11. As can be seen, the formulations of [9] and [10] also confirm increasing D increases $(N_{OH}/N_{\overline{OH}})^{-1}$. The observed correlation suggests that the occurrence of extinctions and incomplete combustion can be potentially related to the observed bending behavior. However, such correlation does not necessitate a causal relation between the bending behavior and the extinctions. In fact, the bending behavior is also reported in previous studies (see for example [11, 12]), in which significant flame extinctions are not reported. Thus, further investigations are required to study a potential causal relation between the extinctions and the bending behavior.

The results presented in Fig. 5.10(b) suggest that increasing the hydrogen-enrichment percentage decreases $(N_{OH}/N_{\overline{OH}})^{-1}$. This is because, especially at larger values of u', adding hydrogen reduces the amount of extinctions (due to the larger reactivity of hydrogen compared to methane [25]). The results presented in Fig. 5.10(c) show that normalizing u' by

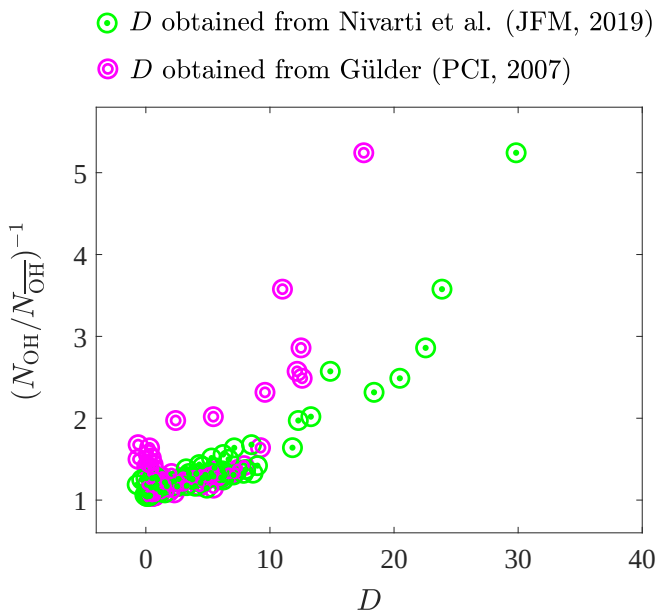

Fig. 5.11. Variations of $(N_{OH}/N_{\overline{OH}})^{-1}$ versus D. The horizontal axis is estimated based on the formulations provided in [9] and [10] (Eqs. (1.23) and (1.22)).

the corresponding laminar flame speed allows for the collapse of the data. Also, it can be seen that increasing the turbulence intensity increases $(N_{OH}/N_{\overline{OH}})^{-1}$. As this parameter increases, the possibility of extinction occurrence increases, the fuel can potentially escape from the flame region, decreasing the generated heat release rate, decreasing $\mathcal{M}_T/\mathcal{M}_L$, and as a result the pronounced deviation of the heat release rate marker from the prediction of the Damköhler's first hypothesis shown in Fig. 5.9. It is acknowledged that for flames similar to those of the present thesis, the room air entrainment, see [8, 123], can influence the bending behavior reported here. Specifically, as discussed in Chapter 4, it is hypothesized that the room air entrainment dilutes the reactants, stratifies the mixture, and locally decreases the fuel-air equivalence ratio [49, 124, 125]. This can locally decrease the burning velocity, which may contribute to the bending behavior. This point is extensively discussed in Chapter 6.

Here, it is of interest to develop a model that allows for predicting the effect of the governing parameters on the occurrence of extinctions, the bending behavior, and as a result the normalized heat release rate marker. To address these, first, the results presented

in Fig. 5.10(c) are color-coded based on the corresponding tested integral length scale and presented in Fig. 5.10(d). As evident in the inset of the figure, $(N_{\mathrm{OH}}/N_{\overline{\mathrm{OH}}})^{-1}$ does not change by changing the integral length scale at relatively small values of $u'/S_{\mathrm{L},0}$. However, at relatively large values of the turbulence intensity, decreasing the integral length scale increases the values of $(N_{\mathrm{OH}}/N_{\overline{\mathrm{OH}}})^{-1}$ (compare the values of this parameters at $u'/S_{\mathrm{L},0} \approx 20$ and at different integral length scales). At relatively small turbulence intensities, the turbulent eddies cannot penetrate into the flame zone, extinctions rarely occur, and the values of $(N_{\mathrm{OH}}/N_{\overline{\mathrm{OH}}})^{-1}$ are relatively small and nearly independent of the tested integral length scales. However, at larger values of $u'/S_{\mathrm{L},0}$, eddies feature relatively large rotational kinetic energy and can penetrate into the flame zone (see Section 4.3). Thus, for the large values of $u'/S_{\mathrm{L},0}$, decreasing the integral length scale facilitates penetration of relatively small scale eddies into the flame zone, increasing the occurrence of extinctions, and as a result the larger values of $(N_{\mathrm{OH}}/N_{\overline{\mathrm{OH}}})^{-1}$ and D shown in Figs. 5.10 and 5.9(c). In essence, the above argument suggests that both $(N_{\mathrm{OH}}/N_{\overline{\mathrm{OH}}})^{-1}$ and D should be positively (negatively) correlated with $u'/S_{\mathrm{L},0}$ (Λ). To investigate this, variations of $(N_{\mathrm{OH}}/N_{\overline{\mathrm{OH}}})^{-1}$ and D versus $(u'/S_{\mathrm{L},0})(\Lambda/\delta_{\mathrm{L}})^{-1}$ (which is the inverse of the Damköhler number) are presented in Figs. 5.12(a) and (b), respectively. These figures suggest that $(N_{\mathrm{OH}}/N_{\overline{\mathrm{OH}}})^{-1}$ and D data collapse when they are plotted versus Da^{-1}. Using the least-square technique, third and second order polynomial curves were fit to the variation of $(N_{\mathrm{OH}}/N_{\overline{\mathrm{OH}}})^{-1}$ and D versus Da^{-1}, respectively, and it is obtained that

$$(N_{\mathrm{OH}}/N_{\overline{\mathrm{OH}}})^{-1} \approx 0.35Da^{-3} - 0.79Da^{-2} + 0.83Da^{-1} + 1. \tag{5.11}$$

$$D \approx 3.1Da^{-2} + 3.5Da^{-1}. \tag{5.12}$$

Combining Eqs. (5.10) and (5.12), it can be shown that the normalized heat release rate

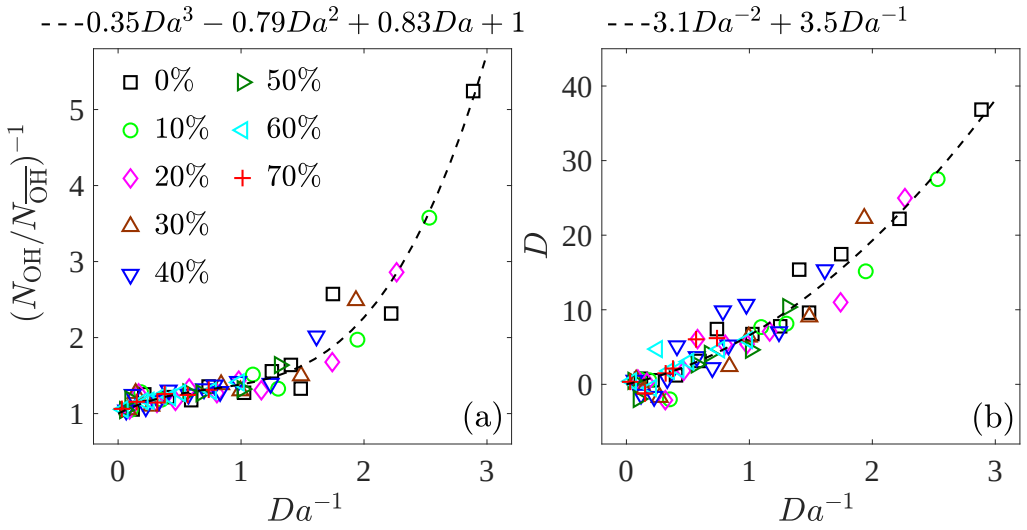

Fig. 5.12. Variations of (a) $(N_{OH}/N_{\overline{OH}})^{-1}$ and (b) D with Da^{-1}.

marker is obtained from

$$\frac{\mathcal{M}_T}{\mathcal{M}_L} \approx \underbrace{\left(1 + \frac{u'}{S_{L,0}}\right)}_{\text{Term I}} \underbrace{-3.1Da^{-2} - 3.5Da^{-1}}_{\text{Term II}}. \tag{5.13}$$

In Eq. (5.13), Term I is the prediction of the Damköhler's first hypothesis (see Eq. (1.24)), and Term II highlights the negative contribution of the bending behavior to the normalized heat release rate marker of the tested turbulent premixed flames. This correction to the Damköhler's formulation is the contribution of this chapter to the existing literature in combustion science.

To assess prediction of Eq. (5.13), first, values of the normalized heat release rate marker color-coded based on the normalized integral length scale (Λ/δ_L) are presented in Fig. 5.13(a). Then, the values of $\mathcal{M}_T/\mathcal{M}_L$ obtained from Eq. (5.13) are overlaid on the figure for several values of Λ/δ_L by the dotted-dashed curves. The prediction of Damköhler [18] is also shown by the black dashed line. The results in Fig. 5.13(a) suggest that the formulation proposed in Eq. (5.13) allows for prediction of the normalized heat release rate marker. The results also show that, flames with larger Λ/δ_L feature less pronounced bending behavior; and, at a fixed value of $u'/S_{L,0}$, increasing Λ/δ_L increases $\mathcal{M}_T/\mathcal{M}_L$. In fact, at the limit

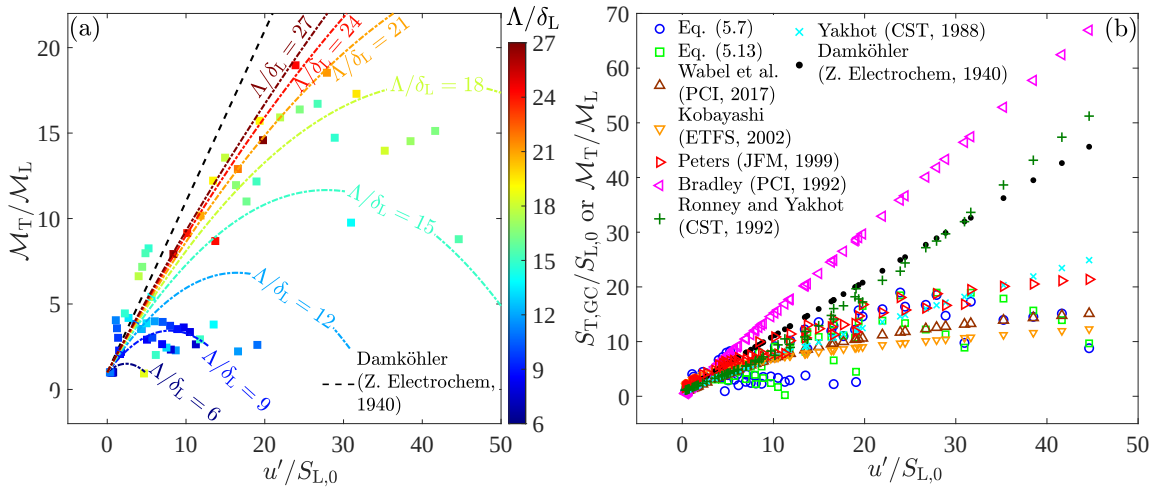

Fig. 5.13. (a) Comparison between the predictions of Eqs. (5.7) and (5.13) proposed in the present study. (b) Comparisons between the predictions of Eqs. (5.7) and (5.13) with the normalized global consumption speed obtained from the models proposed in [11, 13–18].

of Λ/δ_L approaching infinity, Eq. (5.13) suggests that $\mathcal{M}_T/\mathcal{M}_L$ approaches the prediction of the Damköhler's first hypothesis shown by the dashed line in Fig. 5.13. Also, for a fixed value of Λ/δ_L, the variation of the normalized heat release rate marker versus $u'/S_{L,0}$ features a parabolic behavior. For extremely large values of $u'/S_{L,0}$, the effect of Term II in Eq. (5.13) becomes dominant, which is equivalent to pronounced occurrences of extinctions, leading to decrease of $\mathcal{M}_T/\mathcal{M}_L$.

The experimental results of the present study (obtained from Eq. (5.7)), prediction of Eq. (5.13), as well as the predictions of the normalized global consumption speed using models developed in past investigations [11, 13–18] (Eqs. (1.24), (1.25), (1.28), (1.29), (1.33), (1.34), and (1.35)) are presented in Fig. 5.13(b). For example, predictions of the model developed by Wabel et al. [11] were obtained using their formulation along with our turbulent flow characteristics and preheat zone thicknesses, and the results are shown by the brown triangular symbol in Fig. 5.13(b). The models developed by Wabel et al. [11] and Kobayashi [13] are empirical fits to their experimental results and the values estimated by these models are close to the values of $\mathcal{M}_T/\mathcal{M}_L$ obtained in this study, especially at large integral length scales. The rest of the models [14–18] are obtained using theoretical arguments. These models [14–18] have not considered the flame quench/extinction and the

non-flamelet behavior, which can significantly influence the global consumption speed/heat release rate marker, especially at large turbulence intensities, hence the large difference observed between the predictions of the present study along with Kobayashi [13] and Wabel et al. [11] with those from [14–18].

The bending behavior shown in Fig. 5.13 and decrease of the heat release rate marker due to extinctions are consistent with the results of past studies, see for example [15, 41, 104, 105]. The implication of Eq. (5.13) and the results presented in Fig. 5.13 is that the heat release rate marker cannot increase indefinitely with increasing the turbulence intensity. However, at very large normalized integral length scales, the amount of bending (or decrease of the burning velocity) is less pronounced. This conclusion is of relevance to DNS studies. Compared to experimental investigations, the DNS studies tend to utilize a relatively small domain of investigation and as a result a relatively small integral length scale, see for example studies of [83, 84, 98, 99]. Our results suggest, increasing the size of the domain of investigation and the integral length scale could potentially allow for the DNS investigations to capture relatively larger values of their burning rate.

Chapter 6

Lack back-support effects on the flame structure and burning velocity

Relatively large background turbulence intensities can lead to flame extinction events, surrounding air entrainment, and as a result reactants dilution, which can change the flame structure and the burning velocity. Although some past investigations, see for example [8, 11, 55, 118, 121], considered mitigating the reactants dilution using a large pilot flame (referred to as back-support), several other investigations did not utilize a back-support or their back-support could not surround the entire flame, see for example [36]. It was hypothesized in Chapters 4 and 5 that air entrainment and flame extinction as a result of the lack of back-support may influence the flame structure (preheat and reaction zone thicknesses as well as the non-flamelet behavior) and the burning velocity (heat release rate marker). Studying this hypothesis is challenging since the flame extinction, itself, is usually influenced by varying background turbulent flow characteristics in past studies. The objective of this chapter is to investigate the influences of lack of back-support on both the flame structure and the burning velocity by keeping the background turbulence unchanged.

Aiming to study the effect of the co-flow on the relevant tested co-flow turbulent flames, the preheat (δ_{P}) and reaction (δ_{F}) zone thicknesses, the non-flamelet behavior ($\mathcal{N}\%$), the normalized local consumption speed ($S_{\mathrm{T,LC}}/S_{\mathrm{L},0}$, see Eq. (5.1)), and the normalized heat

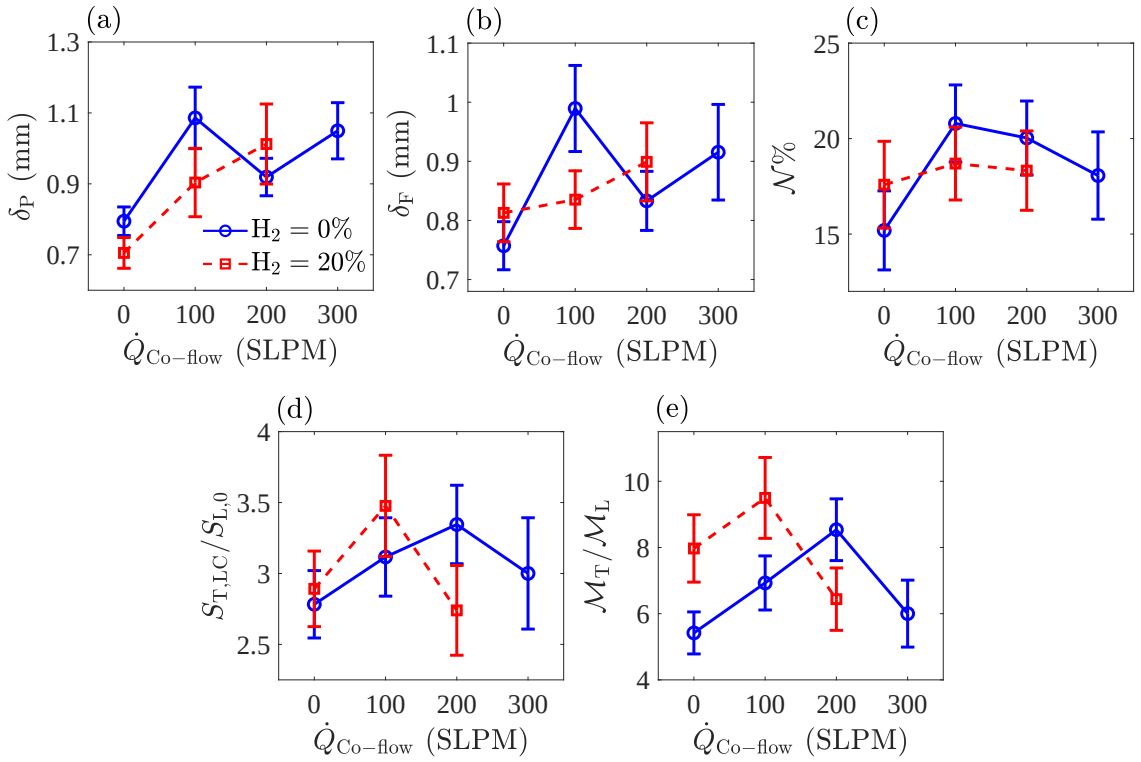

Fig. 6.1. Variations of (a) the mean preheat zone thickness, (b) the reaction zone thickness, (c) the non-flamelet parameter, (d) the normalized local consumption speed, and (e) the normalized heat release rate marker with the flow rate of the co-flow.

release rate marker ($\mathcal{M}_T/\mathcal{M}_L$) are estimated and presented in Fig. 6.1(a–d), respectively. The values of δ_P and δ_F were estimated following the procedures discussed in Chapter 3. $\mathcal{N}\%$ relates to the deviation of the OH and formaldehyde PLIF data from those synthetically generated from a laminar flame simulation (see Chapter 4). As discussed in Chapter 5, $\mathcal{M}_T/\mathcal{M}_L$ equals the integral over the domain of investigation of the heat release rate estimated from Eq. (5.7) and is a newly proposed parameter for estimation of how fast turbulent premixed flames burn. The lengths of the error bars in Fig. 6.1 are equal to the standard deviations (over 500 frames) of the corresponding parameters. The results in Fig. 6.1 show that, increasing $\dot{Q}_{Co-flow}$ may increase or decrease the above parameters, and a trend cannot be obtained. The underlying pathways that would allow understanding the effects of co-flow on the flame structure and the burning velocity are schematically presented in Fig. 6.2. As demonstrated in the figure, co-flow (top left corner) and background turbulence (bottom right corner) are the speculated root-cause of changes in the above parameters. The latter is

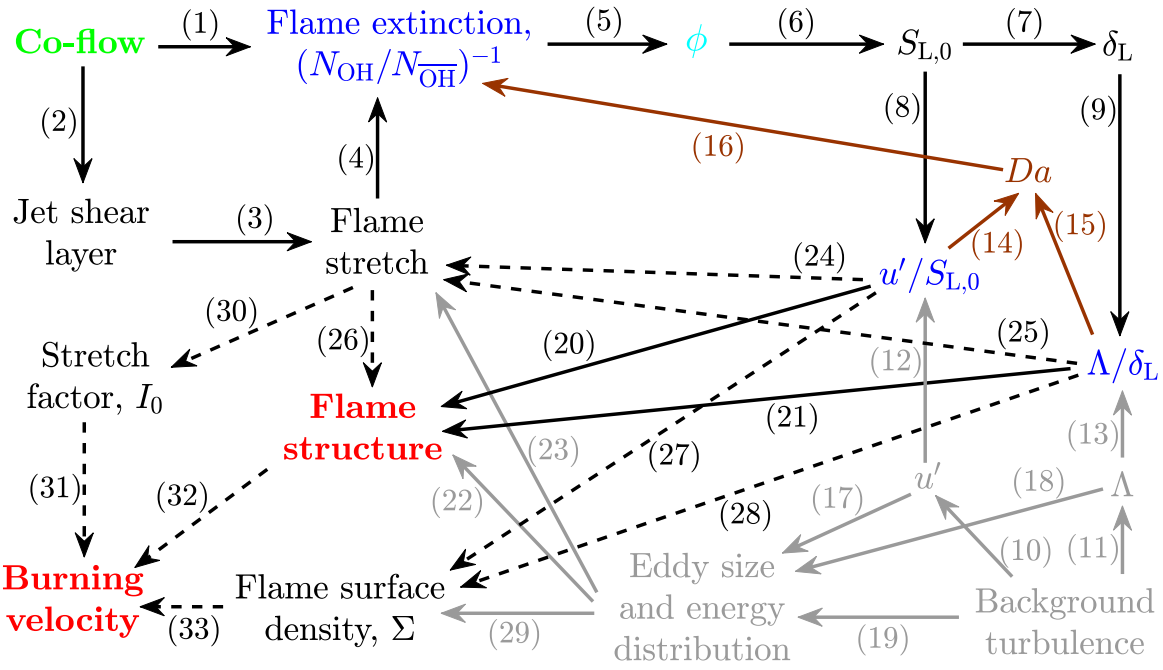

Fig. 6.2. Schematic diagram presenting the possible pathways that the co-flow and the background turbulence intensity can influence both the flame structure and burning velocity.

unchanged in the present study, and the corresponding pathways rooted in the background turbulence (shown by the gray color) do not influence the flame structure and the burning velocity in the present investigation.

In Fig. 6.2, the co-flow leads to the entrainment of cold air and as a result the flame extinctions (see process (1) in Fig. 6.2). Similarly, adding the co-flow can alter the jet shear layer dynamics (see process (2)), which can influence the flame stretch (process (3)), and lead to a pronounced amount of flame extinction (process (4)). Occurrence of local extinctions as the co-flow is added is visualized in Figs. 6.3 and 6.4 for 0 and 20% of H_2%, respectively. In these figures, the first to fourth columns pertain to the flow rate of the co-flow increasing from 0 to 300 SLPM in increments of 100 SLPM, while the rest of the tested parameters are unchanged. Please note that, as discussed in Chapter 2, data is not available for 300 SLPM of $H_2 = 20\%$ and as a result, Fig. 6.4 has only three columns. The first, second, and third rows of the figures present representative OH and CH_2O PLIF as well as the corresponding heat release rate marker (I_{HRR}) images, respectively. In the last rows of Figs. 6.3 and 6.4,

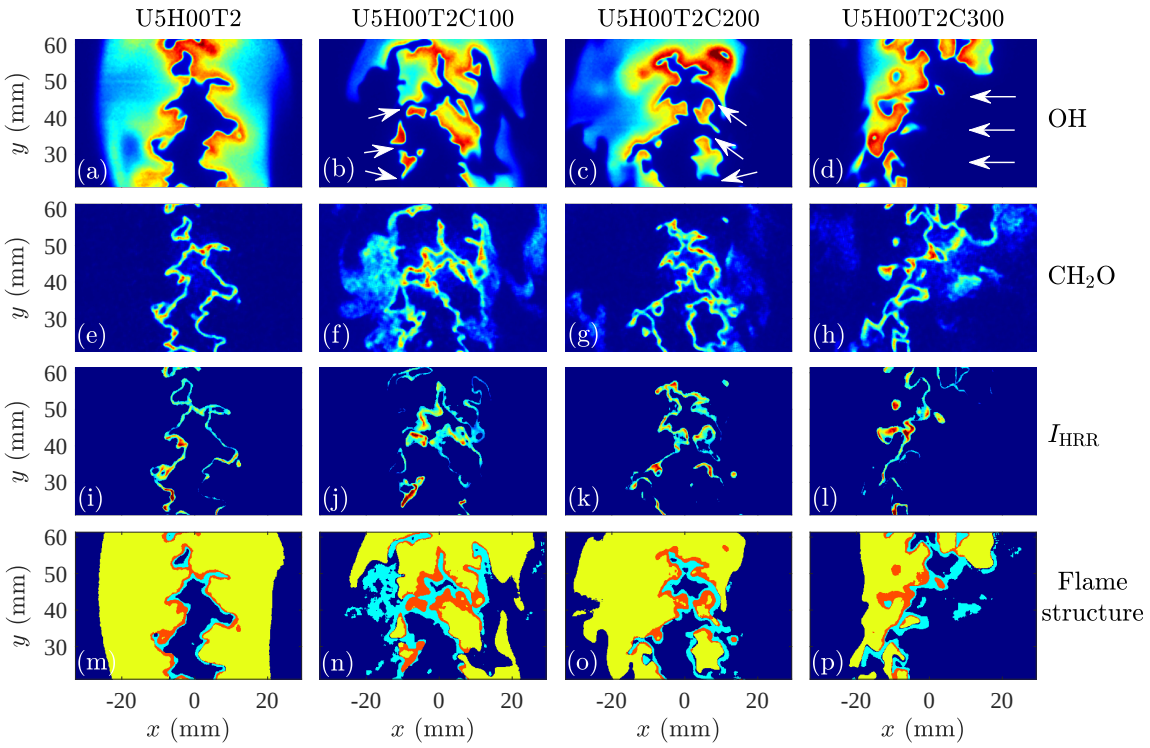

Fig. 6.3. OH (first row) and CH_2O (second row) PLIF images, I_{HRR} (third row), and flame structure (fourth row) for representative frames of U5H00T2 (first column), U5H00T2C100 (second column), U5H00T2C200 (third column), and U5H00T2C300 (fourth column). In (b–d), the white arrows highlight the representative regions where flame extinction event and air entrainment occur. In (m–p), the cyan, red, and yellow regions present the preheat, reaction, and combustion products zones, respectively.

the flame structures are visualized using the cyan, red, and yellow colors, which correspond to the preheat, reaction, and combustion products zones, respectively. As can be seen in Figs. 6.3 and 6.4, for $\dot{Q}_{\text{Co-flow}} = 0$ (test conditions of U5H00T2 and U5H20T2), the pilot and the combustion products surround the reaction zone. However, with adding the co-flow (lack of back-support), the surrounding cold air dilutes the combustion products, interacts with the reaction zone, and flame extinctions take place. Representative locations where flame extinction events and air entrainment occur are highlighted by the white arrows in the first rows of Figs. 6.3 and 6.4.

As discussed in Chapter 5, OH PLIF signal can be used to study flame extinction events. Similar to Chapter 5, the flame extinction is quantified using the normalized area of the pixels with significant OH PLIF data (compared to the time averaged OH PLIF data), which

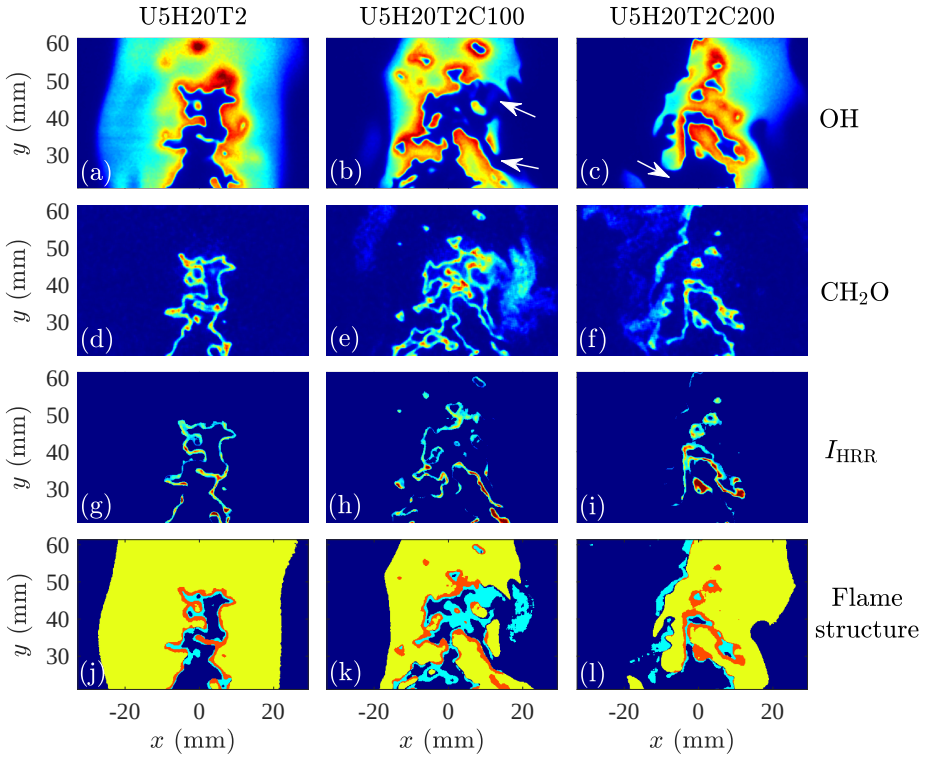

Fig. 6.4. OH (first row) and CH_2O (second row) PLIF images, I_{HRR} (third row), and flame structure (fourth row) for representative frames of U5H20T2 (first column), U5H20T2C100 (second column), and U5H20T2C200 (third column). In (b and c), the white arrows highlight the representative regions where flame extinction event and air entrainment occur. In (j–l), the cyan, red, and yellow regions present the preheat, reaction, and combustion products zones, respectively.

is referred to as $(N_{OH}/N_{\overline{OH}})^{-1}$. This parameter was calculated for each frame of all co-flow relevant tested conditions, with the corresponding mean values presented in Fig. 6.5. The error bar length in the figure is the standard deviation of $(N_{OH}/N_{\overline{OH}})^{-1}$. As can be seen, increasing $\dot{Q}_{Co-flow}$ from 0 to 300 SLPM increases $(N_{OH}/N_{\overline{OH}})^{-1}$ from about 1 to 3.3. The results presented in Fig. 6.5 allows for quantifying processes (1–4) in Fig. 6.2 and confirm the observations made in Figs. 6.3 and 6.4 also statistically hold.

Following the diagram shown in Fig. 6.2, flame extinction is the root-cause of several pathways that lead to alteration of the flame structure and the burning velocity. Thus, for all the co-flow relevant tested conditions, the mean and instantaneous (estimated for each frame) values of δ_P, δ_F, $\mathcal{N}\%$, $S_{T,LC}/S_{L,0}$, and $\mathcal{M}_T/\mathcal{M}_L$ versus $(N_{OH}/N_{\overline{OH}})^{-1}$ are obtained and presented in Figs. 6.6 and 6.7, respectively. The lengths of the horizontal and vertical

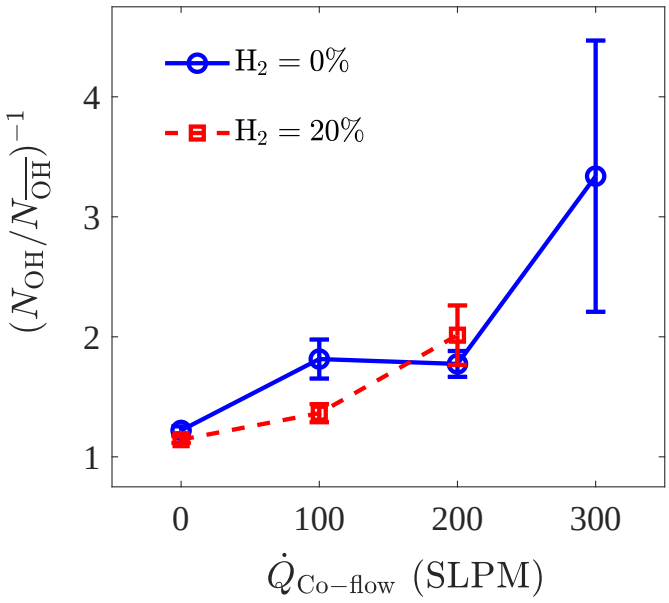

Fig. 6.5. Mean $(N_{OH}/N_{\overline{OH}})^{-1}$ versus $\dot{Q}_{Co-flow}$.

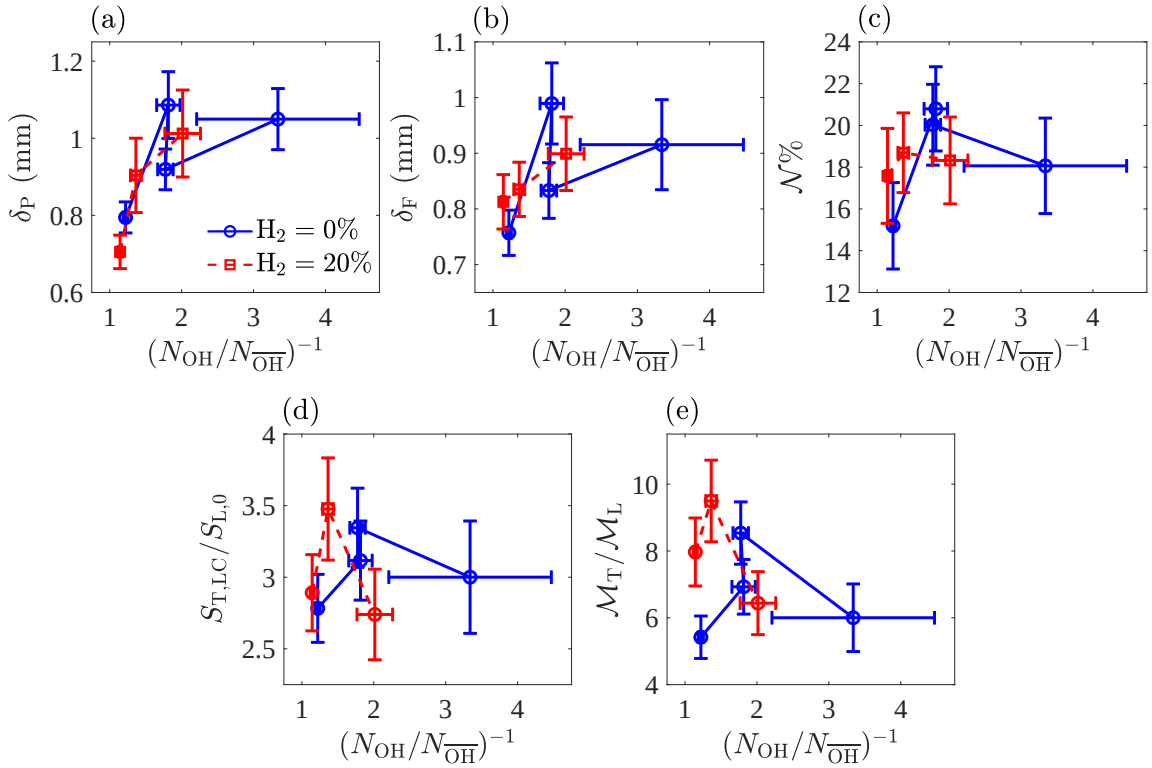

Fig. 6.6. Variations of the mean (a) preheat and (b) reaction zone thicknesses, (c) the mean non-flamelet behavior, (d) the normalized local consumption speed, and (e) the normalized heat release rate marker versus $(N_{OH}/N_{\overline{OH}})^{-1}$.

error bars in Fig. 6.6 equal the standard deviation of the data pertaining to the parameters presented along the horizontal and vertical axes. The trends of variations are also presented

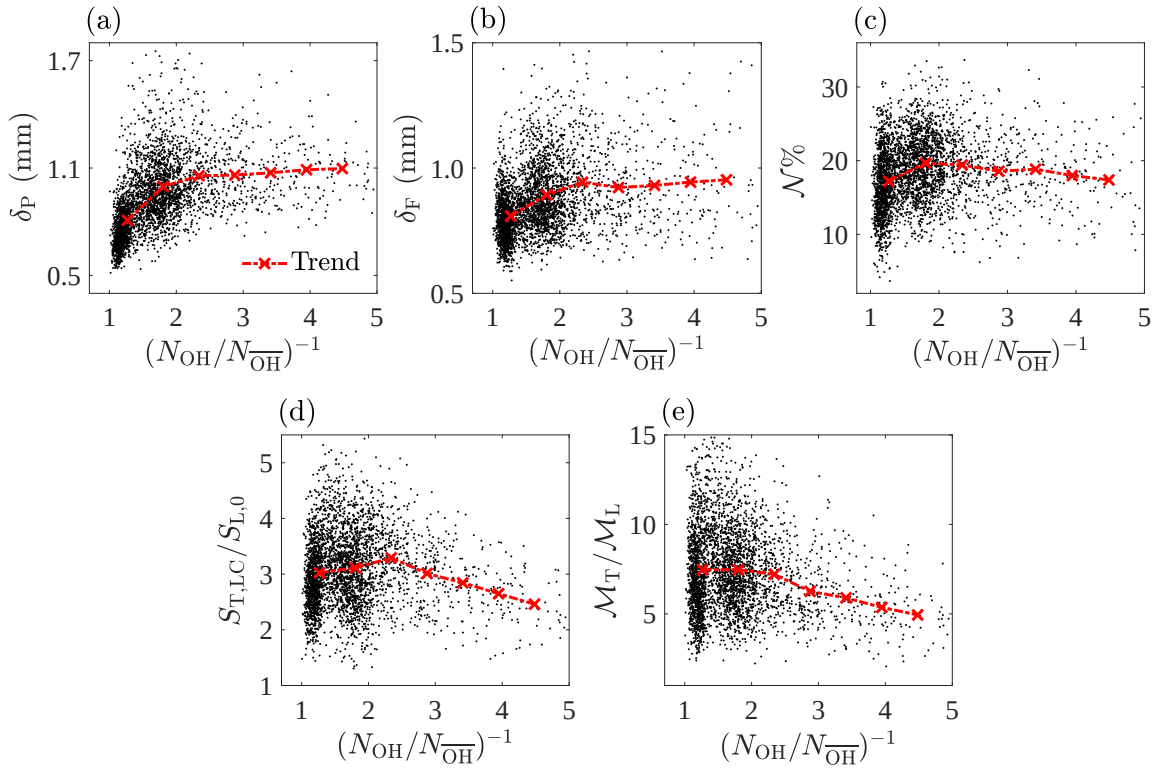

Fig. 6.7. Instantaneous variations of (a) the preheat and (b) reaction zone thicknesses, (c) the non-flamelet behavior, (d) the normalized local consumption speed, and (e) the normalized heat release rate marker versus $(N_{OH}/N_{\overline{OH}})^{-1}$.

in Fig. 6.7 by the red cross data symbol and red doted-dashed lines. These trends were obtained by dividing the data pertaining to the parameter associated with the horizontal axis, $(N_{OH}/N_{\overline{OH}})^{-1}$, into 7 bins and calculating the mean of δ_P, δ_F, $\mathcal{N}\%$, $S_{T,LC}/S_{L,0}$, and $\mathcal{M}_T/\mathcal{M}_L$ for each bin. As can be seen in Figs. 6.6 and 6.7, changing $(N_{OH}/N_{\overline{OH}})^{-1}$ can alter δ_P, δ_F, $\mathcal{N}\%$, $S_{T,LC}/S_{L,0}$, and $\mathcal{M}_T/\mathcal{M}_L$. The reason for these changes is elaborated in the following using the relevant processes/pathways presented in Fig. 6.2.

As schematically demonstrated in Fig. 6.2, the local extinction events (quantified by $(N_{OH}/N_{\overline{OH}})^{-1}$) lead to dilution of the reactants (due to air entrainment), and as a result reduction of the fuel-air equivalence ratio [49, 125] (see process (5) in Fig. 6.2). The fuel-air equivalence ratio spatial distribution is not measured in the present study. However, an alternative method is utilized to estimate an effective fuel-air equivalence ratio (ϕ_{eff}). The results presented in Chapter 5 suggest there exits a unique relation between Da^{-1} and

$(N_{OH}/N_{\overline{OH}})^{-1}$ for a relatively large number of tested conditions without co-flow, which is given by $(N_{OH}/N_{\overline{OH}})^{-1} \approx 0.35Da^{-3} - 0.79Da^{-2}$, see Eq. 5.11. This equation relates the input and output of process (16) in Fig. 6.2. In this equation, Da is estimated based on the set value of the fuel-air equivalence ratio, which is 0.7. However, once reactants dilution occurs (due to air entrainment), the effective fuel-air equivalence ratio (ϕ_{eff}) decreases, and as a result, the effective Damköhler number (Da_{eff}) changes. The relation between these parameters is given by

$$Da_{eff} = (\Lambda/u')\frac{S_{L,0}(\phi_{eff})}{\delta_L(\phi_{eff})}. \tag{6.1}$$

Since the background turbulent flow is unchanged in the present study, Λ/u' in Eq. (6.1) is fixed, and ϕ_{eff} can be estimated provided Da_{eff} is known. The values of the effective Damköhler number were obtained using the experimentally measured $(N_{OH}/N_{\overline{OH}})^{-1}$ along with Eq. (5.11) for each frame and for all co-flow relevant tested conditions. Finally, for each tested H_2% in the present study, Cantera [50] simulations of a freely propagating laminar premixed flame for several values of ϕ_{eff} was performed, the corresponding $S_{L,0}(\phi_{eff})$ and $\delta_L(\phi_{eff})$ were obtained, and the value of ϕ_{eff} that leads to the estimated Da_{eff} was calculated for each collected OH PLIF image and for all co-flow relevant tested conditions. The mean values of ϕ_{eff} versus $(N_{OH}/N_{\overline{OH}})^{-1}$ are presented in Fig. 6.8. The lengths of the vertical and horizontal error bars in this figure are the standard deviations of ϕ_{eff} and $(N_{OH}/N_{\overline{OH}})^{-1}$, respectively. The corresponding mean effective laminar flames speeds ($S_{L,0,eff}$) and thicknesses ($\delta_{L,eff}$) are shown in Figs. 6.9(a) and (b), respectively. In these figures, the lengths of horizontal and vertical error bars are the standard deviations of data presented along the corresponding axes. The results in Figs. 6.5 and 6.8 show that increasing the flow-rate of the co-flow from 0 to 300 SLPM increases $(N_{OH}/N_{\overline{OH}})^{-1}$ from about 1 to 3.3, which decreases the effective fuel-air equivalence ratio from about 0.75 to 0.55. The fuel-air equivalence ratio at the Lower Flammability Limit (LFL) of 100% methane/air and

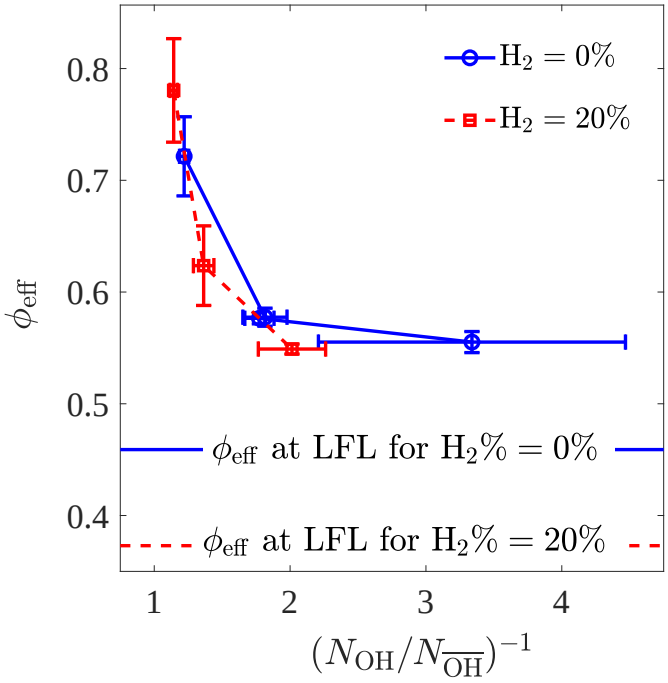

Fig. 6.8. Variation of the effective fuel-air equivalence ratio versus $(N_{\text{OH}}/N_{\overline{\text{OH}}})^{-1}$. The lower flammability limits are extracted for bomb experiments of [19].

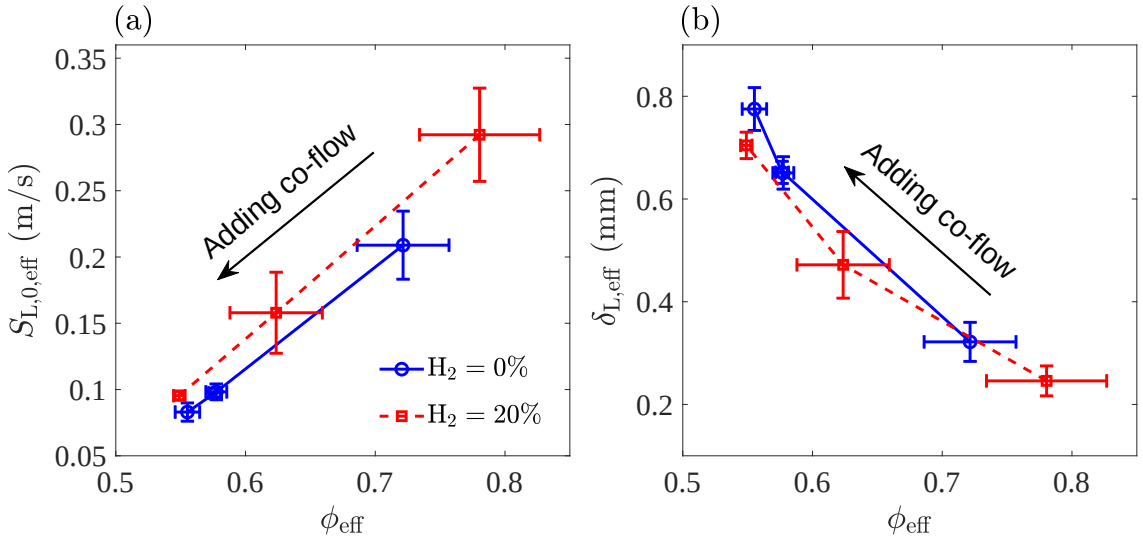

Fig. 6.9. The mean values of (a) $S_{\text{L,0,eff}}$ and (b) $\delta_{\text{L,eff}}$ for the co-flow relevant conditions.

80% methane/ and 20% hydrogen/air mixtures were extracted for the bomb experiments of [19] and presented in Fig. 6.8 for comparison purposes.

The combined effects of the background turbulence and combustion chemistry on the flame structure and burning velocity are studied using either the flamelet assumption [5, 34] or flame thickening models (see Chapter 5). The former and the latter influence the flame

structure and the burning velocity through processes (24–28, 30, 31, and 33) as well as (20, 21, and 32) in Fig. 6.2, respectively. It is acknowledged that both the flame structure and the burning velocity can be influenced by the flame stretch. Here, it is assumed and later verified that the effects of the flame stretch on the flame structure and the burning velocity are not of leading importance. Thus, the diagram shown in Fig. 6.2 suggests that, provided the background turbulence is unchanged, and the relations between the flame extinctions, the effective fuel-air equivalence ratio, and the effective Damköhker number are known, the influences of the co-flow on the flame structure and burning velocity can be elaborated using $u'/S_{\mathrm{L,0,eff}}$ and $\Lambda/\delta_{\mathrm{L,eff}}$.

For all collected images and co-flow relevant tested conditions, the instantaneous values of δ_{P}, δ_{F}, $\mathcal{N}\%$, $S_{\mathrm{T,LC}}/S_{\mathrm{L,0}}$, and $\mathcal{M}_{\mathrm{T}}/\mathcal{M}_{\mathrm{L}}$ are presented against instantaneous $u'/S_{\mathrm{L,0,eff}}$ in Fig. 6.10(a–d), respectively. The results are color-coded based on the instantaneous values of $\Lambda/\delta_{\mathrm{L,eff}}$. The corresponding trends were obtained by dividing the horizon axis ($u'/S_{\mathrm{L,0,eff}}$) into 7 bins and calculating the mean value of the data (δ_{P}, δ_{F}, $\mathcal{N}\%$, $S_{\mathrm{T,LC}}/S_{\mathrm{L,0}}$, and $\mathcal{M}_{\mathrm{T}}/\mathcal{M}_{\mathrm{L}}$) for the bins. These trends are presented on the figure by the red cross data symbols. Also overlaid on the figure are the corresponding mean values of δ_{P}, δ_{F}, $\mathcal{N}\%$, $S_{\mathrm{T,LC}}/S_{\mathrm{L,0}}$, and $\mathcal{M}_{\mathrm{T}}/\mathcal{M}_{\mathrm{L}}$ from the results in Chapters 4 and 5 pertaining to the conditions with the identical setup configuration (two perforated plates). Please note, for the results of Chapters 4 and 5, $S_{\mathrm{L,0,eff}} = S_{\mathrm{L,0}}$ and $\delta_{\mathrm{L,eff}} = \delta_{\mathrm{L}}$ since negligible extinction is observed for $u'/S_{\mathrm{L,0}} \lesssim 15$, see Fig. 5.10(c). The values of $u'/S_{\mathrm{L,0,eff}}$ evaluated at ϕ_{eff} corresponding to LFL of $H_2 = 0\%$ and 20% are estimated using Cantera [50] and equal 36.5 and 134.1, respectively. Similarly, the values $\Lambda/\delta_{\mathrm{L,eff}}$ at ϕ_{eff} corresponding to LFL of $H_2 = 0\%$ and 20% are estimated and equal 2.1 and 0.6, respectively. For the fixed background turbulence of the present study, the above values are the largest and smallest turbulence intensity and normalized integral length scales that the flames could possibly experience due to the reactants dilution. The results in Fig. 6.10(a) show that increasing $u'/S_{\mathrm{L,0,eff}}$ and decreasing

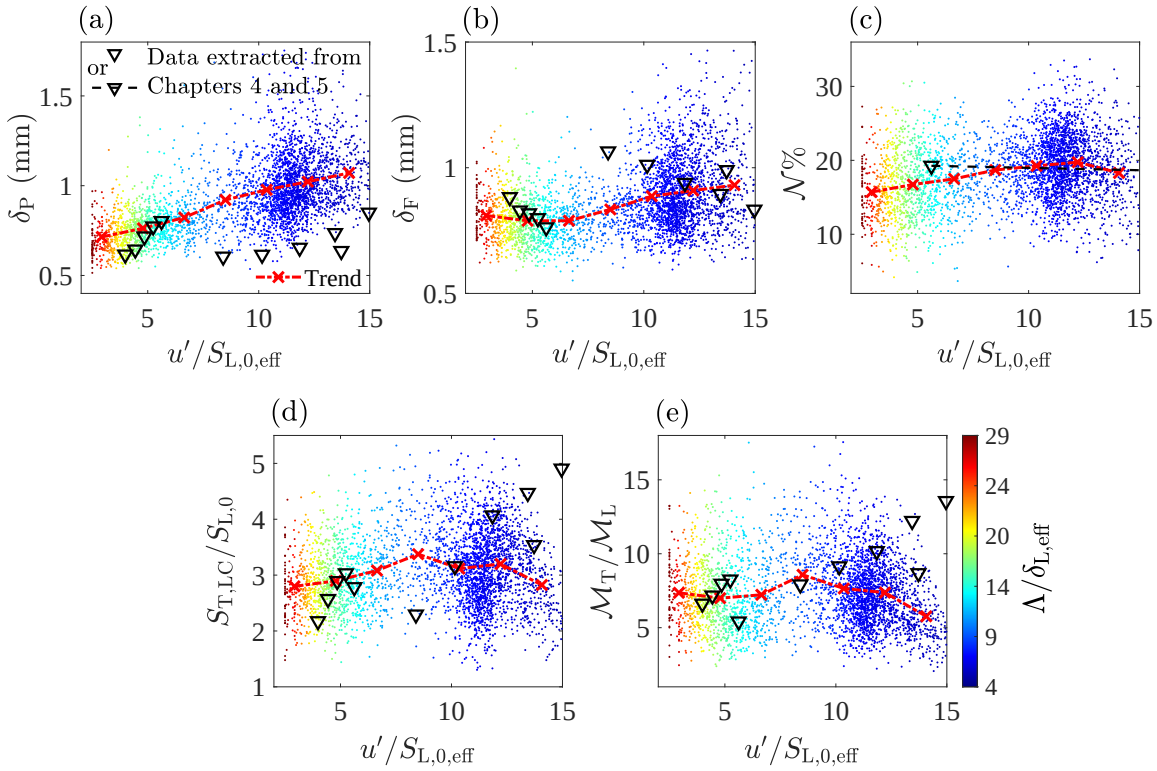

Fig. 6.10. Variations of (a) the preheat zone thickness, (b) the reaction zone thickness, (c) the non-flamelet behavior, (d) the normalized local consumption speed, and (e) the normalized heat release rate marker versus $u'/S_{L,0,eff}$. The red data points are the trends and the black data points are those extracted from Chapters 4 and 5 for the flames without the co-flow and with two perforated flames.

$\Lambda/\delta_{L,eff}$ increases δ_P. The values of the overall effective Lewis number (the effective Lewis number calculated at ϕ_{eff}) were estimated following [3]. It was shown that the values of the overall effective Lewis number changes from 0.95 to 1.06 for the co-flow relevant conditions. Since $Le_{eff} \approx 1$, the effect of curvature on the flame stretch is not pronounced on an averaged basis, but flame strain could influence the flame structure and the burning velocity. The increasing trend presented in Fig. 6.10(a), however, suggests that the flame thickening, with influencing pathways shown by processes (20, 21, and 32) in Fig. 6.2, plays a leading role compared to the flame thinning (due to strain), with the influencing pathways shown by processes (24–26, 30, and 31) for the co-flow relevant tested conditions.

Comparison of the results in Fig. 6.10(a) and those of Chapter 4 suggests that for $\Lambda/\delta_{L,eff} \gtrsim 14$, the data collapse. This is because such large normalized effective integral length scales pertain to $\dot{Q}_{Co-flow} \approx 0$ in the this chapter and that of Chapter 4. However,

adding the co-flow decreases ϕ_{eff} and increases $\delta_{\text{L,eff}}$, decreasing $\Lambda/\delta_{\text{L,eff}}$. Since the background turbulence is unchanged, the large values of $\delta_{\text{L,eff}}$ accommodate the turbulent eddies to reside inside the flame region; and, as a result, the relatively large values of δ_{P} reported in this chapter compared to those in Chapter 4. In comparison with the preheat zone thickness, the variations of the reaction zone thickness and $\mathcal{N}\%$ versus $u'/S_{\text{L,0,eff}}$ feature a modest increase, and the trends are less sensitive to $\Lambda/\delta_{\text{L,eff}}$ (see Figs. 6.10(b) and (c)). It is speculated, for the relatively moderate turbulence intensities studied in this chapter ($u'/S_{\text{L,0,eff}} \lesssim 15$), the preheat zone serves as a buffer [119] and does not allow for penetration of turbulent eddies into the reaction zone, and as a result significant thickening of this zone. Thus, substantial deviation from the flamelet behavior is not observed. This observation also agrees with the representative flame structure presented in Figs. 6.3(m–p) and 6.4(j–l), see the relatively thin red regions.

As shown in [187, 188] and also Chapter 5, the normalized burning velocity (local and global consumption speeds as well as the heat release rate marker) is positively related to the normalized integral length scale. Thus, as Figs. 6.10(d) and (e) show, for $\Lambda/\delta_{\text{L,eff}} \gtrsim 14$ (which is related to $\dot{Q}_{\text{Co-flow}} \approx 0$), the values of the normalized local consumption speed and the normalized heat release rate marker presented in Chapter 5 can be reconciled. However, increasing $\dot{Q}_{\text{Co-flow}}$ increases the flame extinction events, increases $\delta_{\text{L,eff}}$, and decreases the normalized local consumption speed and the normalized heat release rate marker, see the decreasing trend in Figs. 6.10(d) and (e). Indeed, at the turbulence intensities and normalized integral length scales corresponding to LFL (reported above), $S_{\text{T,LC}}/S_{\text{L,0}} = 0$ and $\mathcal{M}_{\text{T}}/\mathcal{M}_{\text{L}} = 0$, hence the decreasing trend for $u'/S_{\text{L,0,eff}} \gtrsim 9$ in Figs. 6.10(d) and (e) is expected. In essence, for the co-flow relevant tested conditions discussed in this chapter, adding the co-flow leads to flame extinction, reduces the effective fuel-air equivalence ratio, broadens the preheat zone, does not influence the reaction zone and the non-flamelet parameter significantly, and eventually decreases the normalized burning velocity.

Chapter 7

Conclusions

7.1 Concluding remarks

The internal structure and burning velocity of extremely turbulent hydrogen-enriched methane-air premixed flames were investigated using planar laser-induced fluorescence of OH and CH_2O as well as stereoscopic particle image velocimetry techniques. A Bunsen burner with an exit diameter of 22.2 mm was utilized in the experiments. The fuel-air equivalence ratio was set to 0.7 for all tested conditions, and volume-based hydrogen-enrichment percentage was varied from 0% to 70% with steps of 10%. Four mean bulk flow velocities of 5, 15, 25, and 35 m/s were examined. Three turbulence generating mechanisms corresponding to none, one, or two perforated plates were utilized. The turbulence intensity ($u'/S_{L,0}$) of the tested conditions varied from 0.3 to 44.6, leading to Reynolds and Karlovitz numbers ranging from 18 to 2729 and 0.1 to 76.0, respectively. In addition to these, five conditions were tested using a co-flow setup with the corresponding flow rates of 100, 200, and 300 SLPM to mimic the lack of back-support and explore the effect of air entrainment and flame extinction on the premixed flames internal structure and burning velocity. For these conditions, the mean bulk flow velocity and streamwise velocity fluctuations root mean square were 5 m/s and 1.10 m/s, respectively. Also, the volume-based tested hydrogen-enrichment percentage was set to either 0% or 20%.

Using freely propagating laminar flame simulations, a method was proposed to more accurately track the heat release rate of the hydrogen-enriched methane-air flames to be

able to locate the preheat and reaction zones of these flames and estimate their thicknesses. Then, utilizing this method, the preheat and reaction zone thicknesses were measured for the tested premixed flames. It was shown that, at large turbulence intensities, both the preheat and reaction zones feature broadening, and their thickness can increase up to 6.3 and 4.9 times those of the laminar flame counterparts, respectively. The results showed that, for a given RMS velocity fluctuations (u'), increasing the hydrogen-enrichment percentage decreases the preheat zone thickness. However, a monotonic behavior was not observed for the effect of hydrogen enrichment on the reaction zone thickness. While broadening of the preheat and reaction zones at large turbulence intensities have been reported in the literature for methane-air flames, broadening of these zones for extremely turbulent hydrogen-enriched methane-air premixed flames was reported in this thesis for the first time. Also, a framework was developed to quantify the deviation of the premixed flames from the flamelet behavior, referred to as the non-flamelet behavior ($\mathcal{N}\%$). This was quantified for the methane-air flames and it was shown that the increase of non-flamelet behavior is accompanied by broadening of the reaction zone.

The local turbulent flow characteristics and their relations with the flame internal structure were also investigated for the methane-air premixed flames. The value of the swirling strength (Q) was estimated for these flames inside both the reactants and preheat zones. It was shown that Q is correlated with the preheat and reaction zone thicknesses. Specifically, increasing $u'/S_{L,0}$ from 0.8 to 44.6 increases Q (estimated inside both reactants and preheat zone) normalized by those for a nearly laminar flame (estimated inside the reactants) from about 1 to 8000. This means that increasing the turbulence intensity significantly increases the swirling strength inside both the reactants and the preheat zone. The effects of the utilized turbulence generating mechanisms on the distribution of the eddy sizes and their specific kinetic energy were also studied. The results suggest that different types of turbulence generating mechanisms lead to different distributions of the eddy size and energy.

These differences are important and are speculated to cause the controversial results related to the broadening of the reaction zone that are reported in the literature. The results show that, for highly turbulent premixed flames, there exists a large number of eddies with two-dimensionally-resolved sizes close to the Taylor length scale, which feature a relatively large specific kinetic energy. While it is experimentally shown these eddies enter the preheat zone, broadening of the reaction zone being due to the penetration of these eddies into this zone is speculated and remains to be investigated experimentally.

Broadening of the reaction zone observed for the premixed flames suggests that using the flamelet assumption may not lead to an accurate estimation of the burning velocity for these flames. A method that does not utilize the flamelet assumption was developed here and was used to estimate the burning velocity of the tested flames. In this method, a parameter was introduced for estimating the burning velocity and is referred to as the heat release rate marker. The values of the local consumption speed were also estimated for all tested conditions. The results showed that at a given RMS velocity fluctuations, increasing the hydrogen enrichment percentage increases the local consumption speed and the heat release rate marker. It was shown that for relatively small turbulence intensities, the value of the normalized (by that of the corresponding laminar flame) heat release rate marker follows that of the normalized local consumption speed. However, at larger turbulence intensities, the value of the normalized heat release rate marker followed the normalized global consumption speed values reported in the literature and they were significantly larger than the normalized local consumption speed. In fact, similar to past investigations, the results showed that increasing the turbulence intensity increases the ratio of the estimated values of the heat release rate marker/global consumption speed and the local consumption speed. Such disparity has been a matter of discussion in the literature. The results of this thesis show that the ratio of the normalized heat release rate marker and the normalized local consumption speed is positively correlated with both the preheat and reaction zone thick-

nesses, with the latter correlation being more pronounced. This implies that the flamelet assumption used for the calculation of the local consumption speed may be the reason for the difference between the values of the global and local consumption speeds reported in the literature. It was shown that, correcting the formulation of the local consumption speed by a non-dimensional factor that takes into account the reaction zone thickening, the difference between the heat release rate marker of the tested flames and the local consumption speed can be reconciled.

Similar to past investigations related to the normalized global consumption speed, the results showed that increasing the turbulence intensity does not linearly increase the normalized heat release rate marker, and this parameter features a bending behavior. First, the amount of bending in the variation of the normalized heat release rate marker versus the turbulence intensity was quantified. It was hypothesized and shown that the amount of bending is positively related to the occurrence of extinctions. For a given RMS velocity fluctuations, the bending behavior and occurrence of the extinctions were less pronounced for hydrogen-enriched flames. The results showed that both the amount of bending and the occurrence of the extinctions are related to the inverse of the Damköhlder number. Using this, a formulation that allows for quantifying the bending behavior and the heat release rate marker was developed. It was shown that the predictions of the proposed formulation follow those of past experimental investigations as well. The proposed formulation suggested that, at a given turbulence intensity, increasing the normalized integral length scale increases the normalized heat release rate marker approaching a limiting value predicted by the Damköhler's first hypothesis. At a fixed value of the integral length scale, the proposed formulation shows that increasing the turbulence intensity, first, increases the heat release rate marker. However, the proposed formulation (in agreement with past experimental results) predicted that further increasing the turbulence intensity decreases the heat release rate marker, which was hypothesized to be due to the pronounced occurrence of the ex-

tinctions. Although a positive relation between the occurrence of the extinctions and the bending behavior is reported in here, future investigations are required to study if there exists a causal relationship between these two parameters.

The effects of lack of back-support on the flame internal structure, non-flamelet behavior, and burning velocity were investigated using a co-flow setup. For fixed background turbulent flow conditions, it was shown that the lack of back-support leads to the flame extinctions, which influence the flame structure and the burning velocity. Specifically, the pronounced occurrence of the flame extinctions led to the increase of the preheat zone thickness. However, the reaction zone thickness and the non-flamelet parameter were less sensitive to the pronounced extinctions and remained nearly unchanged or featured a modest increase. The burning velocity, however, followed a decreasing trend with pronounced extinctions. The reduction of the effective fuel-air equivalence ratio due to reactants dilution (as a result of flame extinction and air entrainment) was argued to be the underlying reason for the above observations. Addition of the co-flow decreased the effective fuel-air equivalence ratio from 0.75 to 0.55. This increased the effective turbulence intensity from about 5 to 15 and decreased the effective normalized integral length scale from about 15 to 4. While the former can facilitate faster burning of the reactants, the latter decreases the burning rate. It was shown the effect of the latter on the normalized burning velocity is dominant. The results presented in this thesis demonstrate and elaborate the important role of the reactants dilution on the turbulent flame structure and burning velocity even at relatively moderate effective turbulence intensities.

7.2 Future directions

Although it was aimed in this thesis to partly address some of the ongoing research questions regarding the premixed flames, future investigations are required to support some of the findings of this dissertation, extend them to other studies, and also answer the re-

maining questions about the turbulent premixed flames. In the following, more details are provided regarding some of the suggested future investigations.

1. The model developed for the estimation of the heat release rate in hydrogen-enriched methane-air flames is based on the laminar flame simulations. Direct numerical simulation studies are required to confirm the accuracy of this model or improve it for larger turbulence intensities.

2. In this thesis, penetration of eddies into the preheat zone was demonstrated. However, their penetration into the reaction zone was speculated and not shown experimentally due to seed particle evaporation in the reaction zone and other issues with particle image velocimetry. Thus, future experimental efforts are required using solid seed particles combined with other measurement techniques to study the interaction between the reaction zone and turbulent flow structures and investigate the potential reasons for the broadening of the reaction zone.

3. It was shown in this dissertation that the turbulence generating mechanism has significant importance in the eddy size and energy distribution and it can potentially be the underlying reason for the conflicting reported results in the literature for the reaction zone broadening. However, future investigations are required to systematically study the effect of the turbulence generating mechanism and its influence on the quality of the interaction of eddies with the reaction zone.

4. To calculate the local consumption speed here and also some of the previous studies (see for example [11]), it was assumed that the flame stretch factor ($I_0 = S_L/S_{L,0}$) is equal to one. While there exist some studies (see for example [176]) showing the importance of using a proper stretch factor, future investigations are required to elaborate the effect of flame stretch factor and propose a framework for estimating it for different flame conditions.

5. The influence of back-support on the premixed flames structure and burning velocity is not well understood in the literature. The results in this thesis provide a first step towards understanding the influence of back-support on the premixed flames. However, they were limited to relatively small turbulence intensities. Further investigations are required to study the effect of this parameter on the flame structure and burning velocity at large turbulence intensities.

6. In this thesis, in the discussions related to the effect of lack of back-support on the premixed flames, the effective fuel-air equivalence ratio was estimated using the relation between flame extinction and the Damköhlder number. Simultaneous measurements of two-dimensional variations of the fuel-air equivalence ratio as well as the planar laser-induced fluorescence of OH and CH_2O was not performed. However, this will provide an improved understanding related to the effect of the back-support on the internal structure and burning velocity of the premixed flames. Integration of a Raman scattering technique with those used in this thesis is useful for understanding the effects of back-support, reactants dilution, and (even possibly) stratification on the flame structure and the burning velocity of turbulent flames.

7. In order to stabilize a Bunsen flame, usually, a pilot flame is utilized. In this dissertation and also some previous studies (see for example [8, 11, 36]), the influence of the pilot flame on the premixed flames structure and burning velocity was not considered. Future studies are required to investigate if the pilot flame plays a significant role on the results related to the structure and burning velocity of the premixed flames. Specifically, the effects chemistry of the mixture utilized for the pilot flame and its flow rate are required to be investigated in the future.

Bibliography

[1] S. Mohammadnejad, Q. An, P. Vena, S. Yun, S. Kheirkhah, Contributions of flame thickening and extinctions to a heat release rate marker of intensely turbulent premixed hydrogen-enriched methane-air flames, Combust. Flame 231 (2021) 111481.

[2] S. Mohammadnejad, Q. An, P. Vena, S. Yun, S. Kheirkhah, Thick reaction zones in non-flamelet turbulent premixed combustion, Combust. Flame 222 (2020) 285–304.

[3] S. Mohammadnejad, P. Vena, S. Yun, S. Kheirkhah, Internal structure of hydrogen-enriched methane–air turbulent premixed flames: Flamelet and non-flamelet behavior, Combust. Flame 208 (2019) 139–157.

[4] S. Mohammadnejad, Q. An, P. Vena, S. Yun, S. Kheirkhah, et al., Broadening of reaction zones in turbulent lean methane-air premixed flames, in: APS Division of Fluid Dynamics Meeting Abstracts, 2020, pp. G03–001.

[5] N. Peters, Turbulent combustion, Cambridge University Press, 2000.

[6] J. F. Driscoll, J. H. Chen, A. W. Skiba, C. D. Carter, E. R. Hawkes, H. Wang, Premixed flames subjected to extreme turbulence: Some questions and recent answers, Prog. Energy Combust. Sci. 76 (2020) 100802.

[7] C. Chi, G. Janiga, K. Zähringer, D. Thévenin, DNS study of the optimal heat release rate marker in premixed methane flames, Proc. Combust. Inst. 37 (2018) 2363–2371.

[8] A. W. Skiba, T. M. Wabel, C. D. Carter, S. D. Hammack, J. E. Temme, J. F. Driscoll,

Premixed flames subjected to extreme levels of turbulence part I: Flame structure and a new measured regime diagram, Combust. Flame 189 (2018) 407–432.

[9] G. V. Nivarti, R. S. Cant, S. Hochgreb, Reconciling turbulent burning velocity with flame surface area in small-scale turbulence, J. Fluid Mech. 858 (2019).

[10] Ö. L. Gülder, Contribution of small scale turbulence to burning velocity of flamelets in the thin reaction zone regime, Proc. Combust. Inst. 31 (2007) 1369–1375.

[11] T. M. Wabel, A. W. Skiba, J. F. Driscoll, Turbulent burning velocity measurements: Extended to extreme levels of turbulence, Proc. Combust. Inst. 36 (2017) 1801–1808.

[12] Z. Wang, B. Zhou, S. Yu, C. Brackmann, Z. Li, M. Richter, M. Aldén, X. S. Bai, Structure and burning velocity of turbulent premixed methane/air jet flames in thin-reaction zone and distributed reaction zone regimes, Proc. Combust. Inst. 37 (2019) 2537–2544.

[13] H. Kobayashi, Experimental study of high-pressure turbulent premixed flames, Exp. Therm. Fluid Sci. 26 (2002) 375–387.

[14] N. Peters, The turbulent burning velocity for large-scale and small-scale turbulence, J. Fluid Mech. 384 (1999) 107–132.

[15] D. Bradley, How fast can we burn?, Proc. Combust. Inst. 24 (1992) 247–262.

[16] P. D. Ronney, V. Yakhot, Flame broadening effects on premixed turbulent flame speed, Combust. Sci. Technol. 86 (1992) 31–43.

[17] V. Yakhot, Propagation velocity of premixed turbulent flames, Combust. Sci. Technol. 60 (1988) 191–214.

[18] G. Damköhler, Der einfluss der turbulenz auf die flammengeschwindigkeit in gasgemischen, Ber. Bunsen. Phys. Chem. 46 (1940) 601–626.

[19] F. Van den Schoor, R. T. E. Hermanns, J. A. Van Oijen, F. Verplaetsen, L. P. H. De Goey, Comparison and evaluation of methods for the determination of flammability limits, applied to methane/hydrogen/air mixtures, J. Hazard. Mater. 150 (2008) 573–581.

[20] M. P. Burke, M. Chaos, Y. Ju, F. L. Dryer, S. J. Klippenstein, Comprehensive H_2/O_2 kinetic model for high-pressure combustion, Int. J. Chem. Kinet. 44 (2012) 444–474.

[21] Z. Hong, D. F. Davidson, R. K. Hanson, An improved H_2/O_2 mechanism based on recent shock tube/laser absorption measurements, Combust. Flame 158 (2011) 633–644.

[22] A. Kéromnès, W. K. Metcalfe, K. A. Heufer, N. Donohoe, A. K. Das, C. J. Sung, J. Herzler, C. Naumann, P. Griebel, O. Mathieu, O. Mathieu, M. C. Krejci, E. L. Petersen, W. J. Pitz, H. J. Curran, An experimental and detailed chemical kinetic modeling study of hydrogen and syngas mixture oxidation at elevated pressures, Combust. Flame 160 (2013) 995–1011.

[23] A. L. Sánchez, F. A. Williams, Recent advances in understanding of flammability characteristics of hydrogen, Prog. Energy Combust. Sci. 41 (2014) 1–55.

[24] A. R. Masri, Challenges for turbulent combustion, Proc. Combust. Inst. 38 (2021) 121–155.

[25] R. W. Schefer, D. M. Wicksall, A. K. Agrawal, Combustion of hydrogen-enriched methane in a lean premixed swirl-stabilized burner, Proc. Combust. Inst. 29 (2002) 843–851.

[26] D. Cicoria, C. K. Chan, Effects of turbulence and strain rate on hydrogen-enriched high Karlovitz number lean premixed methane flames, Fuel 211 (2018) 754–766.

[27] E. R. Hawkes, J. H. Chen, Direct numerical simulation of hydrogen-enriched lean premixed methane–air flames, Combust. Flame 138 (2004) 242–258.

[28] F. E. Hernández-Pérez, C. P. Groth, Ö. L. Gülder, Large-eddy simulation of lean hydrogen–methane turbulent premixed flames in the methane-dominated regime, Int. J. Hydrog. Energy 39 (2014) 7147–7157.

[29] G. P. McTaggart-Cowan, S. N. Rogak, S. R. Munshi, P. G. Hill, W. K. Bushe, Combustion in a heavy-duty direct-injection engine using hydrogen—methane blend fuels, Int. J. Engine Res. 10 (2009) 1–13.

[30] G. P. McTaggart-Cowan, H. L. Jones, S. N. Rogak, W. K. Bushe, P. G. Hill, S. R. Munshi, Direct-injected hydrogen-methane mixtures in a heavy-duty compression ignition engine, SAE 2006-01-0653 (2006).

[31] J. A. Turner, Sustainable hydrogen production, Science 305 (2004) 972–974.

[32] S. H. Jensen, P. H. Larsen, M. Mogensen, Hydrogen and synthetic fuel production from renewable energy sources, Int. J. Hydrog. Energy 32 (2007) 3253–3257.

[33] P. Koutmos, J. J. McGuirk, Isothermal flow in a gas turbine combustor – a benchmark experimental study, Exp. Fluids 7 (1989) 344–354.

[34] J. F. Driscoll, Turbulent premixed combustion: Flamelet structure and its effect on turbulent burning velocities, Prog. Energy Combust. Sci. 34 (2008) 91–134.

[35] A. N. Lipatnikov, J. Chomiak, Turbulent flame speed and thickness: phenomenology, evaluation, and application in multi-dimensional simulations, Prog. Energy Combust. Sci. 28 (2002) 1–74.

[36] B. Zhou, C. Brackmann, Z. Wang, Z. Li, M. Richter, M. Aldén, X. S. Bai, Thin reaction zone and distributed reaction zone regimes in turbulent premixed methane/air flames: Scalar distributions and correlations, Combust. Flame 175 (2017) 220–236.

[37] M. J. Dunn, A. R. Masri, R. W. Bilger, A new piloted premixed jet burner to study strong finite-rate chemistry effects, Combust. Flame 151 (2007) 46–60.

[38] N. Peters, Laminar flamelet concepts in turbulent combustion, Proc. Combust. Inst. 21 (1988) 1231–1250.

[39] J. A. van Oijen, A. Donini, R. J. M. Bastiaans, J. H. M. ten Thije Boonkkamp, L. P. H. de Goey, State-of-the-art in premixed combustion modeling using flamelet generated manifolds, Prog. Energy Combust. Sci. 57 (2016) 30–74.

[40] L. Y. Gicquel, G. Staffelbach, T. Poinsot, Large eddy simulations of gaseous flames in gas turbine combustion chambers, Prog. Energy Combust. Sci. 38 (2012) 782–817.

[41] J. M. Duclos, D. Veynante, T. Poinsot, A comparison of flamelet models for premixed turbulent combustion, Combust. Flame 95 (1993) 101–117.

[42] A. W. Skiba, C. D. Carter, S. D. Hammack, J. F. Driscoll, Experimental assessment of the progress variable space structure of premixed flames subjected to extreme turbulence, Proc. Combust. Inst. 38 (2021) 2893–2900.

[43] B. Zhou, C. Brackmann, Q. Li, Z. Wang, P. Petersson, Z. Li, M. Aldén, X. S. Bai, Distributed reactions in highly turbulent premixed methane/air flames: Part I. Flame structure characterization, Combust. Flame 162 (2015) 2937–2953.

[44] B. Zhou, C. Brackmann, Z. Li, M. Aldén, X. S. Bai, Simultaneous multi-species and temperature visualization of premixed flames in the distributed reaction zone regime, Proc. Combust. Inst. 35 (2015) 1409–1416.

[45] M. J. Dunn, A. R. Masri, R. W. Bilger, R. S. Barlow, G. H. Wang, The compositional structure of highly turbulent piloted premixed flames issuing into a hot coflow, Proc. Combust. Inst. 32 (2009) 1779–1786.

[46] M. J. Dunn, A. R. Masri, R. W. Bilger, R. S. Barlow, Finite rate chemistry effects in highly sheared turbulent premixed flames, Flow Turbul. Combust. 85 (2010) 621–648.

[47] H. Wang, E. R. Hawkes, B. Savard, J. H. Chen, Direct numerical simulation of a high Ka CH_4/air stratified premixed jet flame, Combust. Flame 193 (2018) 229–245.

[48] H. Wang, E. R. Hawkes, J. H. Chen, B. Zhou, Z. Li, M. Aldén, Direct numerical simulations of a high Karlovitz number laboratory premixed jet flame–an analysis of flame stretch and flame thickening, J. Fluid Mech. 815 (2017) 511–536.

[49] B. Zhou, Q. Li, Y. He, P. Petersson, Z. Li, M. Aldén, X.-S. Bai, Visualization of multi-regime turbulent combustion in swirl-stabilized lean premixed flames, Combust. Flame 162 (2015) 2954–2958.

[50] D. G. Goodwin, R. L. Speth, H. K. Moffat, B. W. Weber, Cantera: An object-oriented software toolkit for chemical kinetics, thermodynamics, and transport processes, 2018, `https://www.cantera.org`, Version 2.4.0.

[51] A. Skiba, On the structure of premixed flames subjected to extreme levels of turbulence, Ph.D. thesis, The University of Michigan (2017).

[52] K. K. Kuo, R. Acharya, Fundamentals of turbulent and multiphase combustion, John Wiley & Sons, 2012.

[53] A. W. Skiba, T. M. Wabel, J. E. Temme, J. F. Driscoll, Measurements to determine the regimes of turbulent premixed flames, 51st AIAA/SAE/ASEE Joint Propulsion Conference (2015) p. 4089.

[54] J. E. Temme, T. M. Wabel, A. W. Skiba, J. F. Driscoll, Measurements of premixed turbulent combustion regimes of high Reynolds number flames, 53rd AIAA Aerospace Sciences Meeting (2015) p. 0168.

[55] T. M. Wabel, A. W. Skiba, J. E. Temme, J. F. Driscoll, Measurements to determine the regimes of premixed flames in extreme turbulence, Proc. Combust. Inst. 36 (2017) 1809–1816.

[56] T. M. Wabel, An experimental investigation of premixed combustion in extreme turbulence, Ph.D. thesis, The University of Michigan (2017).

[57] F. Halter, C. Chauveau, N. Djebaïli-Chaumeix, I. Gökalp, Characterization of the effects of pressure and hydrogen concentration on laminar burning velocities of methane–hydrogen–air mixtures, Proc. Combust. Inst. 30 (2005) 201–208.

[58] J. Göttgens, F. Mauss, N. Peters, Analytic approximations of burning velocities and flame thicknesses of lean hydrogen, methane, ethylene, ethane, acetylene, and propane flames, Proc. Combust. Inst. 24 (1992) 129–135.

[59] H. N. Najm, P. H. Paul, C. J. Mueller, P. S. Wyckoff, On the adequacy of certain experimental observables as measurements of flame burning rate, Combust. Flame 113 (1998) 312–332.

[60] H. N. Najm, O. M. Knio, P. H. Paul, P. S. Wyckoff, A study of flame observables in premixed methane-air flames, Combust. Sci. Technol. 140 (1998) 369–403.

[61] B. Zhou, J. Kiefer, J. Zetterberg, Z. Li, M. Aldén, Strategy for PLIF single-shot HCO imaging in turbulent methane/air flames, Combust. Flame 161 (2014) 1566–1574.

[62] J. Kiefer, Z. Li, T. Seeger, A. Leipertz, M. Aldén, Planar laser-induced fluorescence of HCO for instantaneous flame front imaging in hydrocarbon flames, Proc. Combust. Inst. 32 (2009) 921–928.

[63] S. R. Turns, An introduction to combustion, McGraw-Hill New York, 1996.

[64] W. Tsang, R. F. Hampson, Chemical kinetic data base for combustion chemistry. Part I. Methane and related compounds, J. Phys. Chem. Ref. Data 15 (1986) 1087–1279.

[65] A. C. Eckbreth, Laser diagnostics for combustion temperature and species, Vol. 3, CRC Press, 1996.

[66] T. M. Wabel, P. Zhang, X. Zhao, H. Wang, E. Hawkes, A. M. Steinberg, Assessment of chemical scalars for heat release rate measurement in highly turbulent premixed combustion including experimental factors, Combust. Flame 194 (2018) 485–506.

[67] P. H. Paul, H. N. Najm, Planar laser-induced fluorescence imaging of flame heat release rate, Proc. Combust. Inst. 27 (1998) 43–50.

[68] D. C. Kyritsis, V. S. Santoro, A. Gomez, The effect of temperature correction on the measured thickness of formaldehyde zones in diffusion flames for 355 nm excitation, Exp. Fluids 37 (2004) 769–772.

[69] Q. V. Nguyen, P. H. Paul, The time evolution of a vortex-flame interaction observed via planar imaging of CH and OH, Proc. Combust. Inst. 26 (1996) 357–364.

[70] M. S. Mansour, N. Peters, Y. C. Chen, Investigation of scalar mixing in the thin reaction zones regime using a simultaneous CH-LIF/Rayleigh laser technique, Proc. Combust. Inst. 27 (1998) 767–773.

[71] G. J. Marshall, R. W. Pitz, Evaluation of heat release indicators in lean premixed H_2/Air cellular tubular flames, Proc. Combust. Inst. 37 (2019) 2029–2036.

[72] S. B. Pope, Turbulent flows, IOP Publishing, 2001.

[73] P. A. Davidson, Turbulence: an introduction for scientists and engineers, Oxford university press, 2015.

[74] R. Borghi, Turbulent combustion modelling, Prog. Energy Combust. Sci. 14 (1988) 245–292.

[75] T. Poinsot, D. Veynante, Theoretical and numerical combustion, second ed., R.T. Edwards, Philadelphia, USA, 2005.

[76] J. B. Bell, M. S. Day, J. F. Grcar, M. J. Lijewski, J. F. Driscoll, S. A. Filatyev, Numerical simulation of a laboratory-scale turbulent slot flame, Proc. Combust. Inst. 31 (2007) 1299–1307.

[77] A. Buschmann, F. Dinkelacker, T. Schäfer, M. Schäfer, J. Wolfrum, Measurement of the instantaneous detailed flame structure in turbulent premixed combustion, Proc. Combust. Inst. 26 (1996) 437–445.

[78] S. A. Filatyev, J. F. Driscoll, C. D. Carter, J. M. Donbar, Measured properties of turbulent premixed flames for model assessment, including burning velocities, stretch rates, and surface densities, Combust. Flame 141 (2005) 1–21.

[79] J. R. Osborne, S. A. Ramji, C. D. Carter, S. Peltier, S. Hammack, T. Lee, A. M. Steinberg, Simultaneous 10 kHz TPIV, OH PLIF, and CH_2O PLIF measurements of turbulent flame structure and dynamics, Exp. Fluids 57 (2016) 65.

[80] J. R. Osborne, S. A. Ramji, C. D. Carter, A. M. Steinberg, Relationship between local reaction rate and flame structure in turbulent premixed flames from simultaneous 10 kHz TPIV, OH PLIF, and CH_2O PLIF, Proc. Combust. Inst. 36 (2017) 1835–1841.

[81] J. Kariuki, A. Dowlut, R. Yuan, R. Balachandran, E. Mastorakos, Heat release imaging in turbulent premixed methane–air flames close to blow-off, Proc. Combust. Inst. 35 (2015) 1443–1450.

[82] J. Kariuki, A. Dowlut, R. Balachandran, E. Mastorakos, Heat release imaging in turbulent premixed ethylene-air flames near blow-off, Flow Turbul. Combust. 96 (2016) 1039–1051.

[83] A. Y. Poludnenko, E. S. Oran, The interaction of high-speed turbulence with flames: Global properties and internal flame structure, Combust. Flame 157 (2010) 995–1011.

[84] A. Y. Poludnenko, E. S. Oran, The interaction of high-speed turbulence with flames: Turbulent flame speed, Combust. Flame 158 (2011) 301–326.

[85] P. Tamadonfar, Ö. L. Gülder, Experimental investigation of the inner structure of premixed turbulent methane/air flames in the thin reaction zones regime, Combust. Flame 162 (2015) 115–128.

[86] A. Soika, F. Dinkelacker, A. Leipertz, Measurement of the resolved flame structure of turbulent premixed flames with constant Reynolds number and varied stoichiometry, Proc. Combust. Inst. 27 (1998) 785–792.

[87] F. Halter, C. Chauveau, I. Gökalp, Investigations on the flamelet inner structure of turbulent premixed flames, Combust. Sci. Technol. 180 (2008) 713–728.

[88] A. Aspden, M. Day, J. Bell, Towards the distributed burning regime in turbulent premixed flames, J. Fluid Mech. 871 (2019) 1–21.

[89] A. J. Aspden, M. S. Day, J. B. Bell, Lewis number effects in distributed flames, Proc. Combust. Inst. 33 (2011) 1473–1480.

[90] A. J. Aspden, M. S. Day, J. B. Bell, Turbulence–flame interactions in lean premixed hydrogen: transition to the distributed burning regime, J. Fluid Mech. 680 (2011) 287–320.

[91] R. K. Cheng, I. G. Shepherd, B. Bedat, L. Talbot, Premixed turbulent flame structures in moderate and intense isotropic turbulence, Combust. Sci. Technol. 174 (2002) 29–59.

[92] I. G. Shepherd, R. K. Cheng, The burning rate of premixed flames in moderate and intense turbulence, Combust. Flame 127 (2001) 2066–2075.

[93] K. N. C. Bray, R. S. Cant, Some applications of Kolmogorov's turbulence research in the field of combustion, Proc. R. Soc. London Ser. A 434 (1991) 217–240.

[94] S. Kheirkhah, Experimental study of turbulent premixed combustion in V-shaped flames, Ph.D. thesis, The University of Toronto (2016).

[95] D. Durox, S. Ducruix, S. Candel, Experiments on collapsing cylindrical flames, Combust. Flame 125 (2001) 982–1000.

[96] C. J. Sun, C. J. Sung, L. He, C. K. Law, Dynamics of weakly stretched flames: quantitative description and extraction of global flame parameters, Combust. Flame 118 (1999) 108–128.

[97] S. Lapointe, G. Blanquart, Fuel and chemistry effects in high Karlovitz premixed turbulent flames, Combust. Flame 167 (2016) 294–307.

[98] G. V. Nivarti, R. S. Cant, Scalar transport and the validity of Damköhler's hypotheses for flame propagation in intense turbulence, Phys. Fluids 29 (2017) 085107.

[99] G. Nivarti, S. Cant, Direct numerical simulation of the bending effect in turbulent premixed flames, Proc. Combust. Inst. 36 (2017) 1903–1910.

[100] D. Lee, K. Y. Huh, Validation of analytical expressions for turbulent burning velocity in stagnating and freely propagating turbulent premixed flames, Combust. Flame 159 (2012) 1576–1591.

[101] F. T. C. Yuen, Ö. L. Gülder, Dynamics of lean-premixed turbulent combustion at high turbulence intensities, Combust. Sci. Technol. 182 (2010) 544–558.

[102] B. Lewis, G. Von Elbe, Combustion, flames and explosions of gases, Elsevier, 2012.

[103] F. T. C. Yuen, Ö. L. Gülder, Turbulent premixed flame front dynamics and implications for limits of flamelet hypothesis, Proc. Combust. Inst. 34 (2013) 1393–1400.

[104] R. G. Abdel-Gayed, K. J. Al-Khishali, D. Bradley, Turbulent burning velocities and flame straining in explosions, Proc. R. Soc. A 391 (1984) 393–414.

[105] R. G. Abdel-Gayed, D. Bradley, M. Lawes, Turbulent burning velocities: A general correlation in terms of straining rates, Proc. R. Soc. A 414 (1987) 389–413.

[106] F. Halter, C. Chauveau, I. Gökalp, Characterization of the effects of hydrogen addition in premixed methane/air flames, Int. J. Hydrog. Energy 32 (2007) 2585–2592.

[107] C. Mandilas, M. P. Ormsby, C. G. W. Sheppard, R. Woolley, Effects of hydrogen addition on laminar and turbulent premixed methane and iso-octane–air flames, Proc. Combust. Inst. 31 (2007) 1443–1450.

[108] T. Boushaki, Y. Dhué, L. Selle, B. Ferret, T. Poinsot, Effects of hydrogen and steam addition on laminar burning velocity of methane–air premixed flame: Experimental and numerical analysis, Int. J. Hydrog. Energy 37 (2012) 9412–9422.

[109] E. Hu, Z. Huang, J. He, C. Jin, J. Zheng, Experimental and numerical study on laminar burning characteristics of premixed methane–hydrogen–air flames, Int. J. Hydrog. Energy 34 (2009) 4876–4888.

[110] M. Emadi, D. Karkow, T. Salameh, A. Gohil, A. Ratner, Flame structure changes resulting from hydrogen-enrichment and pressurization for low-swirl premixed methane–air flames, Int. J. Hydrog. Energy 37 (2012) 10397–10404.

[111] P. Griebel, E. Boschek, P. Jansohn, Lean blowout limits and NO_x emissions of turbulent, lean premixed, hydrogen-enriched methane/air flames at high pressure, J. Eng. Gas Turb. Power 129 (2007) 404–410.

[112] O. Tuncer, S. Acharya, J. H. Uhm, Dynamics, nox and flashback characteristics of confined pre-mixed hydrogen enriched methane flames, ASME Turbo Expo 2007: Power for Land, Sea, and Air (2007) 857–868.

[113] R. Schefer, Hydrogen enrichment for improved lean flame stability, Int. J. Hydrog. Energy 28 (2003) 1131–1141.

[114] M. Subramanya, A. Choudhuri, Investigation of combustion instability effects on the flame characteristics of fuel blends, 5th Int. Energy Convers. Eng. Conf. Exhib. (IECEC) (2007) 4796.

[115] W. Zhang, J. Wang, W. Lin, G. Li, Z. Hu, M. Zhang, Z. Huang, Effect of hydrogen enrichment on flame broadening of turbulent premixed flames in thin reaction regime, Int. J. Hydrog. Energy 46 (2021) 1210–1218.

[116] H. Guo, B. Tayebi, C. Galizzi, D. Escudié, Burning rates and surface characteristics of hydrogen-enriched turbulent lean premixed methane–air flames, Int. J. Hydrog. Energy 35 (2010) 11342–11348.

[117] A. W. Skiba, T. M. Wabel, J. E. Temme, J. F. Driscoll, Experimental assessment of premixed flames subjected to extreme turbulence, 54th AIAA Aerospace Sciences Meeting (2016) 1454.

[118] A. W. Skiba, T. M. Wabel, C. D. Carter, S. D. Hammack, J. E. Temme, T. Lee, J. F. Driscoll, Reaction layer visualization: A comparison of two PLIF techniques and advantages of kHz-imaging, Proc. Combust. Inst. 36 (2017) 4593–4601.

[119] T. M. Wabel, A. W. Skiba, J. F. Driscoll, Evolution of turbulence through a broadened preheat zone in a premixed piloted Bunsen flame from conditionally-averaged velocity measurements, Combust. Flame 188 (2018) 13–27.

[120] C. Brackmann, B. Zhou, Z. Li, M. Aldén, Strategies for quantitative planar laser-induced fluorescence of NH radicals in flames, Combust. Sci. Technol. 188 (2016) 529–541.

[121] J. Rosell, X.-S. Bai, J. Sjoholm, B. Zhou, Z. Li, Z. Wang, P. Pettersson, Z. Li, M. Richter, M. Aldén, Multi-species PLIF study of the structures of turbulent premixed methane/air jet flames in the flamelet and thin-reaction zones regimes, Combust. Flame 182 (2017) 324–338.

[122] B. Coriton, J. H. Frank, A. G. Hsu, M. D. Smooke, A. Gomez, Effect of quenching of the oxidation layer in highly turbulent counterflow premixed flames, Proc. Combust. Inst. 33 (2011) 1647–1654.

[123] Z. S. Li, B. Li, Z. W. Sun, X. S. Bai, M. Aldén, Turbulence and combustion interaction: High resolution local flame front structure visualization using simultaneous single-shot PLIF imaging of CH, OH, and CH_2O in a piloted premixed jet flame, Combust. Flame 157 (2010) 1087–1096.

[124] P. Petersson, J. Olofsson, C. Brackman, H. Seyfried, J. Zetterberg, M. Richter, M. Aldén, M. A. Linne, R. K. Cheng, A. Nauert, et al., Simultaneous PIV/OH-PLIF, Rayleigh thermometry/OH-PLIF and stereo PIV measurements in a low-swirl flame, Appl. Opt. 46 (2007) 3928–3936.

[125] K. J. Nogenmyr, C. Fureby, X. S. Bai, P. Petersson, R. Collin, M. Linne, Large eddy simulation and laser diagnostic studies on a low swirl stratified premixed flame, Combust. Flame 156 (2009) 25–36.

[126] S. Kheirkhah, Ö. Gülder, Topology and brush thickness of turbulent premixed V-shaped flames, Flow Turbul. Combust. 93 (2014) 439–459.

[127] S. Kheirkhah, Ö. L. Gülder, G. Maurice, F. Halter, I. Gökalp, On periodic behavior of weakly turbulent premixed flame corrugations, Combust. Flame 168 (2016) 147–165.

[128] A. Fayoux, K. Zähringer, O. Gicquel, J. C. Rolon, Experimental and numerical de-

termination of heat release in counterflow premixed laminar flames, Proc. Combust. Inst. 30 (2005) 251–257.

[129] B. O. Ayoola, R. Balachandran, J. H. Frank, E. Mastorakos, C. F. Kaminski, Spatially resolved heat release rate measurements in turbulent premixed flames, Combust. Flame 144 (2006) 1–16.

[130] M. Röder, T. Dreier, C. Schulz, Simultaneous measurement of localized heat release with OH/CH_2O-LIF imaging and spatially integrated OH^* chemiluminescence in turbulent swirl flames, Appl. Phys. B 107 (2012) 611–617.

[131] M. Röder, T. Dreier, C. Schulz, Simultaneous measurement of localized heat-release with OH/CH_2O–LIF imaging and spatially integrated OH^* chemiluminescence in turbulent swirl flames, Proc. Combust. Inst. 34 (2013) 3549–3556.

[132] Y. Hardalupas, C. S. Panoutsos, A. M. K. P. Taylor, Spatial resolution of a chemiluminescence sensor for local heat-release rate and equivalence ratio measurements in a model gas turbine combustor, Exp. Fluids 49 (2010) 883–909.

[133] B. Ayoola, G. Hartung, C. Armitage, J. Hult, R. Cant, C. Kaminski, Temperature response of turbulent premixed flames to inlet velocity oscillations, Exp. Fluids 46 (2009) 27.

[134] P. C. Vena, B. Deschamps, H. Guo, G. J. Smallwood, M. R. Johnson, Heat release rate variations in a globally stoichiometric, stratified iso-octane/air turbulent V-flame, Combust. Flame 162 (2015) 944–959.

[135] J. E. Harrington, K. C. Smyth, Laser-induced fluorescence measurements of formaldehyde in a methane/air diffusion flame, Chem. Phys. Lett. 202 (1993) 196–202.

[136] C. Brackmann, J. Nygren, X. Bai, Z. Li, H. Bladh, B. Axelsson, I. Denbratt, L. Koopmans, P. E. Bengtsson, M. Aldén, Laser-induced fluorescence of formaldehyde in com-

bustion using third harmonic Nd:YAG laser excitation, Spectrochim. Acta. A Mol. Biomol. Spectrosc. 59 (2003) 3347–3356.

[137] K. Yamamoto, S. Isii, M. Ohnishi, Local flame structure and turbulent burning velocity by joint PLIF imaging, Proc. Combust. Inst. 33 (2011) 1285–1292.

[138] N. T. Clemens, Flow imaging, encyclopedia of imaging science and technology, John Wiley and Sons Inc., 2002.

[139] G. H. Wang, N. T. Clemens, Effects of imaging system blur on measurements of flow scalars and scalar gradients, Exp. Fluids 37 (2004) 194–205.

[140] J. Westerweel, F. Scarano, Universal outlier detection for PIV data, Exp. Fluids 39 (2005) 1096–1100.

[141] J. Westerweel, D. Dabiri, M. Gharib, The effect of a discrete window offset on the accuracy of cross-correlation analysis of digital PIV recordings, Exp. Fluids 23 (1997) 20–28.

[142] A. Sciacchitano, D. R. Neal, B. L. Smith, S. O. Warner, P. P. Vlachos, B. Wieneke, F. Scarano, Collaborative framework for PIV uncertainty quantification: comparative assessment of methods, Meas. Sci. Technol. 26 (2015) 074004.

[143] A. Sciacchitano, B. Wieneke, F. Scarano, PIV uncertainty quantification by image matching, Meas. Sci. Technol. 24 (2013) 045302.

[144] B. Wieneke, PIV uncertainty quantification from correlation statistics, Meas. Sci. Technol. 26 (2015) 074002.

[145] J. J. Charonko, P. P. Vlachos, Estimation of uncertainty bounds for individual particle image velocimetry measurements from cross-correlation peak ratio, Meas. Sci. Technol. 24 (2013) 065301.

[146] B. H. Timmins, B. W. Wilson, B. L. Smith, P. P. Vlachos, A method for automatic estimation of instantaneous local uncertainty in particle image velocimetry measurements, Exp. Fluids 53 (2012) 1133–1147.

[147] J. Westerweel, Theoretical analysis of the measurement precision in particle image velocimetry, Exp. Fluids 29 (2000) S003–S012.

[148] H. Huang, D. Dabiri, M. Gharib, On errors of digital particle image velocimetry, Meas. Sci. Technol. 8 (1997) 1427.

[149] H. Nobach, E. Bodenschatz, Limitations of accuracy in PIV due to individual variations of particle image intensities, Exp. Fluids 47 (2009) 27–38.

[150] B. Coriton, S.-K. Im, M. Gamba, J. H. Frank, Flow field and scalar measurements in a series of turbulent partially-premixed dimethyl ether/air jet flames, Combust. Flame 180 (2017) 40–52.

[151] A. K. Prasad, Stereoscopic particle image velocimetry, Exp. Fluids 29 (2000) 103–116.

[152] J. Westerweel, On velocity gradients in PIV interrogation, Exp. Fluids 44 (2008) 831–842.

[153] J. M. Foucaut, J. Carlier, M. Stanislas, PIV optimization for the study of turbulent flow using spectral analysis, Meas. Sci. Technol. 15 (2004) 1046.

[154] P. Lavoie, G. Avallone, F. De Gregorio, G. P. Romano, R. A. Antonia, Spatial resolution of PIV for the measurement of turbulence, Exp. Fluids 43 (2007) 39–51.

[155] N. Worth, T. Nickels, N. Swaminathan, A tomographic PIV resolution study based on homogeneous isotropic turbulence DNS data, Exp. Fluids 49 (2010) 637–656.

[156] K. E. Meyer, J. M. Pedersen, O. Özcan, A turbulent jet in crossflow analysed with proper orthogonal decomposition, J. Fluid Mech. 583 (2007) 199–227.

[157] I. A. Mulla, A. Dowlut, T. Hussain, Z. M. Nikolaou, S. R. Chakravarthy, N. Swaminathan, R. Balachandran, Heat release rate estimation in laminar premixed flames using laser-induced fluorescence of CH_2O and H-atom, Combust. Flame 165 (2016) 373–383.

[158] B. R. Chowdhury, B. M. Cetegen, Effects of free stream flow turbulence on blowoff characteristics of bluff-body stabilized premixed flames, Combust. Flame 190 (2018) 302–316.

[159] S. Chaudhuri, S. Kostka, M. W. Renfro, B. M. Cetegen, Blowoff dynamics of bluff body stabilized turbulent premixed flames, Combust. Flame 157 (2010) 790–802.

[160] E. R. Hawkes, R. Sankaran, J. H. Chen, Estimates of the three-dimensional flame surface density and every term in its transport equation from two-dimensional measurements, Proc. Combust. Inst. 33 (2011) 1447–1454.

[161] J. B. Bell, M. S. Day, I. G. Shepherd, M. R. Johnson, R. K. Cheng, J. F. Grcar, V. E. Beckner, M. J. Lijewski, Numerical simulation of a laboratory-scale turbulent V-flame, Proc. Natl. Acad. Sci. U.S.A. 102 (2005) 10006–10011.

[162] M. Zhang, J. Wang, W. Jin, Z. Huang, H. Kobayashi, L. Ma, Estimation of 3D flame surface density and global fuel consumption rate from 2D PLIF images of turbulent premixed flame, Combust. Flame 162 (2015) 2087–2097.

[163] L. P. H. de Goey, T. Plessing, R. T. E. Hermanns, N. Peters, Analysis of the flame thickness of turbulent flamelets in the thin reaction zones regime, Proc. Combust. Inst. 30 (2005) 859–866.

[164] A. Tyagi, J. O'Connor, Towards a method of estimating out-of-plane effects on measurements of turbulent flame dynamics, Combust. Flame 216 (2020) 206–222.

[165] D. Veynante, G. Lodato, P. Domingo, L. Vervisch, E. R. Hawkes, Estimation of three-dimensional flame surface densities from planar images in turbulent premixed combustion, Exp. Fluids 49 (2010) 267–278.

[166] O. Chatakonda, E. R. Hawkes, A. J. Aspden, A. R. Kerstein, H. Kolla, J. H. Chen, On the fractal characteristics of low Damköhler number flames, Combust. Flame 160 (2013) 2422–2433.

[167] F. Dinkelacker, A. Soika, D. Most, D. Hofmann, A. Leipertz, W. Polifke, K. Döbbeling, Structure of locally quenched highly turbulent lean premixed flames, Proc. Combust. Inst. 27 (1998) 857–865.

[168] J. Jeong, F. Hussain, On the identification of a vortex, J. Fluid Mech. 285 (1995) 69–94.

[169] R. Cucitore, M. Quadrio, A. Baron, On the effectiveness and limitations of local criteria for the identification of a vortex, Eur. J. Mech. B/Fluids 18 (1999) 261–282.

[170] P. Chakraborty, S. Balachandar, R. J. Adrian, On the relationships between local vortex identification schemes, J. Fluid Mech. 535 (2005) 189–214.

[171] W. S. Fu, Y. C. Lai, C. G. Li, Estimation of turbulent natural convection in horizontal parallel plates by the Q criterion, Int. Commun. Heat Mass Transf. 45 (2013) 41–46.

[172] S. Lapointe, B. Savard, G. Blanquart, Differential diffusion effects, distributed burning, and local extinctions in high Karlovitz premixed flames, Combust. Flame 162 (2015) 3341–3355.

[173] V. L. Zimont, Theory of turbulent combustion of a homogeneous fuel mixture at high Reynolds numbers, Combust. Explos. Shock Waves 15 (1979) 305–311.

[174] C. Jainski, M. Rißmann, B. Böhm, A. Dreizler, Experimental investigation of flame

surface density and mean reaction rate during flame–wall interaction, Proc. Combust. Inst. 36 (2017) 1827–1834.

[175] V. Caux-Brisebois, A. M. Steinberg, C. M. Arndt, W. Meier, Thermo-acoustic velocity coupling in a swirl stabilized gas turbine model combustor, Combust. Flame 161 (2014) 3166–3180.

[176] N. Chakraborty, D. Alwazzan, M. Klein, R. S. Cant, On the validity of Damköhler's first hypothesis in turbulent bunsen burner flames: A computational analysis, Proc. Combust. Inst. 37 (2019) 2231–2239.

[177] P. Venkateswaran, A. Marshall, D. H. Shin, D. Noble, J. Seitzman, T. Lieuwen, Measurements and analysis of turbulent consumption speeds of H_2/CO mixtures, Combust. Flame 158 (2011) 1602–1614.

[178] A. Marshall, J. Lundrigan, P. Venkateswaran, J. Seitzman, T. Lieuwen, Fuel effects on leading point curvature statistics of high hydrogen content fuels, Proc. Combust. Inst. 35 (2015) 1417–1424.

[179] A. W. Skiba, C. D. Carter, S. D. Hammack, J. F. Driscoll, The effects of resolution on the fidelity of two dimensional flame surface density measurements in premixed flame subject to extreme levels of turbulence, US National Meeting of The Combustion Institute, Pasadena CA (2019).

[180] E. R. Hawkes, J. H. Chen, Comparison of direct numerical simulation of lean premixed methane–air flames with strained laminar flame calculations, Combust. Flame 144 (2006) 112–125.

[181] J. Kim, A. Satija, R. P. Lucht, J. P. Gore, Effects of turbulent flow regime on perforated plate stabilized piloted lean premixed flames, Combust. Flame 211 (2020) 158–172.

[182] A. Garmory, E. Mastorakos, Capturing localised extinction in sandia Flame F with LES–CMC, Proc. Combust. Inst. 33 (2011) 1673–1680.

[183] W. Jin, S. A. Steinmetz, M. Juddoo, M. J. Dunn, Z. Huang, A. R. Masri, Effects of shear inhomogeneities on the structure of turbulent premixed flames, Combust. Flame 208 (2019) 63–78.

[184] R. Sadanandan, M. Stöhr, W. Meier, Simultaneous OH-PLIF and PIV measurements in a gas turbine model combustor, Appl. Phys. B 90 (2008) 609–618.

[185] Q. An, A. M. Steinberg, The role of strain rate, local extinction, and hydrodynamic instability on transition between attached and lifted swirl flames, Combust. Flame 199 (2019) 267–278.

[186] J. Kariuki, J. R. Dawson, E. Mastorakos, Measurements in turbulent premixed bluff body flames close to blow-off, Combust. Flame 159 (2012) 2589–2607.

[187] A. Attili, S. Luca, D. Denker, F. Bisetti, H. Pitsch, Turbulent flame speed and reaction layer thickening in premixed jet flames at constant Karlovitz and increasing Reynolds numbers, Proc. Combust. Inst. 38 (2021) 2939–2947.

[188] S. Trivedi, R. S. Cant, Turbulence intensity and length scale effects on premixed turbulent flame propagation, Flow Turbul. Combust. (2021) 1–23.

[189] M. M. Kamal, C. Duwig, S. Balusamy, R. Zhou, S. Hochgreb, Proper orthogonal decomposition analysis of non-swirling turbulent stratified and premixed methane/air flames, ASME Turbo Expo 2014: Gas Turbine Technical Conference and Exposition, Dusseldorf, Germany (2014).

[190] N. Bouvet, F. Halter, C. Chauveau, Y. Yoon, On the effective Lewis number formulations for lean hydrogen/hydrocarbon/air mixtures, Int. J. Hydrog. Energy 38 (2013) 5949–5960.

[191] J. Bechtold, M. Matalon, The dependence of the Markstein length on stoichiometry, Combust. Flame 127 (2001) 1906–1913.

[192] R. Addabbo, J. Bechtold, M. Matalon, Wrinkling of spherically expanding flames, Proc. Combust. Inst. 29 (2002) 1527–1535.

[193] G. K. Giannakopoulos, A. Gatzoulis, C. E. Frouzakis, M. Matalon, A. G. Tomboulides, Consistent definitions of "Flame Displacement Speed" and "Markstein Length" for premixed flame propagation, Combust. Flame 162 (2015) 1249–1264.

[194] S. Mathur, P. Tondon, S. Saxena, Thermal conductivity of binary, ternary and quaternary mixtures of rare gases, Mol. Phys. 12 (1967) 569–579.

Appendices

Appendix A

GRI-Mech 3.0 for simulation of hydrogen-enriched methane-air flames at atmospheric condition

GRI-Mech 3.0 is developed for natural gas combustion (which mainly contains methane); however, the analyses show that GRI-Mech 3.0 allows for relatively accurate prediction of laminar hydrogen-air premixed flames combustion chemistry too (at $P = 1$ atm). In order to show this, Cantera simulations were run using GRI-Mech 3.0 as well as the mechanisms developed and used in [20–23]. The structure of the heat release rate obtained from the above mechanisms and that from GRI-Mech 3.0 are presented in Fig. A.1. The results pertain to freely propagating hydrogen-air premixed flames with fuel-air equivalence ratio of 0.7 at $P = 1$ atm. As can be seen, the predictions of GRI-Mech 3.0 is similar to the mechanisms developed for pure hydrogen flames in the studies of [20–23]. Similarly, the laminar flame speed of freely propagating hydrogen-air premixed flames at $\phi = 0.7$ and $P = 1$ atm was obtained and equals to 1.23, 1.33, 1.29, 1.41, and 1.39 m/s using GRI-Mech. 3.0 and those of [20], [21], [22], and [23], respectively. The similarity in distribution of the heat release rate and the laminar flame speed suggest that GRI-Mech 3.0 allows for relatively accurate prediction of these parameters even for freely propagating laminar hydrogen-air premixed flames for $\phi = 0.7$ and at $P = 1$ atm. Considering the accuracy of using GRI-Mech 3.0 for laminar methane-air flames, this mechanism can be utilized for simulation of laminar

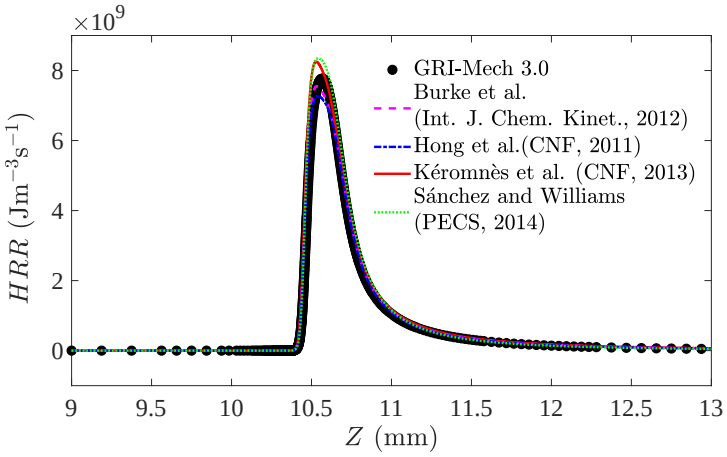

Fig. A.1. Cantera simulation results of HRR variation across a freely propagating laminar premixed flame of hydrogen and air. The results are generated using the GRI-Mech. 3.0 and the mechanisms proposed in [20–23].

hydrogen-enriched methane-air premixed flames as well.

Appendix B

POD analysis for removing Kelvin-Helmholtz instability from non-reacting velocity data

The Proper Orthogonal Decomposition (POD) technique was utilized to remove the dominant flow structures from non-reacting flow data related to conditions with zero perforated plates. These analyses were performed for four mean bulk flow velocities of 5,15, 25, and 35 m/s, which are tested in this thesis. For calculation of the POD modes, similar procedure to that presented in [94, 127, 156, 189] was utilized. First, the eigenvalue of the velocity data related to the i^{th} mode (γ_i) as well as the cumulative mode energy ($\Sigma_{k=1}^{k=i}\gamma_k$) are estimated, and the results are presented in Figs. B.1(a–c) and (d–f), respectively. The results in Figs. B.1(a and d), (b and e), and (c and f) correspond to velocity components along y, x, and z directions, respectively. The results presented in Figs. B.1(d–f) are normalized by the total modes energy. The total number of SPIV image pairs used for calculation of the non-reacting velocity data is 1040, and corresponds to the maximum number of modes in Fig. B.1. As can be seen, the first two modes are relatively energetic and contribute to 10 to 60% of the total cumulative mode energy depending on the tested mean bulk flow velocity.

Since the first and second modes are mainly related to the dominant flow structures, the corresponding mode-shapes for the non-reacting condition and for no turbulence generator

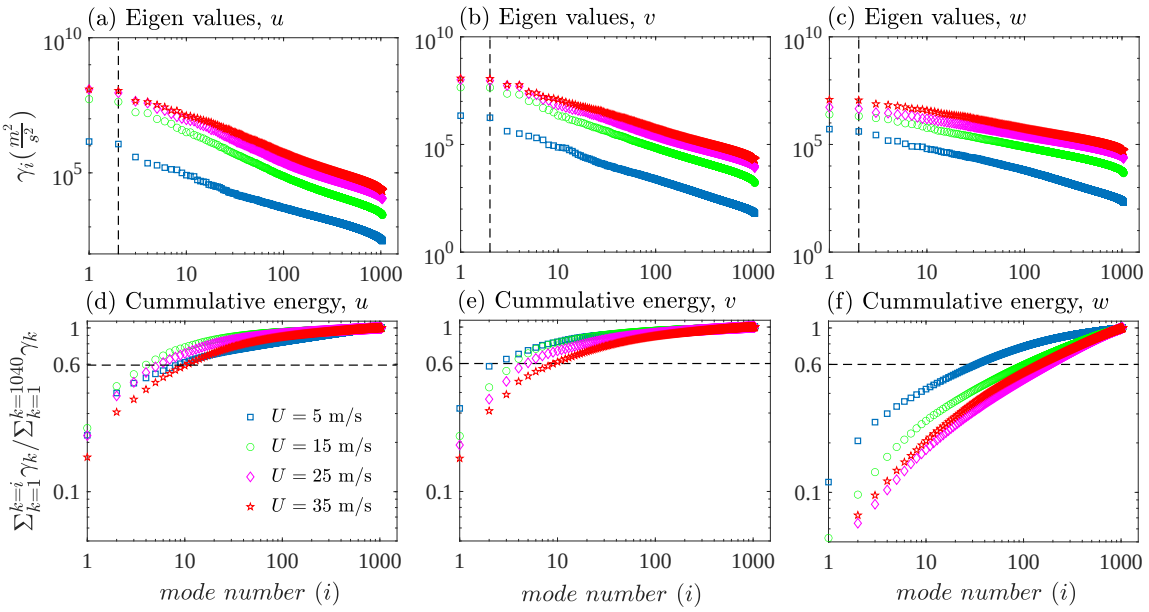

Fig. B.1. (a–c) are the eigenvalues of the non-reacting velocity data with no turbulence generator and U = 5,15, 25, and 35 m/s. (d–f) are the normalized cumulative mode energies.

were calculated and presented in Fig. B.2. Results shown in Figs. B.2(a–f), (g–l), (m–r), and (s–x) correspond to mean bulk flow velocities of 5, 15, 25, and 35 m/s, respectively. The first, third, and fifth columns in the figure are the first POD mode of the velocity fluctuations along the y, x, and z axes, respectively. Also, the second, fourth, and sixth columns are the second POD mode of the velocity fluctuations along the y, x, and z axes, respectively. As can be seen, the dominant flow structures are apparent, they are located near the jet shear layers, and they correspond to the Kelvin-Helmholtz instability. These vortices have been previously observed and reported for the same burner except for a larger exit diameter of 48.4 mm and mean bulk flow velocities ranging from 4.0 to 8.3 m/s, please see [126, 127].

In order to assess the impact of the dominant flow structures on the turbulent flow characteristics, the first n POD modes were removed from the velocity data (with n varying from 0 to 1039), the velocity fields were reconstructed, the root-mean-square (RMS) velocity fluctuations were calculated, and the values corresponding to u', v', and w' were averaged inside the FCR window shown in Fig. 2.3. Figures B.3(a), (b), and (c) present variations of

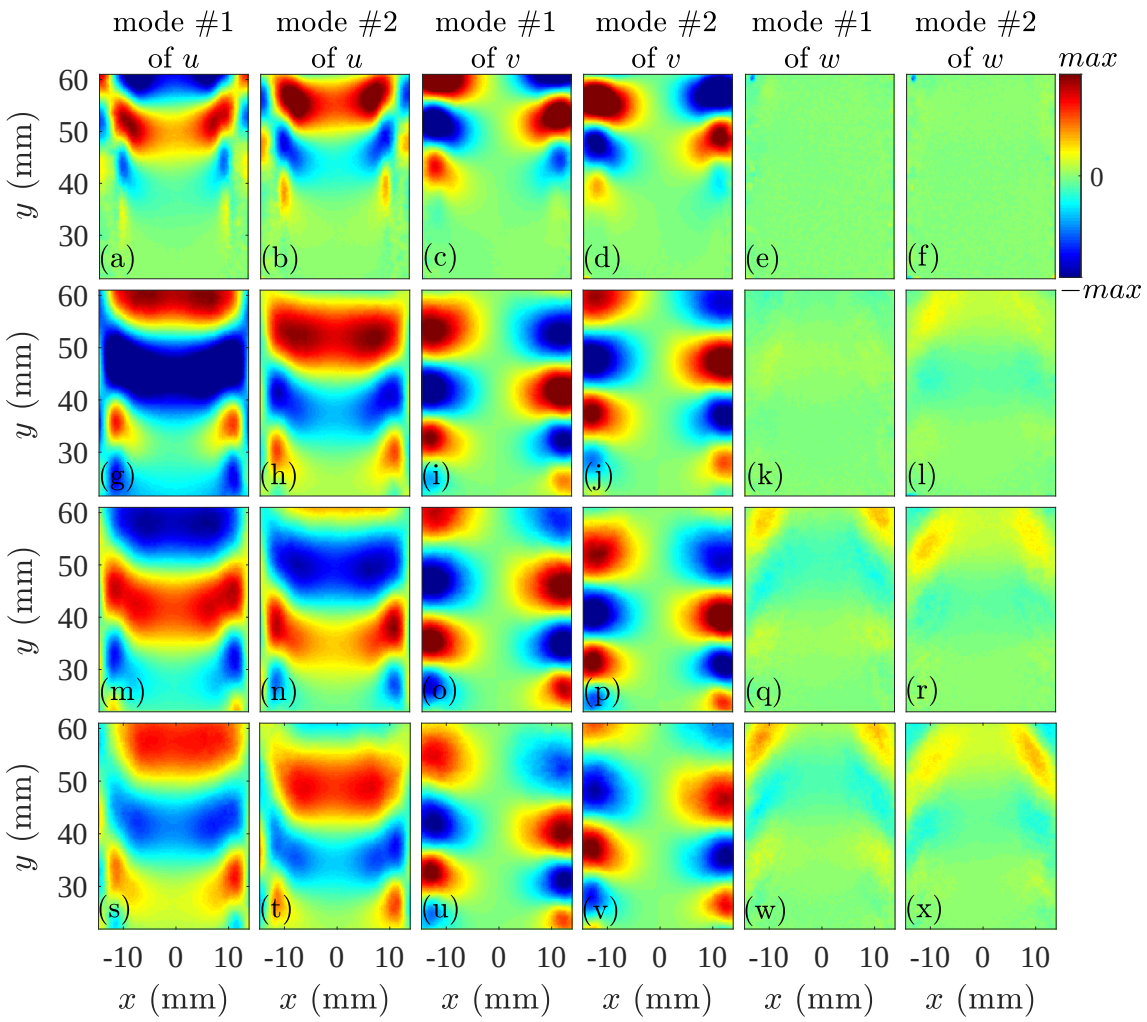

Fig. B.2. Mode-shapes of the non-reacting flow with no turbulence generator related to $U = 5$ m/s (a–f), $U = 15$ m/s (g–l), $U = 25$ m/s (m–r), and $U = 35$ m/s (s–x). The first (second), third (fourth), and fifth (sixth) columns correspond to mode #1 (#2) for u, v, and w components of the velocity data, respectively.

the averaged u', v', and w' inside the FCR window in Fig. 2.3 for several values of n. For example, $n = 0$ means that no POD mode is excluded for the RMS calculations. As can be seen, the RMS values are relatively insensitive to removing the modes up to about the first two modes. This is because the RMS values are calculated inside the FCR window, whose flow field is not significantly influenced by the Kelvin-Helmholtz instability. Nevertheless, the RMS velocity data were reported in Table 2.1 for $n = 2$, i.e. the first two modes excluded from the velocity data for the RMS calculations. These values are extracted from Fig. B.3 at $n + 1 = 3$, which is highlighted by the dashed line.

The integral length scale averaged inside the FCR window in Fig. 2.3 was evaluated for

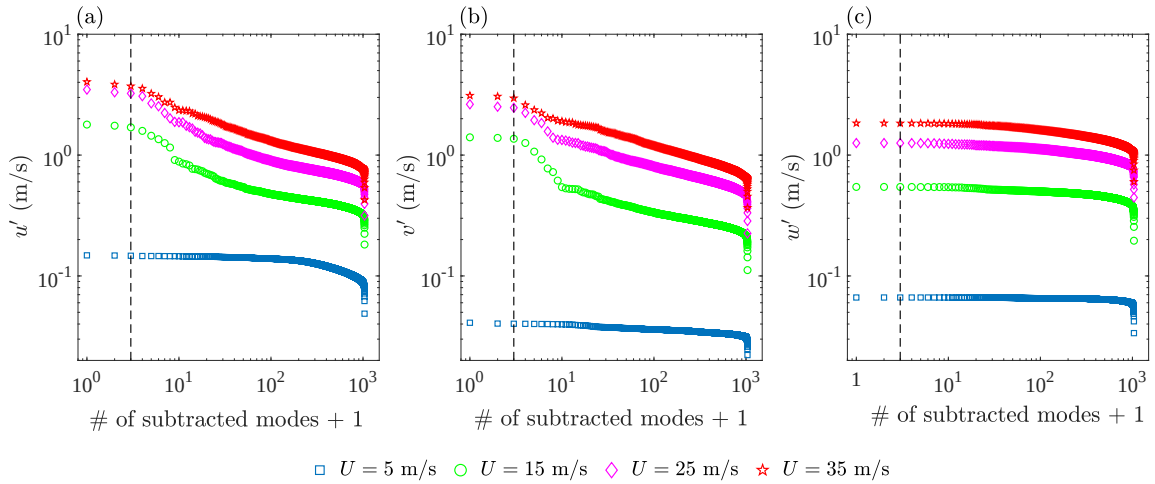

Fig. B.3. (a), (b), and (c) are the root-mean-square of the velocity data along the y, x, and z axes after excluding the first n POD modes from the calculations. The results are calculated inside the red FCR window in Fig. 2.3.

Table B.1. Effect of excluding the first n number of modes from the velocity data on the integral length scale averaged inside the FCR window on Fig. 2.3. $n = 0$ means no POD mode is excluded. The reported values are in mm.

# of excluded modes (n)	0	1	2	5	10	20	100	500
$U = 5$ m/s	2.3	2.5	2.1	2.2	2.1	2.2	0.5	0.4
$U = 15$ m/s	4.1	3.8	3.9	3.4	2.9	2.1	0.5	0.4
$U = 25$ m/s	4.1	3.9	3.9	3.0	3.5	2.2	0.7	0.4
$U = 35$ m/s	3.9	3.6	3.6	3.0	3.2	2.5	0.8	0.4

several values of n. The values of the integral length scale averaged in the FCR window for no, 1, 2, 5, 10, 20, 100, and 500 removed modes are tabulated in Table B.1. As can be seen, the averaged value of the integral length scale is nearly insensitive to the extracted number of modes up to $n = 2$. This is because the region inside the FCR window is not significantly influenced by the Kelvin-Helmholtz instability. The averaged values of integral length scale related to $n = 2$ (see the cells with the green font) are presented in Table 2.1 and were used for locating the tested conditions on the Borghi-Peters diagram.

Appendix C

Effective Lewis number estimation

The effective Lewis number (Le_{eff}) was estimated following the methodology of [190–193] and was presented in Tables 2.1 and 2.2. Bouvet et al. [190] suggested that, for stoichiometric mixture of bi-component fuels (such as CH_4 and H_2), the effective Lewis number is given by

$$Le_{\text{eff,st}} = x_1 Le_1 + x_2 Le_2, \tag{C.1}$$

where x_i and Le_i are the fuel volumetric fraction and Lewis number of the i^{th} component, respectively. For hydrogen-enriched methane, the former depends on the hydrogen-enrichment percentage, and the later is obtained from [190]

$$Le_i = \frac{\alpha_{\text{th}}}{D_{i,\text{N}_2}}, \tag{C.2}$$

where D_{i,N_2} is the bi-molecular diffusivity of the i^{th} component and nitrogen molecule. α_{th} is the thermal diffusivity of the fuel-air mixture, is given by $\alpha_{\text{th}} = \lambda/(\rho_{\text{r}} c_{\text{p}})$, with ρ_{r}, λ, and c_{p} being the unburned mixture density, thermal conductivity, and specific heat, respectively. λ and c_{p} of the mixture were estimated from the following equations [190, 194]

$$\lambda = \frac{1}{2}\left(\sum_{k=1}^{N} X_k \lambda_k + \frac{1}{\sum_{k=1}^{N} \frac{X_k}{\lambda_k}}\right), \tag{C.3a}$$

$$c_{\text{p}} = \sum_{k=1}^{N} Y_k c_{\text{p},k}, \tag{C.3b}$$

where N is the total number of the species in the fuel-air mixture. X_k, Y_k, λ_k, and $c_{\mathrm{p},k}$ are the mole fraction, mass fraction, thermal conductivity, and specific heat of the the k^{th} species, respectively.

For lean mixtures, the effective Lewis number is given by [191–193]

$$Le_{\mathrm{eff}} = \frac{Le_{\mathrm{O_2}} + A_{\mathrm{Le}} Le_{\mathrm{eff,st}}}{1 + A_{\mathrm{Le}}}, \tag{C.4}$$

where $Le_{\mathrm{O_2}}$ can be estimated from Eq. (C.2) and $A_{\mathrm{Le}} = 1+\beta_{\mathrm{Le}}(1/\phi-1)$. β_{Le} is the Zeldovich number and is given by [191] $\beta_{\mathrm{Le}} = [E_{\mathrm{a}}(T_{\mathrm{b}} - T_{\mathrm{u}})]/(RT_{\mathrm{b}}^2)$, with T_{u}, T_{b}, E_{a}, and R being the reactants temperature, products temperature (the adiabatic flame temperature), overall activation energy, and the universal gas constant, respectively. For all tested conditions, $T_{\mathrm{u}} = 300$ K and E_{a} was extracted from [191].

Appendix D

Hydroxyl radical versus formaldehyde molecule scatter plots for studying the non-flamelet behavior

Following Peters [5], Driscoll et al. [6] suggest that premixed flames feature flamelet behavior provided the variations of species mass fractions versus the reaction progress variable agree with those of the laminar flame. Here, the non-flamelet behavior is defined as deviation of the OH versus CH_2O PLIF towards $OH/OH_{max} = CH_2O/CH_2O_{max} = 1$. As discussed in Section 4.2, such deviation is accompanied by broadening of the reaction zone. However, in Section 4.2, it is not argued if deviation of the OH versus CH_2O PLIF signals towards $OH/OH_{max} = CH_2O/CH_2O_{max} = 0$ corresponds to broadening of the reaction zone. In order to investigate this, data with significant deviation from that of the laminar flame towards $OH/OH_{max} = CH_2O/CH_2O_{max} = 1$ and towards $OH/OH_{max} = CH_2O/CH_2O_{max} = 0$ are respectively highlighted by the red and pink colors in Fig. D.1. The first row of the figure presents variation of OH versus CH_2O for representative frames of two flame conditions that feature non-flamelet behavior (conditions U35H00T0 and U35H00T2). Figures D.1(c) and (d) present the frames related to the results shown in Figs. D.1(a) and (b), respectively.

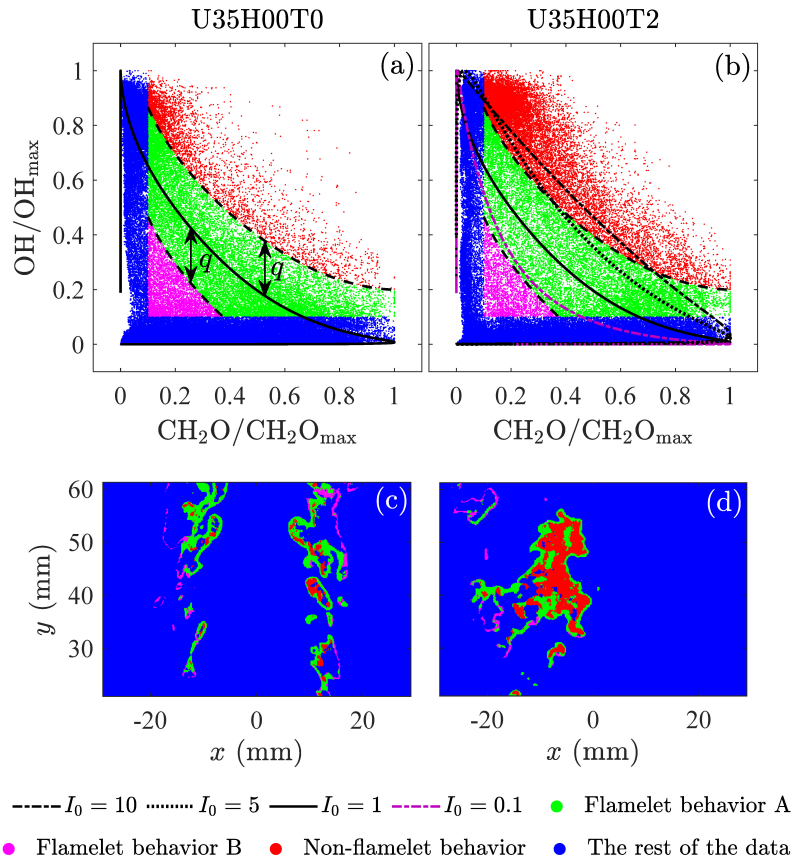

Fig. D.1. (a) and (b) Variations of OH versus CH_2O PLIF data for representative frames of conditions U35H00T0 and U35H00T2. (c) and (d) Regions of the flames shown in the first row featuring flamelet (green color) behavior, non-flamelet (red color) behavior, and deviation towards origin (pink color). Also overlaid on the diagram are data related to freely propagating ($I_0 = 1$) and stretched flames with $I_0 = 0.1$, 5, and 10.

Comparison of the results in Figs. D.1(a and b) with those in Figs. D.1(c and d) suggests only data deviated towards $OH/OH_{max} = CH_2O/CH_2O_{max} = 1$ (the red data points) are associated with broadened reaction zones. Also, the trend in Fig. 4.7(b) suggests that $\mathcal{N}\%$ and broadening of the reaction zone are positively correlated. Compared to the red data points, data closer to $OH/OH_{max} = CH_2O/CH_2O_{max} = 0$ (pink data points) are associated with thin reaction zones and do not pertain to the non-flamelet behavior. Please note that a consistent observation is made for the rest of the frames. As a result, the pink data points were considered to feature the flamelet behavior and are highlighted by the green color in Fig. 4.6.

It is expected that changing the stretch factor ($I_0 = S_L/S_{L,0}$) can change the variation of

OH versus CH_2O PLIF signals. Overlaid on Fig. D.1(b) are the predictions of Cantera simulations for a stretched (opposed jets) laminar flame. In the Cantera simulations, reactants (with the temperature of 300 K) are injected from one inlet and combustion products are injected from the other inlet. Both inlets inject the same mass flow rate and the stretch factor is varied by changing the mass flow rate. Variation of the OH versus CH_2O synthetic PLIF signals are presented in Fig. D.1(b) for flames with stretch factors of $I_0 = 0.1$, $I_0 = 5$, and $I_0 = 10$ and are shown by the purple dotted-dashed, black dotted, and black dotted-dashed curves, respectively. For lean premixed methane-air Bunsen flames, the mean stretch factor is expected to be close to unity [6, 11, 34]. However, the instantaneous stretch factor can be different from unity, and this may contribute to deviation of the OH versus CH_2O plots towards $OH/OH_{max} = CH_2O/CH_2O_{max} = 1$. The value of $q \approx 0.2$ (see Figs. D.1(a and b)) is selected to ensure that the red data points correspond to events for which the deviation from the freely propagating laminar flame is unlikely to be related to the effect of stretch factor. Nevertheless, as discussed in the following, using slightly larger or smaller values for q will not change the reported trends.

In order to study the effect of q on the reported mean $\mathcal{N}\%$ values, a sensitivity analysis was performed by changing the value of q to those 5% larger and smaller than $q = 0.20$. Specifically, mean $\mathcal{N}\%$ was obtained for $q = 0.21$ and $q = 0.19$ and the corresponding results (pertaining to the pure methane-air flames in Table 2.1) are shown in Fig. D.2. Figures D.2(a–c) pertain to the first, second, and third turbulence generating mechanisms, respectively. The results in this figure show that changing q changes the values of mean $\mathcal{N}\%$, however, the reported trends remain unchanged.

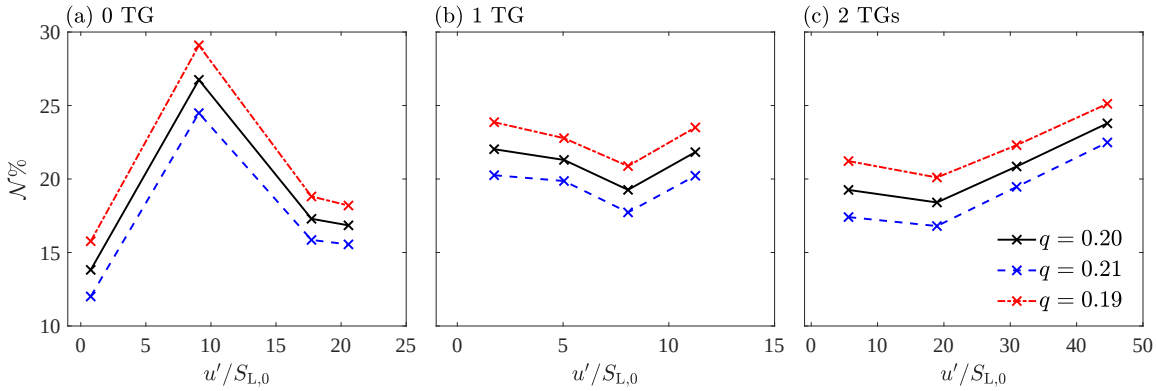

Fig. D.2. Variation of the average non-flamelet behavior ($\mathcal{N}\%$) with turbulence intensity ($u'/S_{L,0}$) for different values of the threshold, q. 0 TG, 1 TG, and 2 TGs pertain to the pure methane-air conditions in Table 2.1 with zero, one, and two turbulence generator(s), respectively.

Appendix E

Effect of the Kelvin-Helmholtz instability on the non-flamelet behavior

In order to investigate the reason why the value of mean $\mathcal{N}\%$ decreases by changing from condition U15H00T0 to condition U35H00T0 (see Fig. 4.8), representative frames related to conditions U15H00T0 and U35H00T0 were considered and are shown in the first and second rows of Fig. E.1, respectively. The first column of the figure presents the vorticity contours. The second column of the figure shows the vortices detected by the Q–criterion with the blue color ($Q \geq 1$ s^{-2}). Also in the second column of the figure, preheat zone, reaction zone, and combustion products are shown by the cyan, red, and yellow colors, respectively. The third column represents the regions featuring flamelet and non-flamelet behaviors, by the green and red colors, respectively. The fourth column shows the variation of the OH versus CH_2O PLIF signals. As the results in the last two columns of Fig. E.1 suggest, condition U15H00T0 features more pronounced non-flamelet behavior compared to condition U35H00T0, which is also statistically consistent with the results shown in Fig. 4.8. As the first and second columns of Fig. E.1 show, the vortices interacting with the flame front are significantly different for conditions U15H00T0 and U35H00T0. The Kelvin-Helmholtz vortices apparent in conditions U15H00T0 pull the reactants towards the reaction zone, leading to a very thin preheat zone, and enlarged reaction zone due to

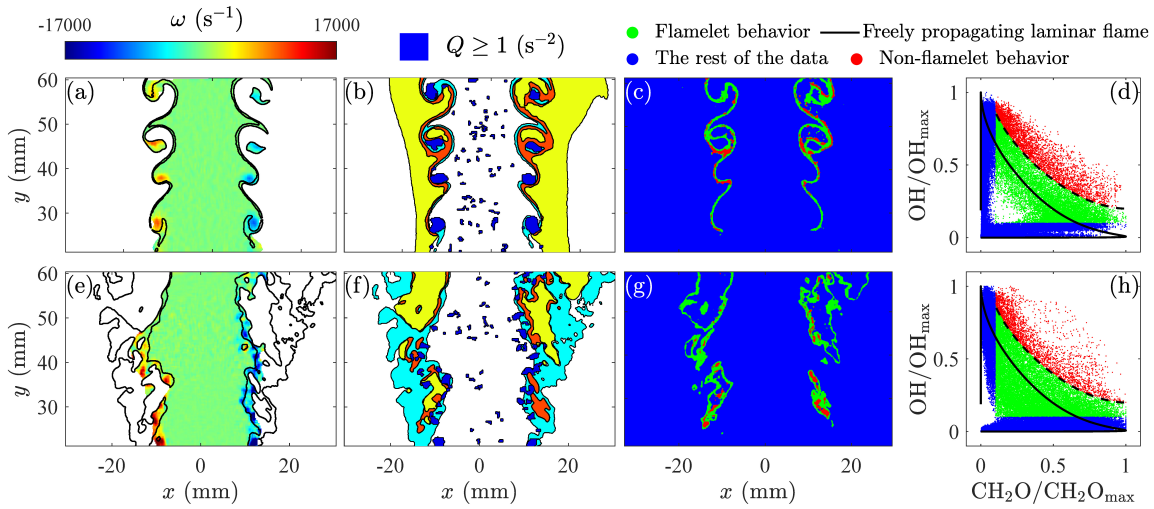

Fig. E.1. Vorticity (first column), flame structure and location of vortices (second column), regions featuring flamelet and non-flamelet behaviors (third column), and the variation of the OH versus CH_2O PLIF signals (fourth column) for representative frames of conditions U15H00T0 (first row) and U35H00T0 (second row).

flame merging compared to laminar flames. The decreased preheat and increased reaction zone thicknesses are also statistically consistent with the results presented in Fig. 4.3. The increased size of the reaction zone, which is apparent by the red regions in Fig. E.1(b), leads to significant deviation from the laminar flame predictions and causes the more pronounced non-flamelet behavior of conditions U15H00T0. However, the interaction of large scale coherent structures with the flame front is less pronounced for condition U35H00T0, and as a result, mean $\mathcal{N}\%$ values are smaller for this flame compared to conditions U15H00T0.

Appendix F

Size of the smallest detectable eddy

Figures F.1(a and b) present a test u and v velocity data, which are the velocity components along y and x directions, respectively. The domain consists of 100 (10×10) interrogation windows. Assuming a vector spacing (and interrogation window size) of 0.47 mm, the vorticity (ω), strain rate ($\epsilon^* = \partial u/\partial x + \partial v/\partial y$), and swirling strength (Q) were calculated and are shown in Figs. F.1(c–e). The regions of $Q > 0$, where swirling strength dominates the strain, were used to identify vortices. The detected vortex is highlighted by the pink color in Fig. F.1(f). As can be seen, a resolution of 0.47 mm allows for detecting a square-shaped vortex with a side length of $l' = 0.47$ mm. Thus, the vortex perimeter is $\mathcal{C} = 4 \times l' = 4 \times 0.47 = 1.88$ mm, and its area is $\mathcal{A} = l' \times l' = 0.47 \times 0.47 = 0.22$ mm^2. Using Eq. (4.3), the equivalent radius of this eddy is given by $\mathcal{R} = 2\mathcal{A}/\mathcal{C} = 0.23$ mm, which is half of the interrogation window size. Its diameter is 0.47 mm. Similarly, for a vortex that corresponds to two interrogation windows, the radius is given by $\mathcal{R} = 2\mathcal{A}/\mathcal{C} = 2l' \times l'/6l' = 0.31$ mm. The diameter of the eddy corresponding to two side-by-side located interrogation windows would be 0.63 mm. In essence, the diameter (radius) of the smallest detected vortex is equal to one (half of) interrogation window length for zero-overlap between the interrogation windows.

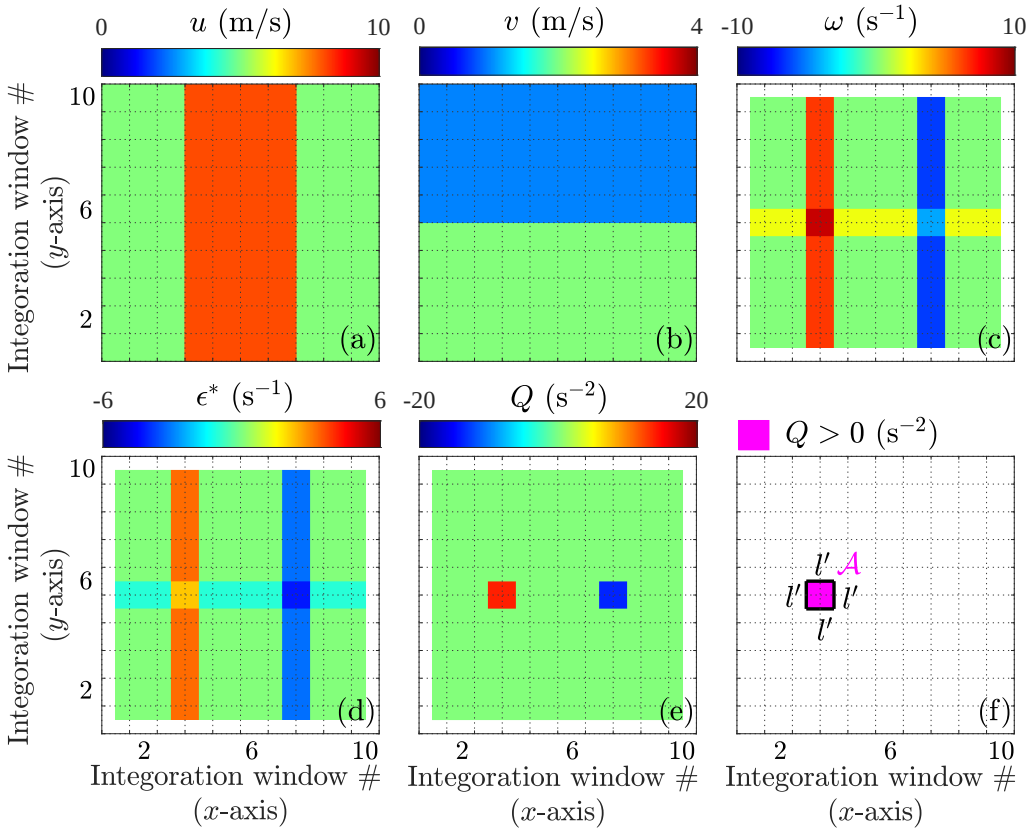

Fig. F.1. Test velocity data along (a) y and (b) x directions. (c) vorticity, (d) strain rate, and (e) swirling strength of the velocity field shown in (a and b). (f) $Q > 0$.